

University of Amsterdam
Institute of Physics
Amsterdam, Netherlands

Thesis for the Degree of Master Physics and Astronomy (GRAPPA
track) 60.0 credits

DARK MATTER AT SMALL SCALE

Eleftherios Malandris
lefteris.malandris@student.uva.nl

Examiner: Dr. Christoph Weniger
University of Amsterdam

Supervisor(s): Dr. Shin'ichiro Ando , Ariane Dekker
University of Amsterdam

Acknowledgements

I would like to thank all the people that have helped me during my work on this thesis. First, I would like to thank my supervisor Shin'ichiro Ando for inspiring me to work on dark matter physics and giving me the opportunity to do what turned out to be an exciting project. I would also like to thank my daily supervisor Ariane Dekker, for the many discussions, help, guidance, and her previous projects she has offered me constantly during this thesis. Finally, I would like to thank Shunichi Horigome for providing me and analyzing the results from dark matter N-body simulations, with his contribution to be extremely important for the progress of this project.

Abstract

The Λ CDM cosmological model is able to describe the universe at large scale with remarkable success, but at small scales in the formation of dark matter halos and galaxies there are problems that still remain open. These problems can be tackled through a variety of ways, with the more common to be by studying the role of baryon physics in dark matter or through analytical dynamic models combined with accurate simulations data. In this project the latter way will be explored, through analytical modeling of dark matter halos with the addition of information from recent dark matter N-body simulations.

The goal of the project is to study dark matter evolution and formation in small scale, by expanding the semi-analytical model of previous work <https://arxiv.org/abs/1803.07691> with halo's substructure spatial information. An extra goal for this work is also to provide extensively different ideas and processes which were tested for the creation of a simplistic model of dark matter halo's substructure for future work.

The previous model which is used as a base in this work describes dark matter halo formation by the extended Press-Schechter formalism with simplistic physical assumptions such as spherical subhaloes following only circular orbits. Despite its simplicity, this model leads to substructure results close to the N-body simulations, with these results containing a variety of substructure characteristics such as subhaloes' density and radius. This approach can be used in a very wide range of mass and redshift values of a host halo, providing a great tool for dark matter studies at small scales. Considering spatial effects on substructure through the spatial evolution of subhaloes and the tidal forces, the addition of such information can lead to more accurate results but also to provide further insights on dark matter substructure's physics. The process of adding spatial information in the existing model contains theoretical expectations but due to lack of observations, results from N-body simulations are used where is necessary. The same model is also adjusted to the case of the warm dark matter (WDM) and is expected to be able to describe also low mass candidates of dark matter. Differences are expected due to the different power spectrum between the CDM and WDM case, especially considering the completely different structure formation with the CDM to show bottom-up formation and WDM the opposite. For the case of the WDM the free streaming effect is expected to lead to key differences in the formation of substructures by affecting both the mass function and the spatial distribution of subhaloes. Additionally, by the substructure of a dark matter halo the distribution of satellite galaxies, based on known galaxy formation conditions, can be obtained and tested with observational data for both CDM and WDM cases.

The model described above can be applied in the sector of indirect dark matter searches, by calculating the gamma ray signal due to dark matter particles' annihilation. There are existing physical models, only as theoretical tools since there is not an observation of this signal so far, based on dark matter candidates like WIMPs. A process is presented for creating mock catalogues of dark matter halos' substructure luminosity 2D templates, which could be useful for testing new analysis techniques or to update observational constraints on dark matter gamma ray signals.

Contents

1. Introduction	1
1.1 Dark matter evidence	2
1.2 Dark matter particle candidates	4
1.3 Dark Matter Structures	6
1.4 Small Scale Problems	10
2. Background	12
2.1 Physical assumptions for subhaloes	12
2.2 Dark matter host halo mass evolution and concentration	13
2.3 Subhaloes' mass loss rate	14
2.4 Subhaloes accretion rate	15
2.5 Substructure characteristics estimation	18
3. Methodology	19
3.1 N-body simulation results	19
3.1.1 Radial distribution results of the simulation	20
3.1.2 Toy Model	22
3.1.3 Mass loss function from simulation (second case)	24
3.1.4 Mass loss function from simulation (third case)	25
3.1.5 Mass loss function combining simulation's results with the toy model	26
3.2 How the spatial information is added in the model	26
3.3 How the final distribution of subhaloes is defined	27
3.4 Adding more information in the model	28
3.5 Results and application of the model	30
4. Results	31
4.1 Cold Dark Matter Case	31
4.1.1 Basic model's assumptions	31
4.1.2 Subhaloes characteristics' distributions	34
4.1.3 Preferred variable values	36
4.1.4 Adding more information in the model	38
4.2 Warm Dark Matter Case	44
4.2.1 Model with basic assumptions	44
4.2.2 Model with additional information	46
4.3 Annihilation boost factor	48
4.3.1 Dark matter substructure's gamma-ray emission	51
4.3.2 Model with additional information	54
5. Discussion	56
5.1 Comparison with similar models	57
5.2 How to further improve this model	57
5.2.1 Haloes elliptical orbit effect	58
5.3 Additional used approaches on the problem	59
5.4 Gravitational lensing applications	60
6. Conclusions	63
References	68

List of Figures

1	Coma galaxy cluster.	1
2	Rotational curve.	2
3	Bullet cluster.	3
4	Dark matter particle candidates.	4
5	<i>Dark matter structure.</i>	6
6	Top hat overdensity.	7
7	Milky Way's satellite galaxies.	11
8	<i>Main model of dark matter halo's substructure.</i>	12
9	<i>Host halo mass evolution and concentration models.</i>	13
10	<i>Mass loss rate of main model.</i>	15
11	<i>Yang accretion rate function (CDM).</i>	16
12	<i>Yang accretion rate function (WDM).</i>	17
13	<i>Yang weight model special case.</i>	17
14	<i>Updated model.</i>	19
15	<i>Spatial distribution of subhaloes of CDM N-body simulation.</i>	20
16	<i>Normalized number density of subhalos of N body simulation.</i>	21
17	<i>Normalized density comparison of Aquarius project and $\nu^2 GC-H^2$ results.</i>	21
18	<i>Mass loss statistics of N-body simulation.</i>	22
19	<i>Mass loss function toy model case.</i>	23
20	<i>Mass loss model case 2.</i>	24
21	<i>Mass loss model case 3.</i>	25
22	<i>Mass loss function models.</i>	26
23	<i>Subhaloes' distance PDF (NFW).</i>	27
24	<i>Subhaloes accretion position.</i>	28
25	<i>Redshift effects on subhaloes.</i>	29
26	<i>Subhaloes completed orbits.</i>	29
27	<i>Subhaloes' number density.</i>	31
28	<i>Subhaloes' number density (closer look).</i>	31
29	<i>Subhaloes' mass function.</i>	32
30	<i>Subhaloes' mass function slope.</i>	32
31	<i>Subhaloes' mass fraction.</i>	33
32	<i>Satellite galaxies.</i>	33
33	<i>Subhaloes concentration and scale radius statistics.</i>	34
34	<i>Subhaloes density and mass statistics.</i>	34
35	<i>Subhaloes' concentration and mass histogram.</i>	35
36	<i>Subhaloes' concentration and position histogram.</i>	35
37	<i>Subhaloes number density with orbital condition.</i>	36
38	<i>Subhaloes' number density with different host's concentration condition.</i>	37
39	<i>Mass loss rate effects of all models.</i>	37
40	<i>New model subhaloes spatial weights.</i>	38
41	<i>Subhaloes number density: new model.</i>	39
42	<i>Subhaloes number density for different subhalo mass: new model.</i>	39
43	<i>Subhaloes mass function: new model.</i>	40
44	<i>Subhaloes mass fraction: new model.</i>	40
45	<i>Satellite galaxies: new model.</i>	41
46	<i>Satellite galaxies mass and density.</i>	41
47	<i>Satellite galaxies positions.</i>	42
48	<i>General condition of the new model.</i>	42
49	<i>Subhaloes number density for different host mass values.</i>	43
50	<i>Subhaloes mass function for different host's mass values.</i>	43
51	<i>Warm dark matter subhaloes number density for $m_{WDM} = 1.5 \text{ keV}$.</i>	44
52	<i>Warm dark matter subhaloes mass function and satellite galaxies for $m_{WDM} = 1.5 \text{ keV}$.</i>	45
53	<i>Warm dark matter subhaloes mass function : new model</i>	46
54	<i>Warm dark matter subhaloes number density : new model</i>	46

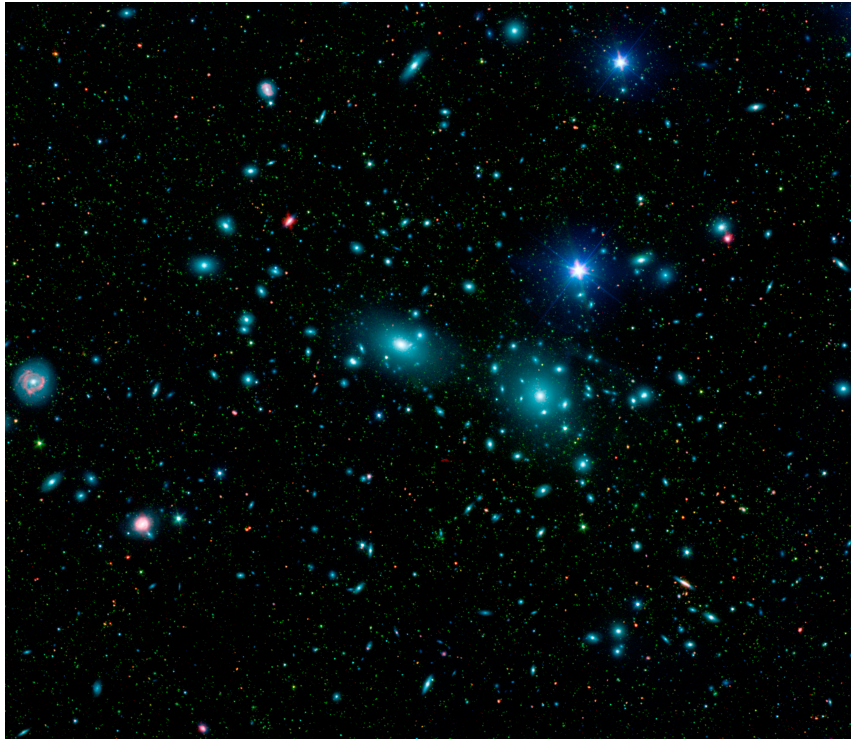
55	<i>Satellite galaxies positions : WDM</i>	47
56	Principle of indirect detection of dark matter. (Image by GAO Linqing and LIN Sujie)	48
57	Boost factor at different distance : first results.	49
58	Boost factor fitting; toy model.	50
59	Surface brightness : first results.	51
60	Boost factor-mass correlation.	51
61	Subhalo mass boost factor relation.	52
62	Simulated subhaloes luminosity.	52
63	Low mass subhaloes luminosity.	53
64	Total luminosity template : Toy and 4 mass models.	53
65	Boost factor at different distances : new model	54
66	Surface Brightness : new model.	54
67	Luminosity templates: new model.	55
68	Total luminosity template: new model.	55
69	<i>Accretion redshift effects on mass loss.</i>	57
70	<i>Elliptical orbit effect.</i>	58
71	<i>Random selection of subhaloes position.</i>	59
72	<i>Mass loss statistics.</i>	60
73	<i>Lensing effects : subhalos mass.</i>	61
74	<i>Lensing effects : subhaloes radius.</i>	62

List of Tables

1. Introduction

The idea of invisible matter in the sky is a quite old idea, but it has become broadly accepted by cosmologists and astrophysicists only recently due to the latest observations [1]. The first discussion of invisible mass can be found in by Lord Kelvin in 1884 where he identified an inconsistency of Newton's Theory of Gravity on the velocity dispersion of stars in galaxy assuming "dark stars". There was similar hypothesis at the early 1900s for a missing amount of matter from galaxies which is not observed. But the first time when the idea of the dark matter as it stands today was mentioned in 1933 by Fritz Zwicky, assuming virialized matter, during his study on the Coma galaxy cluster [2]. Zwicky observed that the rotational velocity of the luminous matter of this cluster had a high disagreement with the expected rotation due to the calculated gravitational attraction within the cluster. His calculations showed rotational velocities higher than expectations at a factor of 400, which was not accurate as recent calculations shows but led to the concept of galaxies having much more mass than the observed luminous amount, which has extremely low photons intensity in comparison to the baryonic matter.

Figure 1: Coma galaxy cluster.

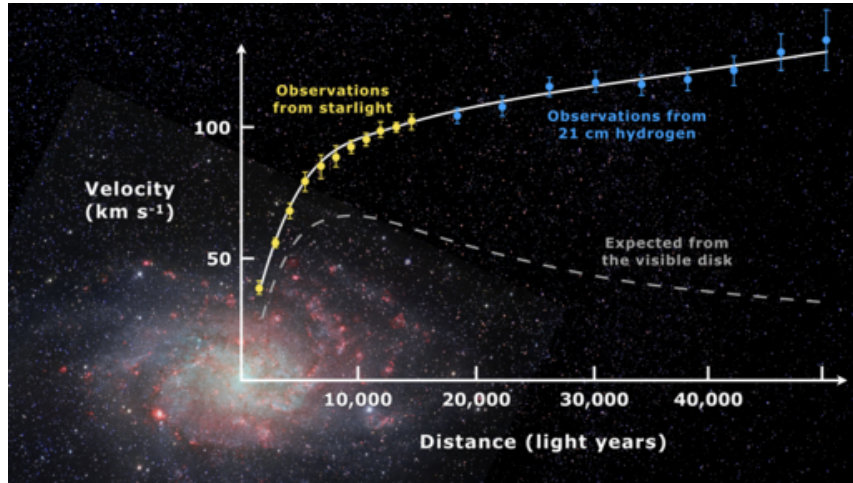


Observations of Coma galaxy cluster from NASA's Spitzer Space Telescope, combines visible-light data from the Sloan Digital Sky Survey (color coded blue) with long and short wavelength infrared views (red and green, respectively). (<http://www.spitzer.caltech.edu/images/1803-ssc2007-10a1-Dwarf-Galaxies-in-the-Coma-Cluster>).

The concept of dark matter did not gain a lot of attention in the respected research community until much later. The early work on similar observations conducted by Vera Rubin, Kent Ford, and Ken Freeman's work in the 1960s and 1970s [3], [4] provided further strong evidences, mainly through galaxy rotation curves. With the observational instruments to have increased accuracy from the early times at 1960s, the velocity of gas and stars of galaxies could be measured leading to completely different measurements from the commonly accepted galactic disk model. The observational accuracy increased further and enough evidence to back the dark matter assumption had found until around 1980s, leading to the applications of dark matter more broadly in cosmology and solving a variety of Big Bang cosmological model inconsistencies. The most known evidence of dark matter are briefly described in the next section.

1.1 Dark matter evidence

Figure 2: Rotational curve.



Rotation curve of spiral galaxy Messier 33 (yellow and blue points with error bars), and a predicted one from distribution of the visible matter (gray line). The discrepancy between the two curves can be accounted for by adding a dark matter halo surrounding the galaxy [5] (created by Mario De Leo).

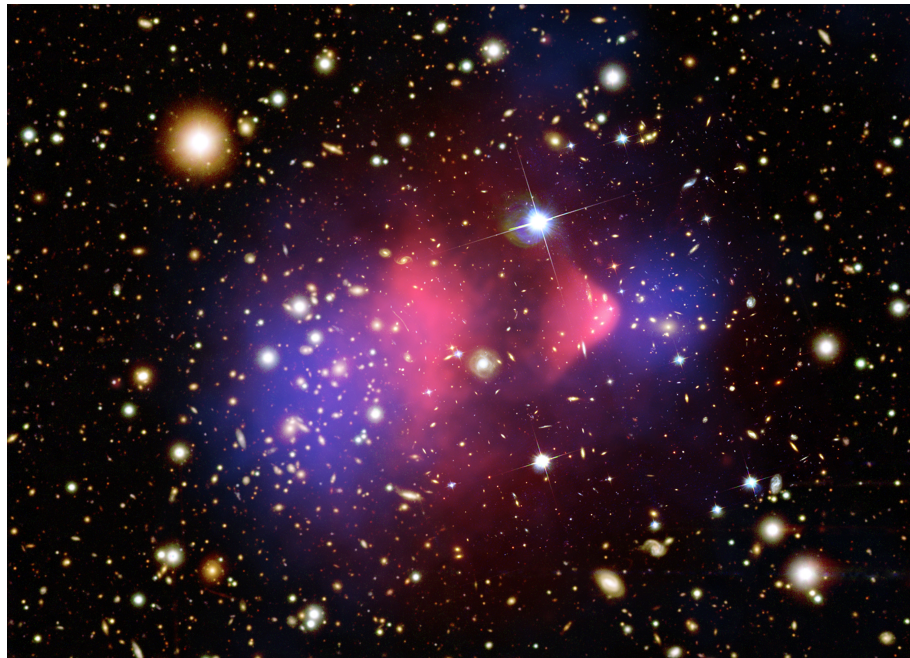
A variety of observations in cosmology and astrophysics cannot be explained by relativity and standard model with only baryons. These observations are the main dark matter evidences and the most known are:

- Galaxy rotation curves : The stars which form the "arms" in spiral galaxies rotate around the center of the galaxy, while the luminous mass (stars) are decreasing with the distance from the center at the outer galactic area. Based on the structure of the luminous mass which forms a disk, the rotational velocity of stars is expected to decrease with increasing distance based on $u^2 = \frac{G \cdot M(r)}{r}$. But observations [5] show, as it can be seen in 2, the rotational velocity to be almost flat (and slightly increasing with distance) at the outer galactic area instead of decreasing based on the visible matter, which indicates the existence of much more mass than the baryonic amount.
- Galaxy clusters mass: The mass of an observed galactic cluster can be measured through three ways, through the radial velocities of the galaxies within the cluster, through gravitational lensing and via their X-ray spectrum and flux. These three ways lead to results which agree with the ratio of dark matter to baryons in the ΛCDM model, dark matter is 5 times more than the baryonic matter [6].
- Gravitational lensing : The most successful theory of gravity is General Relativity until today, which predicts the distortion of light paths near massive objects such as galaxy clusters. Photons emitted by a more distant source, such as a quasar, can have their paths changed if they pass close to a massive object, with that object acting as a lens. Lensing effects are a consequence of mass and so both baryons and dark matter particles contribute to these events. The more massive an object, the more lensing is observed. Examples of gravitational lensing observations are rings (Einstein ring) or arcs (strong lensing) but also weak gravitational lensing thought minute distortions of galaxies' light is possible. An additional observations' case is multiple copies of an object due to strong lensing. By measuring the distortion geometry of the lensed images, the mass of the object which acts as a lens can be calculated, indicating clearly that the visible mass is far from enough to cause these effects.
- Bullet Cluster : The result of a recent collision of two galaxy clusters, with one passing through the other like a bullet, led its apparent center of mass to be far displaced from the

baryonic center of mass. This is happening across our line of sight, so we can clearly see the two clusters [7]. In 3 the blue coloured area shows the majority of the mass causing gravitational lensing effects, while the pink coloured area shows the X-ray observation which is caused by the hot gas of the galaxies. The majority of the mass causing the gravitational lensing is not visible and so it is explained by dark matter. Also, the baryonic matter and dark matter of each galaxy are observed dispatched. This can be explained by each component's interactions, the collisionless dark matter interacts mostly (if not completely) via gravity and travels much further from the baryonic matter, which is additionally interacting electromagnetically and thus slows down.

- Cosmic microwave background : The cosmic microwave background (CMB) is a sight of the early stages of the universe, it is a radio signal very close to a perfect blackbody radiation but contains very small temperature anisotropies of a few parts in 100000. A sky map of anisotropies can be decomposed into an angular power spectrum, which is observed to contain a series of acoustic peaks at near-equal spacing but different heights. These peaks can be explained with incredible accuracy by the Λ CDM model [8], while other cosmological models fails. These peaks provide information on the density of the baryonic matter (1st peak) and dark matter (3rd peak), as a result of the different evolution between the two. The baryons in the early universe were ionized and was interacting heavily with photons of the CMB while the dark matter only affected CMB thought its gravitational potential and thus this difference in their evolution.

Figure 3: Bullet cluster.



The optical image from the Magellan and the Hubble Space Telescope shows galaxies in orange and white in the background. Hot gas, which contains the bulk of the normal matter in the cluster, is shown by the Chandra X-ray image, which shows the hot intracluster gas (pink). Gravitational lensing, the distortion of background images by mass in the cluster, reveals the mass of the cluster is dominated by dark matter (blue), an exotic form of matter abundant in the Universe, with very different properties compared to normal matter. (https://www.esa.int/ESA_Multimedia/Images/2007/07/The_Bullet_Cluster2).

Additional evidence of dark matter are the velocity dispersion [9], redshift-space distortions [10], Lyman-alpha forest [11] and baryon acoustic oscillations [10]. Beside the above mentioned observational and theoretical evidence of the existence of dark matter there is not yet a meas-

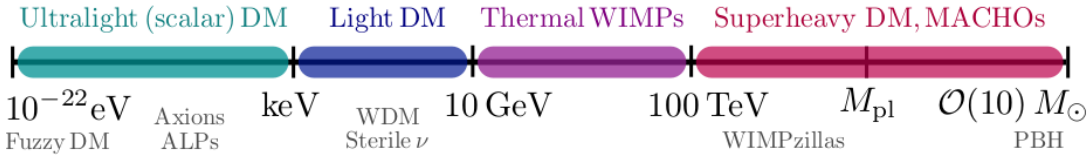
urement, direct or indirect, with high certainty. An alternative explanation would be a modified theory of gravity, meaning that the general relativity is inconsistent and a better theory is needed.

1.2 Dark matter particle candidates

Beside the large scale effects of dark matter a crucial question is the nature of this kind of matter as a particle. This kind of matter can be a known baryonic particle or a non-baryonic particles, for the latter to be based on theoretical predictions mostly through extensions of the Standard Model. There are several candidates with different characteristics, each one of those solves a number of the cosmological problems but are inefficient in others. Their characteristics consists a broad range of parameters with the main to be their mass but also their interactions with baryonic and non-baryonic matter. The focus of this thesis is on the categories of cold and warm dark matter particles, while there are much more candidates outside these categories which are less appealing. For a particle to be considered a dark matter candidate, it has to satisfy some well established criteria:

- Dark matter must be weakly interacting, it must be collisionless.
- Dark matter was probably non-relativistic during the formation of large scale structures (and can therefore form galactic structures).
- Dark matter must be mostly non-baryonic (its abundant is approximately 84 % of the total matter today).
- Dark matter must be stable enough not to decay over the current age of the Universe.
- Dark matter does not appear to emit or absorb light (small effective coupling to photons).
- Massive, since it interacts via gravity.

Figure 4: Dark matter particle candidates.



The broad range of masses for a dark matter particle, with fuzzy dark matter (FDM) at the lightest end and primordial black holes (PBHs) at the heaviest end (picture created by L. Jan Chang [12]).

The cold dark matter (CDM) category consists more massive particles which move at non relativistic velocities and so they lead to a more broad range of mass of substructures from galactic to galactic clusters sizes. The main structure formation is bottom-up, which means that smaller structures formed at the early stages of the universe and on later stages (via collisions, merging and accretion of other structures) the large structures were formed. The best fitted cosmological model so far is the Λ CDM model, which is based on the cold dark matter case. This model has a great agreement with observations and N-body simulations for mainly large structures scales, while in the small scale regime it shows concerning inconsistencies (for distances smaller than $\sim 1 \text{ Mpc}$).

The warm dark matter (WDM) sector consists of particles with very small masses (keV scale) and so relativistic velocities, which lead to smoother fluctuations of the matter density as they propagated through the universe. This means that they can lead to large scale structures like galaxy clusters but are facing problems with smaller structures such as galaxies. In details, the structure formation occurs bottom-up from above their free-streaming scale, and top-down below their free streaming scale. A possible evidence of warm dark matter is the observation of a monochromatic signal around 3.5 keV (WDM energy range), which could be the result of WDM particle annihilation to 2 photons or decay to one photon and a neutrino [13].

Some of the most known dark matter candidates are:

- Weakly interacting massive particles (WIMPs) : These particles interact only through the weak nuclear force and gravity, or possibly also with other interactions with cross-sections no higher than the weak scale and are cold dark matter candidates. They have large masses compared to Standard Model's particles. There is no currently known particle with such properties, but many extensions of the standard model of particle physics, such as supersymmetry, predict such particles (an example is the WINO). Based on the cosmological theoretical models which can explain the cosmological observations, a particle is predicted which has annihilation cross section in the weak-force scale and shows further similarities with the dark matter WIMPs candidate (this apparent coincidence is known as the "WIMP miracle"). Proposed WIMP candidates based on supersymmetry have long been a prime dark matter candidate with mass at the range of 100 GeV. Unfortunately observations focused at these DM particle's mass and cross section ranges, through direct and indirect observational tries, have not led to a successful measurement yet.
- Sterile neutrinos : This candidate have mass in the keV mass range and is an important example of a warm dark matter candidate. The name "sterile" is the results of their interactions, they mix only with the Standard Model neutrinos as they are right-handed neutrinos but not with the other particles of the Standard Model. Sterile neutrinos, like the QCD axion, solve two problems at once, they can explain the lightness of the SM neutrino masses while also serving as the dark matter particle in the Universe. A potential detection signature of sterile neutrino is the production of a photon with energy $m_{DM}/2$ through radiative decay of the sterile neutrino. This would lead to an X-ray line signal in DM-dense regions of the sky.
- Fuzzy cold dark matter : This is a hypothetical form of cold dark matter candidate proposed to solve the cuspy-halo problem (explained at a latter section), which consists the unphysical behavior of dark matter density tending to infinity at its center. It consists extremely light scalar particles with masses on the order of $\simeq 10^{-22}$ eV, which have Compton wavelength on the order of 1 light year. Fuzzy cold dark matter halos in dwarf galaxies would manifest wave behavior on astrophysical scales, and the cusps would be avoided through the Heisenberg uncertainty principle. The wave behavior leads to interference patterns, spherical soliton cores in dark matter halo centers and cylindrical soliton-like cores in dark matter cosmic web filaments.
- Axions : Axions are very light particles ($10^{-4} - 10^{-6}$ eV) with a specific type of self-interaction that makes them a suitable WDM candidate, beside their very low mass. In recent years, axions have become one of the most promising candidates for dark matter. Axions have the theoretical advantage that their existence solves the strong CP problem in quantum chromodynamics, but axion particles have only been theorized and never detected. Axions are an example of a more general category of particle called a WISP (weakly interacting "slender" or "slim" particle), which are the low-mass counterparts of WIMPs.
- Superheavy and composite dark matter : Up to around the Planck mass M_{pl} , there are still DM candidates which are fundamental particles and are known as "WIMPzillas" [14].
- Massive compact halo objects (MACHOs): This candidate is not a new particle but condensed astrophysical objects with very high masses. Potential MACHOs are black holes, primordial black holes, dwarf galaxies, low luminosity stars or astrophysical objects which do not emit light such as planets. As a candidate is not very popular due to the recent observations with the most prominent sector of MACHOs to be the primordial black holes. But there are several studies [15], [16] which imply that that their constraints limit their contribution to dark matter and can account for only a small portion of the entirety of the dark matter in the universe.
- Dark sectors : Particles in the intermediate mass range of 1 GeV, which are thermal DM particles with weak-scale couplings to the Standard Model would be overabundant. This motivates the introduction of new mediators, which must be sufficiently dark to have not been detected thus far, introducing one additional particle or as complex as adding many dark copies of the SM. One example of an actively studied new mediator is the dark photon, a new U(1) gauge boson (typically taken to be massive) which kinetically mixes with the SM photon.

A possible explanation of the physical reality could lead to the existence of more than one dark matter particle candidate to be true, but the existence of some of those is inconsistent with some others. Observations and simulations until today indicate that most of the dark matter, if not all, is cold dark matter.

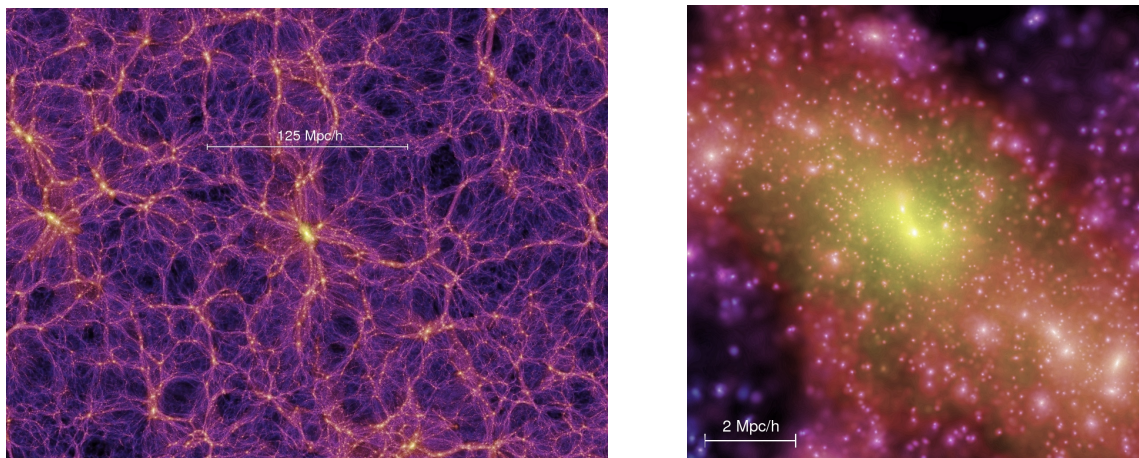
1.3 Dark Matter Structures

Dark matter structures has different forms than the baryonic matter, it forms halos (small scale) and filaments (large scale) as it can be seen in 5. The filaments are the largest structures in the universe, consisting walls of gravitationally bound galaxy superclusters. The filaments are the backbone of the galactic clusters, without them the clusters do not have enough mass in order to be gravitationally bound, while they reach formation size of 80 Mpc forming boundaries between the large cosmic voids [17]. The large scale structures are out of the scope of this project, which is restricted to the small scales and so the dark matter halos.

Dark matter halos are elliptical or spherical objects with their particles to be gravitationally bounded and in virial equilibrium. They emerge from the early stages of the universe from the cosmic fluid in forms of overdensities which overcame the expansion of the universe and formed the first gravitational wells for structure to be formed. These formations are getting in equilibrium at different stages of the universe and merge, collide or accrete each other forming larger halos. The accreted smaller halos are called subhaloes and consist the substructure of their host halo. The evolution of a host halos' substructure have different trajectories for the CDM and the WDM cases, with their differences to be observed only in small scale. Both CDM and WDM halos are getting more massive by accreting smaller subhaloes, with the subhaloes of the CDM to be able to reach very low mass values and WDM to have only massive subhaloes. The number of low mass subhaloes in host halos are much more for the CDM halos, while for the WDM case a few subhaloes can reach small mass values only after their mass is stripped by their host.

The Λ CDM model requires dark matter for the structure formation in the universe, otherwise the expansion of the universe at early ages could not allow baryons to gravitationally collapse and form the observed luminous structures. If this was not the case the whole universe would not have galactic clusters, galaxies and stars etc. but it would be an extremely low density homogeneous fluid of particles and photons following the expansion of space. Luckily for us, this is not the case because dark matter did not interact with the photons (unlike the baryons) and was able to collapse, creating the first seeds of formation by also pulling baryons at later stages. Not all dark matter ended up collapsing, but due to the cosmic fluid not being perfectly homogeneous and thus having perturbations and overdensities, some of which managed to collapse through the process following explained based on the excellent lecture notes of Prof. Frank van den Bosch [18].

Figure 5: *Dark matter structure.*



Dark matter filaments at large scales (left) and dark matter at small scale (right) in form of halos and subhaloes from the results of Millennium Simulation [19].

In this part the way in which halos are formed is shown, since it is crucial to understand what dark matter halos are. The most important property of dark matter particles is that they are collisionless, meaning that they only (or almost only) interact through gravity. A consequence of this characteristic is the different way of forming structures, the lack of collisions means that the particles are passing through the others and makes their collapse and equilibrium completely different from the baryonic structures.

Starting at the early stages of the universe, when halos started their formation process, the conditions of that age have to be defined. A simple cosmological state is assumed such as the Einstein de Sitter (EdS) cosmology after recombination, when the universe was in its matter dominance phase. Although the following treatment is only valid for an EdS cosmology, similar models can be constructed for other cosmologies as well, including Λ CDM. Furthermore, since all cosmologies behave similar to EdS at early times, this treatment is always a good approximation at high redshift values. The previous assumptions describe the universe as a homogeneous fluid, but with the addition of small perturbation in the simple form of top hat spherical overdensities of collisionless dark matter. These assumptions translates mathematically as:

$$\Omega(t) = 1 \quad (1.3.1)$$

$$\bar{\rho} = \frac{1}{6\pi G t^2} \quad (1.3.2)$$

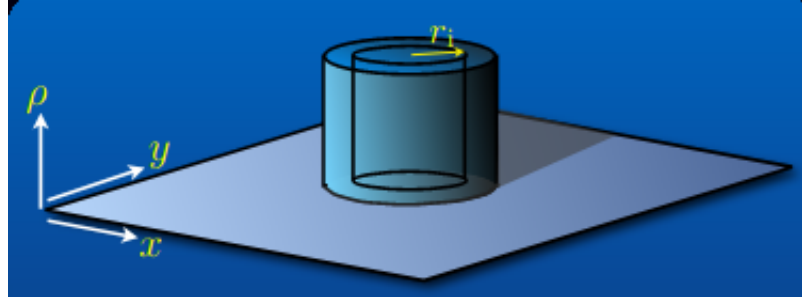
$$D(a) \sim a \sim t^{2/3} \quad (1.3.3)$$

$$H(t) \cdot t = \frac{2}{3} \quad (1.3.4)$$

where $\Omega = \frac{\sum \rho_i}{\bar{\rho}}$, $i = m, r, \Lambda, \kappa$ is the relative density of all components of the universe, a is the cosmic scale factor which quantifies the acceleration of the universe's expansion, $H(t) = \frac{\dot{a}(t)}{a(t)}$ is the Hubble constant and $D(\alpha)$ is the growth function.

Dark matter interacts only gravitationally and so around the center of the mass of an overdensity all the particles with the same distance from there follow the same movement, since the only force is gravity. This leads to the overdensity consisting individual mass shells following the same movement, while considering the collisionless characteristic of the mass shells, they oscillate around the mass center and pass one through the another.

Figure 6: Top hat overdensity.



The mass enclosed in a shell at distance r_i from the mass center is the mass of the background fluid $\bar{\rho}$ with the addition of the mass of the overdensity $\delta_i = \delta\rho_i/\bar{\rho}$:

$$M(r <) = \frac{4}{3}\pi r_i^3 \bar{\rho} [1 + \delta_i] \quad (1.3.5)$$

Based on the Newton's first theorem (or Birkhoff's theorem for General Relativity) a spherically symmetric matter distribution outside a sphere exerts no force on that sphere and so only $M(r <)$ is needed for the gravitational force. The equation of motion which is used for simplicity is the Newtonian Gravity case:

$$\frac{d^2m}{dt^2} = -\frac{GM}{r^2} \quad (1.3.6)$$

By integrating the equation of motion the energy E of the mass shells can be found:

$$\frac{1}{2} \left(\frac{dr}{dt} \right)^2 - \frac{GM}{r} = E \quad (1.3.7)$$

For the mass shells which have $E < 0$ gravitational collapse happens and the formation of a halo is expected, while for $E > 0$ the gravitational forces are not enough to bound the mass and the overdensity is destroyed following the flow of the universe's expansion. For the special case of $E = 0$, in which instabilities can lead to both cases, it can be shown that:

$$E = 0 \Rightarrow r(t) = \left(\frac{9GM}{2} \right)^{1/3} t^{2/3} \Rightarrow r(t) \sim a \quad (1.3.8)$$

It is obvious by $r(t) \sim D(a)$ that the mass shells grows at the same rate as Universe and so their initial velocity can be considered same as the Hubble flow, so $u_i = H_i r_i$. Now the relation of the mass of a shell can be expressed as Hubble constant dependent $M = \frac{H_i^2 r_i^2}{2G} (1 + \delta_i)$, and the mass shell's initial energy can be found:

$$E_i = K_i + W_i = \frac{1}{2} H_i^2 r_i^2 - \frac{GM}{r_i} \Rightarrow E_i = K_i - K_i(1 + \delta_i) = -K_i \delta_i \quad (1.3.9)$$

and so the gravitational collapse condition $E < 0$ is equivalent to $\delta_i > 0$, meaning that in EdS cosmology all overdensities collapse. For non EdS cosmologies this condition is $\delta_i > \Omega_i^{-1} - 1$, which is obviously a more reasonable formation condition.

But for understanding the gravitational collapse of the dark matter the case of $E < 0$ has to be solved, with its solution to be:

$$r = A(1 - \cos\theta) \quad (1.3.10)$$

$$t = B(\theta - \cos\theta) \quad (1.3.11)$$

where $\theta \in [0, 2\pi]$ and $A^3 = GMB^2$ being a relation between the solution's constants. The parameter of the radius and time has change to θ and so the different stages of the mass shells evolution have to discussed. What happens physically is the shells starting their expansion at $r=0$ or $\theta = 0$ until they reach their maximum radius at $\theta = \pi$ or equivalently $t = t_{ta} = \pi B$. At the moment of a shell reaching its maximum distance the turnaround (and so t_{ta}) phase starts heading to its center and its expansion stops. The turnaround phase finishes with the shell collapsing back to $r=0$, at $\theta = 2\pi$ or $t = t_{col} = 2t_{ta}$. At the turnaround moment of the shells it can be found thought the energy conservation that $\frac{r_{max}}{r_i} = \frac{1+\delta_i}{\delta_i} \sim \delta_i^{-1}$. This relation can be translated to smaller perturbations having higher turnaround radius, which depends on the initial overdensity, and so collapse later.

At this stage the solution of the spherical collapse have been found for both time and radius of the mass shells and the density parameters can be expressed to θ :

- Mean density of top hat overdensity:

$$\rho_i = \frac{3M}{4\pi r^3} = \frac{3M}{4\pi A^3} (1 - \cos\theta)^{-3} \quad (1.3.12)$$

- Mean density of the background fluid:

$$\bar{\rho} = \frac{1}{6\pi G t^2} = \frac{1}{6\pi G B^2} (\theta - \sin\theta)^{-2} \quad (1.3.13)$$

The overdensity of the spherical collapse is:

$$1 + \delta_i = \frac{\rho_i}{\bar{\rho}} = \frac{9}{2} \frac{(\theta - \sin\theta)^2}{(1 - \cos\theta)^3} \quad (1.3.14)$$

The spherical collapse (SC) solution leads to non linear perturbations and so the evolution of the overdensity as time changes is not easy to calculate. In the non linear regime of perturbations

special cases of parameters and extra assumptions have to be made often for a solution to be found. But in the range of linear perturbations, where the conditions $\theta_i \ll 1$ and $\delta_i \ll 1$ are met, the solution can easily be found by using a Taylor expansion on θ :

$$\delta_{lin} = \delta_i \left(\frac{t}{t_i} \right)^{2/3} \quad (1.3.15)$$

The crucial values of the overdensities are at the moment of turnaround and collapse, which can be found for both the linear perturbations regime and non-linear (SC).

Turnaround ($\theta = \pi$):

- SC model:

$$1 + \delta(t_{ta}) = \frac{9\pi^2}{16} \simeq 5.55 \quad (1.3.16)$$

- Linear theory:

$$\delta_{lin}(t_{ta}) = \frac{3}{20\pi} (6\pi)^{2/3} \simeq 1.062 \quad (1.3.17)$$

Collapse ($\theta = 2\pi$):

- SC model:

$$\delta(t_{coll}) = \infty \quad (1.3.18)$$

- Linear theory:

$$\delta_{lin}(t_{col}) = \frac{3}{20\pi} (12\pi)^{2/3} \simeq 1.686 \quad (1.3.19)$$

Based on the linear perturbation theory any perturbation with overdensity higher than 1.686 will collapse and this value is called critical density δ_c . Although this approach seems simple the results for assuming an non EdS cosmology differs only by around 1% and so this value is not highly dependant on the used cosmology.

A physical problem which arise from the overdensity values is the $\delta(t_{coll}) = \infty$, which would lead to every dark matter structure to eventually form a black hole. But this is not the case since the collapse is never perfectly spherical. Realistically instead of spherical collapse, elliptical collapse happens due to spatial asymmetries of the overdensities. This can be found by the Zel'dovich approximation, which leads to pancake shape of collapsing dark matter with mass collapsing at different times for different spatial axis. Spatial asymmetries in the overdensity are expected to lead to the directions with more mass to collapse earlier, while the final halos in equilibrium are expected to have elliptical shapes (ellipsoidal collapse). The approach described for structure formation could be even more accurate by considering the angular momentum of dark matter particles and more realistic initial profile. This approach although is more realistically, is out of the scope of this project since the spherically collapse is used with only halos with spherical shape.

Although the process of the dark matter structure formation is clear now and a forming condition is described, the radius of these structures have not yet been discussed. For this reason the halos are called virialized, meaning that they reach equilibrium by following the virial theorem,

$$2K_f + W_f + \Sigma = 0, \Sigma \simeq 0 \quad (1.3.20)$$

where K_f is the kinetic energy, W_f is the potential energy and Σ is the work done by surface pressure which is negligible due to dark matter being collisionless.

At the turn around moment the energy of mass shells is $E_{ta} = W_{ta} = -\frac{GM}{r_{ta}}$ and at virial equilibrium (using the virial theorem) $E_f = W_f/2 = -\frac{GM}{2r_{vir}}$. Due to the energy conservation for the mass shells $E_{ta} = E_f$, it can be shown that $r_{vir} = r_{ta}/2$, the final halo's radius is at half of its turn around (or maximum) radius. Practically halos extend much further from their virial radius, but this distance is used for defining a physically bound where the halos are well defined physically, with the enclosed mass to be referred as halo's virial mass. A common used distance reference which can be found in dark matter studies is the distance where the density is 200 times the critical or mean density of the universe.

Baryon's small structures relax through known two body interactions, but this is not the case for the dark matter (but also galaxies), since the time needed for halos reaching equilibrium with the process of two body interactions is even larger than the age of the universe. But galaxies are observed in equilibrium and so relaxation towards virial equilibrium is obtained differently. The relaxation process consists phase mixing between the particles, violent relaxation due to the rapidly changing gravitational potential inside the halos' radius and through the damping and decay of perturbations due to decoherence effects. The relaxation process is not further discussed since it is not needed for understanding the needed dark matter physics for this project.

An important characteristic which is also needed for the understanding of dark matter halos is their density profiles. Unfortunately predictions from the spherical or ellipsoidal collapse solutions can vary and for the realistic cases of dark matter halos the density profiles are uncertain due to the lack of analytic solutions. Instead of calculating the density profile of halos theoretically, results from dark matter N-body simulations are commonly used. By fitting the density profiles of the simulated halos the common accepted density profile is the Navarro–Frenk–White profile (NFW) [20]:

$$\rho(r) = \frac{\rho_0}{\frac{r}{R_s} \left(1 + \frac{r}{R_s}\right)^2} \quad (1.3.21)$$

where ρ_0, R_s (scale radius) are parameters varying for different halos. At distance R_s the slope of the density profile changes from r^{-1} (inner area) to r^{-3} while $\rho_0 = \rho_{crit} \cdot \delta_c$ is a density parameter which is related to the density of the Universe at the time of collapse. This density profile leads to a cusp at the halo's center, which is obviously unphysical with $\rho(0) = \infty$. There are other suggested density profiles which lead to a core at the halo's inner area but there are not broadly accepted and the NFW profile is still the most accepted case.

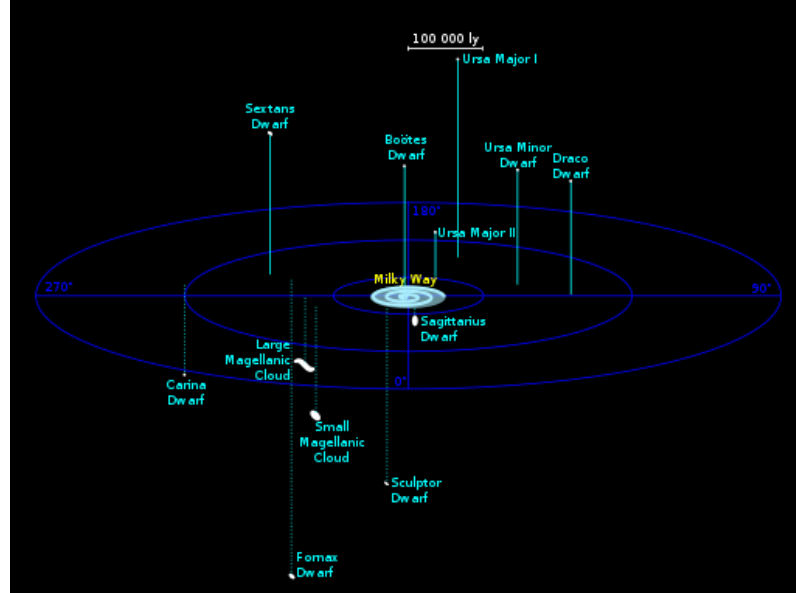
1.4 Small Scale Problems

Although the ΛCDM model is the most successful cosmological model until today it is not perfect, since it suffers from inconsistencies [21]. For the large scale regime of formation and evolution of structure the ΛCDM model shows great agreement with observations, simulations and theoretical expectations but in small scale ,roughly for distances smaller than 1 Mpc, there are several problems with the most important to be:

- The cusp/core problem [22], which issues the unphysical dark matter N-body simulations' density profile at the center of halos. The results of dissipationless N-body simulations lead to cusps profile and so infinite density at the center of halos, similar to NFW profile, while the expected density is a flat profile near the core.
- The “missing satellite problem”, which describes the discrepancy between the number of predicted subhaloes in N-body simulations and those actually observed [23], [24]. The subhaloes are observed in form of satellite galaxies and so it is not clear yet if this disagreement is caused by the true number of subhaloes being fewer or by observational limitations connected to satellite galaxies.
- The “Too Big To Fail” problem, arising from the ΛCDM prediction of satellite galaxies (and thus subhalos) which are too massive and too dense, compared to those observed.
- The angular momentum catastrophe labelling the angular momentum loss in Smooth Particle Hydrodynamics (SPH) simulations of galaxy formation that gives rise to dwarf galaxies' disks with different angular momentum distributions from those of cold dark matter halos, in addition to disc sizes that are much smaller in simulated galaxies compared with observed ones [25].
- The problem of satellites plane, this problem arises from the observations of satellite galaxies of Milky Way and M31. These observed dwarf galaxies are aligned on a thin plane, something that is far from the expected spherical (or elliptical) symmetries of their spatial distribution expected from the ΛCDM paradigm [26].
- The problem of re-obtaining the slope and scatter of the baryonic Tully-Fisher relation $M_b \sim V_c^4$ [27]. The Tully-Fisher relation is fundamental relating the baryonic mass with

the maximum rotational velocity, while also leads to describing the connection between dark matter and visible matter.

Figure 7: Milky Way's satellite galaxies.



Map of the Milky Way and Satellite Galaxies (<http://www.atlasoftheuniverse.com>).

The angular momentum catastrophe and the baryonic Tully-Fisher relation disagreement problems have already possible solutions. It is observed at SPH simulations that the angular moment of baryons is not conserved (10% of the initial value) in gravitational collapsing and the disks of the theoretical galaxies are much smaller than the observed ones [28], [29]. Both these two inconsistencies can be dealt by two possible ways, which consists the feedback of supernovae explosions leading to gas heating effects [30] or the implementation of the dynamical friction of baryonic clumps [31]. This project is based on only dark matter model while these problems need baryonic effects and so they are not met in this work.

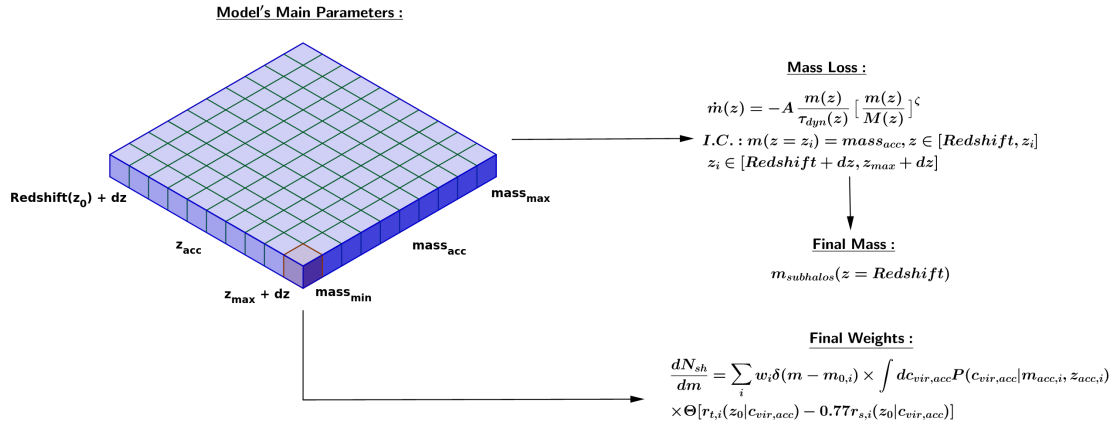
Regarding the cusp/core problem [32], there are several proposals for "turning" the NFW density profile of the N-body simulations to a cored profile. An interesting proposal consists baryonic effects thought supernovae or active galactic nuclei feedback, the huge amount of gas outflows create time varying gravitational potentials by which energy can be transferred to DM particles, leading them to further distances and making smoother the halos' density profile at the inner area [33], [34]. The non-baryonic proposals refer to dark matter particle self interactions [35] or warm dark matter particles [36] with both ways to result to a flat density near the host's core.

The plane satellites problem have a highly flattened distribution of satellite galaxies in 3D space, with a common orientation of satellites being aligned within a plane. Additionally, satellite galaxies are not only on a plane but also much less than the Λ CDM predicted numbers ("missing satellites"). A very prominent solution of the missing satellites problem consist mainly warm dark matter, which leads to much less substructure and so satellites [37]. For the plane satellites problem there are proposals which consists modified gravity theories [38], different galaxy formation conditions [39], dark matter subhalos' accretion asymmetries [40] (accretion along filaments of the cosmic web and infall of satellite galaxies in groups) and baryon-dark matter evolution models [41]. But both of these problems could be even an unpleasant effect of observational limitations, with a large number of satellite galaxies to not be observed due to very low photons emission [39]. But these problems could also indicate that the General relativity is not capturing correctly all the gravitational effects needed for understanding these observations.

2. Background

The goal of this thesis is to add spatial information in an existing dark matter substructure model, which calculates a variety of subhaloes characteristics and is described in this section extensively. This project is based on the dark matter haloes' substructure semi-analytic model SASHIMI [42], which is a model which combines theoretical concepts with N-body simulations results and can calculate the substructure for a big range of host's mass and redshift values. The way in which this model works in a simplistic way can be explained by the following picture. The input consist the mass and redshift of the host halo, the redshift range for considering accretion and the possible subhaloes' masses. Through these values the masses of all subhalos can be found through the mass loss differential equation and a model for their probability to be accreted, based on their accretion mass and redshift, is used additionally. Beside the inputs mentioned above there are more potential variables while the results of this model consist a variety of subhaloes' characteristics such as their concentration, density and scale radius.

Figure 8: *Main model of dark matter halo's substructure.*



This illustration describes the main model in a nutshell, with the main input parameters to be the redshift and mass range, and the main processes to be the accretion rate and mass loss leading to the final values of substructure.

For this part this model has to be studied carefully since it is the core of the project. First of all, this model is affected by the cosmological parameters and models, so it has to be defined clearly. The model is based on the Λ CDM cosmology with important values today ($z=0$) to be [8], [43]:

$$\Omega_\Lambda = 0.692, \Omega_C = 0.25793, \Omega_B = 0.049150, \Omega_m = 0.1415$$

$$\Omega_r = 0, \Omega_0 = 1, H_0 = 67.81 \cdot km/s/Mpc, h = \frac{H_0}{100.0 \cdot km/s/Mpc}, \Omega_M = \frac{\Omega_m}{h^2}$$

In this section the main model's key assumptions and processes are being shown. The two key relations of the model is the mass loss rate and the accretion rate of subhaloes, while the main physical assumptions of this model are presented.

2.1 Physical assumptions for subhaloes

The host halo and subhaloes are assumed to be spherically symmetric objects. The subhaloes orbits are strictly circular orbits. An additional important assumption of this model is that the dark matter haloes and its subhaloes follow the density profile of the Navarro-Frenk-White (NFW)

, with the host halo to be extended outside its virial radius while the subhaloes have zero density at their truncation radius r_t and beyond [20]. The haloes density profile is expected to be extended far from its virial radius from both simulations and observations, but for the subhaloes due to the tidal forces have limited size since the mass outside r_t is stripped from the host.

$$\rho_{host} = \frac{\rho_s \cdot r_s^3}{r(r+r_s)^2} \quad (2.1.1)$$

$$\rho_{sh} = \begin{cases} \frac{\rho_s \cdot r_s^3}{r(r+r_s)^2} & r \leq r_t \\ 0 & r_t < r \end{cases} \quad (2.1.2)$$

In reality dark matter halos shows asymmetries regarding their shape and tend to have elliptical shapes, while the subhaloes' orbits follow elliptical orbits mostly. These two assumptions are used for simplicity, considering elliptical halos collapse differently than the spherical ones and elliptical orbits lead to positions variations and so to unnecessary complexity. It can be seen that the model based on the above assumptions has results close to the N-body simulations ones [42].

2.2 Dark matter host halo mass evolution and concentration

Dark matter haloes are evolving and become more massive for both terms of size and mass through merging with and accreting other halos as time passes. The model which is used for capturing a mean value of the host halo mass evolution at different redshift is [44]:

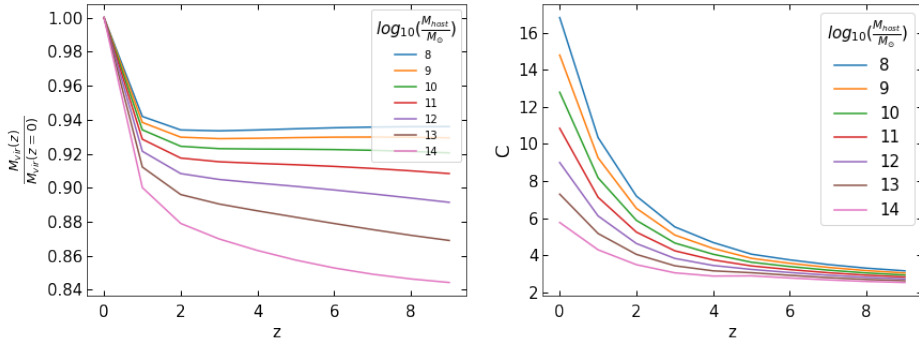
$$\frac{dM}{dz} = (\beta + \alpha \cdot (1 + z - zi)^{-1}) \cdot M z_{zi,vir} \quad (2.2.1)$$

$$\beta = -g(M_0), \alpha = \left(\frac{1.686\sqrt{2/\pi}}{D^2(z=0)} \frac{dD(z=0)}{dz} + 1 \right) \cdot g(M_0), g(M_0) = (S(M_0/q) - S(M_0))^{-1/2} \quad (2.2.2)$$

$$q = 4.137 \cdot z_f^{-0.9476}, z_f = -0.0064 \cdot \log_{10}(M_0)^2 + 0.0237 \cdot \log_{10}(M_0) + 1.8837 \quad (2.2.3)$$

where $D(z)$ and $S(M) = \sigma^2(M)$ are the growth function and the variance of the matter distribution at mass scale M and $z = 0$, respectively. The above relation can be easily modified for being used for given host's mass values at different redshift than 0 [45]. Additionally, the subhaloes' concentration model has to be defined, this model is used for very redshift values ($z \in [0, 10]$), at this redshift ranges the majority of the models fails to capture concentration values properly. The concentration is monotonically increasing for decreasing redshift, any other behavior is nonphysical.

Figure 9: Host halo mass evolution and concentration models.



Host halo mass evolution(left) and concentration model (right) with redshift dependence for a wide range of different host mass values at $z=0$.

The concentration relation that was used is based on [45] and briefly is as follows:

$$c_{halo} = \begin{cases} \log c_{200} = \alpha_1 + \beta_1 \cdot \log\left(\frac{M_{200}}{M_\odot}\right) \cdot [1 + \gamma \cdot \log^2\left(\frac{M_{200}}{M_\odot}\right)] & z \leq 4 \\ \log c_{200} = \alpha_2 + \beta_2 \cdot \log\left(\frac{M_{200}}{M_\odot}\right) & z > 4 \end{cases} \quad (2.2.4)$$

$$\begin{aligned} \alpha_1 &= 1.7543 - 0.2766(1+z) + 0.02039(1+z)^2, \beta_1 = 0.2753 + 0.00351(1+z) - 0.3038(1+z)^{0.0269} \\ \gamma &= -0.01537 + 0.02102(1+z)^{-0.1475} \\ \alpha_2 &= 1.3081 - 0.1078(1+z) + 0.00398(1+z)^2, \beta_2 = 0.0223 - 0.0944(1+z)^{-0.3907} \end{aligned}$$

2.3 Subhaloes' mass loss rate

The mass loss rate which is used in this model is the result of combining theoretical calculations with Monte Carlo simulations results for parameters estimation. The mass loss rate \dot{m}_{sh} , with this being a derivative other time, of a subhalo which is orbiting in the gravitational potential of a host halo due to tidal stripping can be formalized as [46]:

$$\dot{m}_{sh}(z) = -A \cdot \frac{m_{sh}(z)}{\tau_{dyn}(z)} \cdot \left[\frac{m_{sh}(z)}{M_{host}(z)} \right]^\zeta \quad (2.3.1)$$

where $\tau_{dyn}(z)$ is the dynamical timescale of subhaloes' orbits, m_{sh} is the subhalos mass variable and A, ζ are dimensionless parameters. The values of ζ and A in other works are assumed to be constants [46] regarding redshift changes but for this work an estimation was made through fitting of Monte Carlo simulations of mass loss rate of subhaloes, which showed that these quantities depend (in a small order) to redshift but also to host's mass.

This Monte Carlo simulation [42] used subhalo mass values at accretion m_{acc} being uniformly in a logarithmic scale between the smallest mass $10^{-6} M_\odot$ and the maximum mass $0.1 M_{host}$. For each set of m_{acc} and z_{acc} (as well as z and M_{host}), the mass loss rate \dot{m} is calculated with a simple mass loss rate formalism:

$$\dot{m} = \frac{m - m(r_t)}{T_r} \quad (2.3.2)$$

where T_r , m , and $m(r_t)$ are the orbital period, the virial mass of the subhalo just after accretion, and the mass enclosed in the tidal truncation radius r_t of the subhalo respectively. The parameters which have to be estimated through the Monte Carlo simulation are the T_r and $m(r_t)$ for different subhalo and host masses but also at different redshift.

The random variables of subhaloes are the circular orbit radius R_c and the orbit circularity η at infall, which are randomly selected following given distribution functions as [47]. The host's random variable is its virial concentration c_{vir}^{host} for a given mass, which is selected from the lognormal distribution with mean value calculated by the previously defined concentration model [45]. For these random subhaloes their energy and angular momentum have to be calculated, while for the host its gravitational potential. The simulation's physical assumptions follow classical mechanics for virialized objects, they can be briefly defined as:

$$E = \frac{1}{2} V_c^2 + \Phi(R_c), L = \eta R_c V_c \quad (2.3.3)$$

$$\Phi(R) = -V_{vir}^2 \frac{\ln[1 + c_{vir}^{host} \cdot R/R_{vir}]}{f(c_{vir}^{host}) \cdot R/R_{vir}} \quad (2.3.4)$$

$$f(c) = \ln(1 + c) - \frac{c}{1 + c} \quad (2.3.5)$$

$$V_c = (GM/R_c)^{1/2}, V_{vir} = (GM/R_{vir})^{1/2} \quad (2.3.6)$$

where E is the mechanical energy, L the angular momentum of subhaloes, Φ is the host's gravitational potential V_i is subhaloes' velocity (circular or virial).

From the previous calculated physical quantities the orbital period and the subhalos truncated radius can be estimated, using an additional assumption of constant ρ_s and r_s of subhaloes (although it can be seen in N-body simulations such as [48] they change by $\leq 50\%$ in one orbit and thus is not the realistic case), through:

$$T_r = 2 \int_{R_p}^{R_\alpha} \frac{dR}{\sqrt{2[E - \Phi(R)] - L^2/R^2}} \quad (2.3.7)$$

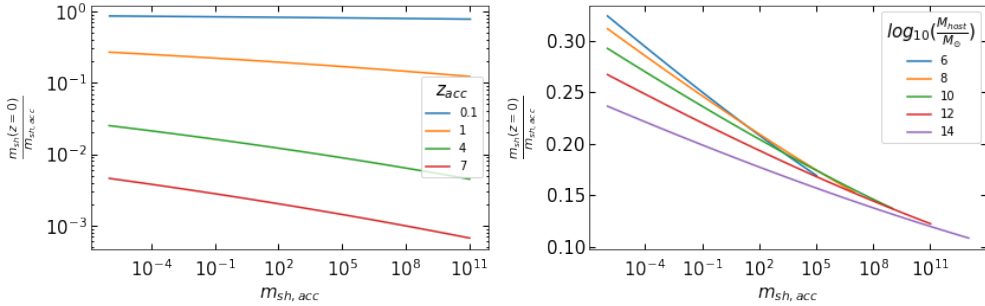
$$r_t = R_p \left[\frac{m(r_t)/M(< R_p)}{2 + \frac{L^2}{R_p GM(< R_p)} - \frac{dlnM(R_p)}{dlnR}} \right] \quad (2.3.8)$$

The resulted relations for A and ζ of this process are as follows [42]:

$$\log_{10}A = [-0.0003 \cdot \log_{10}(\frac{M_{host}}{M_\odot}) + 0.02] \cdot z + 0.011 \cdot \log_{10}(\frac{M_{host}}{M_\odot}) - 0.354 \quad (2.3.9)$$

$$\zeta = [0.00012 \cdot \log_{10}(\frac{M_{host}}{M_\odot}) - 0.0033] \cdot z - 0.0011 \cdot \log_{10}(\frac{M_{host}}{M_\odot}) + 0.026 \quad (2.3.10)$$

Figure 10: *Mass loss rate of main model.*



Mass fraction of subhalo mass after tidal stripping loss to its accretion mass for different subhalo accretion mass values, for a variety of accretion redshift (left) and host mass (right) values.

The Monte Carlo simulations mentioned above covered the host mass (defined as M_{200}) from $M_{host} = 10^{-6} M_\odot$ to $10^{16} M_\odot$ and redshift values from $z = 0$ to 7. The results of this simplistic simulation were also compared with the N body simulations' results $\nu^2 2GC - S$, $\nu^2 GC - H2$, Phi-1, Phi-2 and AN8192L800 with great success and so the tidal forces formula is creditable.

2.4 Subhaloes accretion rate

The subhaloes accretion rate function of this model is based on the extended Press-Schechter formalism. The Press-Schechter formalism predicts the number of haloes at different stages of the universe's evolution as the result of the gravitational collapse of dark matter early small density fluctuations. The specific accretion model is called Yang model [49] (model 3), which also includes calibration of the theoretical model with dark matter N-body simulation results.

The mass accretion history is described by the number of subhaloes accreted into the host per unit of logarithmic mass range around and per unit of redshift range around accretion redshift:

$$\frac{d^2N_{sh}}{dlnm_{acc}dz_{acc}} = F(s_{acc}, \delta_{acc}|S_0, \delta_0; M_{acc}) \frac{ds_{acc}}{dm_{acc}} \frac{d\bar{M}_{acc}}{dz_{acc}} \quad (2.4.1)$$

where the variance s_{acc} and overdensity δ_{acc} are used to parameterize the mass and redshift, respectively, since they are defined as $s_{acc} = \sigma^2(m_{acc}, z = 0)$ and $\delta_{acc} = \delta_c(z_{acc}) = 1.686/D(z_{acc})$ by [50]. The quantity $\sigma(M, z)$ is the variance of the linear density field at redshift z on mass scale M . The $D(z_{acc})$ is the growth function and δ_c is the critical overdensity value for gravitational

collapse. Similarly, for the host, we adopt $S_0 = \sigma^2(M_0, z = 0)$ and $\delta_0 = \delta_{sc}(z = 0)$ to characterize the mass M_0 and redshift $z = 0$ as a boundary condition. The mass of the host M_{acc} at the accretion redshift z_{acc} (that eventually evolves to M_0 at z_0) follows the probability distribution $P(M_{acc}|S_0, \delta_0)$, for which a log-normal distribution is adopted with a logarithmic mean and a logarithmic dispersion:

$$\overline{M}_{acc} = M(z_{acc}|M_0, z_0), \quad \sigma_{\log M_{acc}} = 0.12 - 0.15 \cdot \log_{10} \left(\frac{M_{acc}}{M_0} \right) \quad (2.4.2)$$

The previously defined $F(s_{acc}, \delta_{acc}|S_0, \delta_0; M_{acc})$ is the mass fraction in progenitor haloes of mass m_a to be accreted at redshift z_a can be calculated, and so the wanted $d^2N_{sh}/(dlnm_{acc}dz_{acc})$, for arbitrary hosts by:

$$F(s_{acc}, \delta_{acc}|S_0, \delta_0; M_{acc}) = \Phi(s_{acc}, \delta_{acc}|S_0, \delta_0; M_{acc}) P(M_{acc}|S_0, \delta_0) dM_{acc} \quad (2.4.3)$$

$$\Phi(s_{acc}, \delta_{acc}|S_0, \delta_0; M_{acc}) = \left[\int_{S_{max}}^{\infty} F(s_{acc}, \delta_{acc}|S_0, \delta_0; M_{acc}) ds_{acc} \right]^{-1} \cdot \begin{cases} 0 & m_{acc} \leq m_{max} \\ F(s_{acc}, \delta_{acc}|S_0, \delta_0; M_{acc}) & \text{otherwise} \end{cases} \quad (2.4.4)$$

$$F(s_{acc}, \delta_{acc}|S_0, \delta_0; M_{acc}) = \frac{1}{\sqrt{2\pi}} \frac{(\delta_{acc} - \delta_M)}{(s_{acc} - S_M)^{3/2}} \exp \left[-\frac{(\delta_{acc} - \delta_M)^2}{2(s_{acc} - S_M)} \right] \quad (2.4.5)$$

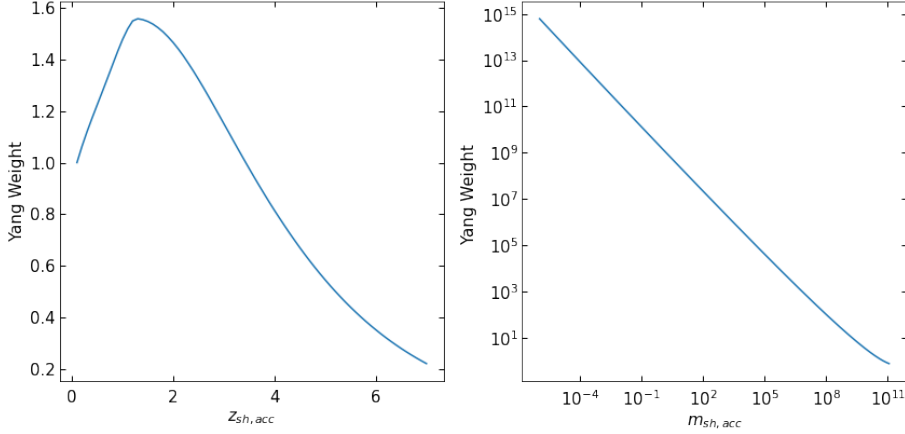
where $m_{max} = \min[M_{acc}, M_0/2]$ and $M_{max} = \min[M_{acc} + m_{max}, M_0]$ are introduced such that the mass hierarchy of the host mass before and after subhalo accretions is assured, $S_M = \sigma_M^2(M_{max})$ and δ_M is defined as the spherical collapse overdensity $\delta_{sc}(z)$ at a redshift at which $M = M_{max}$.

The resulting quantity of the Yang model, which is called Yang weights w_i , is equal to the number of subhaloes accreted at z_{acc} with mass m_{acc} :

$$w_i \sim \frac{d^2N_{sh}}{dlnm_{acc}dz_{acc}}, \quad \sum w_i = N_{sh,tot} = \int dlnm_{acc} \int dz_{acc} \frac{d^2N_{sh}}{dlnm_{acc}dz_{acc}} \quad (2.4.6)$$

Due to the large changes of subhaloes' number for different subhaloes' mass values, the function of Yang weights depending on the accretion redshift, for different subhaloes' masses, is presented normalized to the Yang weight at $z=0.1$ for all subhaloes' mass values (is identical for all m_{acc} values).

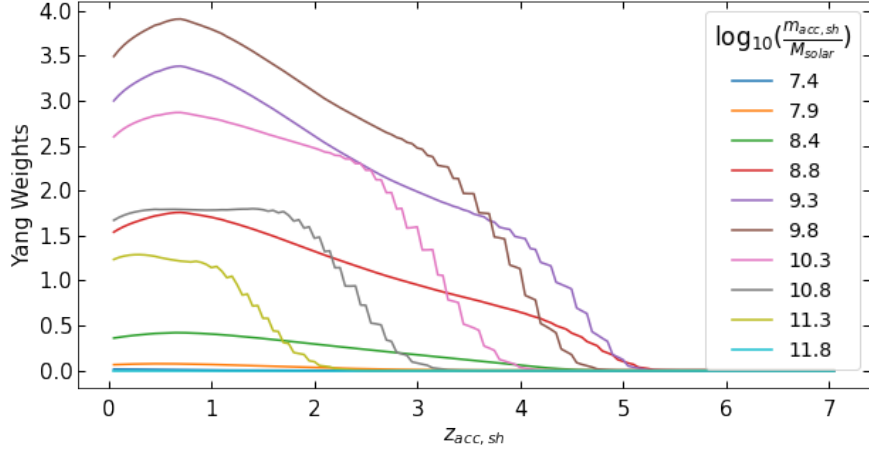
Figure 11: Yang accretion rate function (CDM).



Yang weight of subhaloes for different redshift values in units of w_i at $z=0.1$ (left) and subhaloes' number for different subhalo accretion masses at $z=0.1$.

The same approach for accretion rate of subhaloes can be used for warm dark matter by using the appropriate matter power spectrum. The warm dark matter particle mass is expected to be much less smaller than the cold dark matter particle candidates. The WDM particle masses are in the range of keV, while particle's mass values close to GeV and higher have similar behavior (it should be identical) to the CDM accretion rate function. For the warm dark matter case the less massive the particles are the less substructure there is, while the free streaming effect leads to less substructure (by mass cut-offs for subhaloes' accretion mass values).

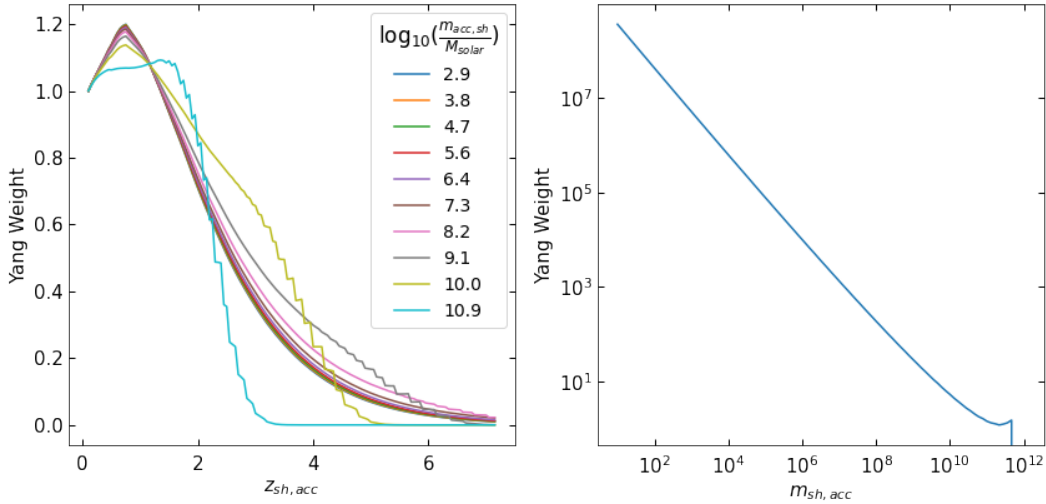
Figure 12: *Yang accretion rate function (WDM)*.



Yang weights for the case of warm dark matter particle with mass 1.5 keV for different subhalo mass values.

From the warm dark matter case of low mass particles the Yang weights are very small and so the substructure is much less than the case of the cold dark matter. Also, subhaloes with different accretion mass show different profiles and so mass segregation could be expected. Additionally, an accretion mass cut off can be observed for values close to 10^7 solar masses for $m_{WDM} = 1.5$ keV.

Figure 13: *Yang weight model special case*.



Probability weight of subhalo for different redshift values in units of weight value at $z=0.1$ (left) and subhaloes' number for different subhalo accretion masses for $m_{DM} = 1$ GeV.

It can be seen that the Yang weights are getting close to the CDM presented weights as expected.

2.5 Substructure characteristics estimation

Here the main calculations of the model are shown for the estimation of r_s, ρ_s, c and r_t at the wanted redshift after the effects of tidal forces. Subhaloes are virialized objects with a well defined spatial border at r_t , for $r > r_t$ the host's gravitational potential through the tidal forces strips their mass and so the field halo assumptions is no longer valid.

Firstly, the density and scale radius of subhaloes have to be calculated at accretion. The virial radius r_{vir} of subhaloes can be calculated by:

$$r_{vir,acc} = \left(\frac{3 \cdot m_{acc,vir}}{4 \cdot \pi \cdot \rho_{crit} \cdot g(z) \cdot \Delta_c(\Omega_z - 1)} \right)^{\frac{1}{3}} \quad (2.5.1)$$

where $\Delta_c = 18\pi^2 + 82d - 39d^2$, $d = \Omega_m(1+z_{acc})^3 / [\Omega_m(1+z_{acc})^3 + \Omega_\Lambda] - 1$ [51], and $\rho_c(z_{acc})$ is the critical density at accretion. Similarly the r_{200} can be calculated, by replacing the $m_{acc,vir}$ and ρ_{crit} with $m_{acc,200}$ and $200\rho_{crit}$ respectively, in order to find the virial concentration at accretion $c_{vir,acc} = c_{200,acc} \cdot \frac{r_{vir,acc}}{r_{200,acc}}$ [52]. The $c_{200,acc}$ is given by a log-normal distribution with mean from the defined concentration model and $\sigma_{logc}=0.12$ [53] and so the scale radius can be found via $r_{s,acc} = r_{vir,acc}/c_{vir,acc}$. The only crucial subhaloes' physical quantity at accretion which have not been found is their density, which is given by:

$$\rho_{acc} = \frac{m_{acc}}{4 \cdot \pi \cdot r_{s,acc}^3 \cdot f(c_{vir,acc})} \quad (2.5.2)$$

The set of parameters $(r_{s,acc}, \rho_{s,acc})$ is related to the maximum circular velocity V_{max} and radius r_{max} at which the circular velocity reaches the maximum through:

$$r_s = \frac{r_{max}}{2.163} \quad (2.5.3)$$

$$\rho_s = \frac{4.625}{4\pi G} \left(\frac{V_{max}}{r_s} \right)^2 \quad (2.5.4)$$

The evolution of r_{max} and V_{max} from accretion to the arbitrary final redshift z_0 , when the tidal stripping effects change the system, is described by the relation [54]:

$$\frac{V_{max,0}}{V_{max,acc}} = \frac{2^{0.4}(m_0/m_{acc})^{0.3}}{(1+m_0/m_{acc})^{0.4}} \quad (2.5.5)$$

$$\frac{r_{max,0}}{r_{max,acc}} = \frac{2^{-0.3}(m_0/m_{acc})^{0.4}}{(1+m_0/m_{acc})^{-0.3}} \quad (2.5.6)$$

The above relation is valid for inner density profiles which are proportional to $1/r$ as the NFW density profile, while the m_0 is the subhalos mass at z_0 which is calculated by the previously defined mass loss rate. By solving the system of the equations the scale radius r_s and the density ρ_s of subhalos can be extracted at the wanted redshift z_0 . The only identified parameter of subhalos is their truncation radius r_t at z_0 by solving the equation:

$$m_0 = 4\pi\rho_{s,0}r_{s,0}^3 f\left(\frac{r_{t,0}}{r_{s,0}}\right) \quad (2.5.7)$$

The subhalos concentration at z_0 according to is $c_{sub,0} = \frac{r_{t,0}}{r_{s,0}}$, while subhalos with $c_{sub,0}$ smaller than 0.77 are not further considered since they are assumed as completely disrupted [55]. And to summarize the general process of this model's calculations, by given z_{acc} and m_{acc} of subhalos their weights are calculated by the subhalos accretion rate function and by the mass loss rate their mass at the final redshift is calculated. After that, the process of this section calculates the subhalos characteristics and combined with their weights leads to the substructure's information at z_0 .

3. Methodology

The previously presented dark matter halo's substructure model [42], which is referred to main model (or average or no spatial) in this thesis, do not have spatial information, but its main formalism is based on mean values of tidal stripping. The goal of this project is to include spatial information in this model in order to provide more insights on subhalo spatial distribution and properties related to that.

The general assumptions on dark matter halo and subhaloes are the same within also the same range of mass and redshift values as the main model. The additional assumptions are as follows:

- All subhaloes follow circular orbits.
- The positions of subhaloes at the "end" redshift value are following the host halo's NFW density profile.
- The positions of subhaloes are independent from their accretion position and redshift.
- The tidal forces formula for different positions inside the host is based on results of a N-body simulation.

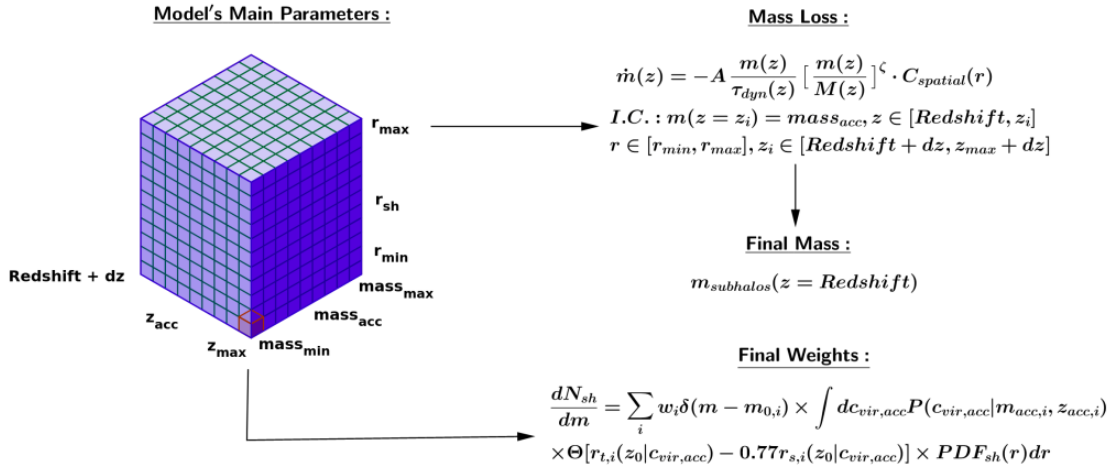


Figure 14: *Updated model.*

An illustration of the new dark matter substructure model, presenting the main input parameters and functions for the substructure results.

The updated model has an additional dimension, compared to the main model, for the input parameters that presents the subhaloes' positions. Also, the mass loss has an additional term which depends on substructure's position and the probability of the subhaloes has an additional term based on the NFW density profile beside the Yang model weights. These new implementations are explained in the following subsections.

An important note for this model is that due to the limited resolution of N-body dark matter simulations on the subhaloes mass and spatial positions, as a result of the extremely high computational cost, the respected tidal forces relations can vary. A reason for that is the conditions for subhaloes properties information. The simulation's results are for a host halo with mass $1.8 \cdot 10^{12}$ solar masses at redshift $z=0$, so the results of this project are focused on this host's mass value, but the same ranges of host mass values and redshift are applicable as the ones of the main model.

3.1 N-body simulation results

The following simulation's results are the analysis work of Shunichi Horigome (Postdoc at University of Tokyo) and are based on the $\nu^2GC - H2$. All the presented results are for a cold dark matter host halo with the characteristics:

- Host mass value is ranged from $3.16 \cdot 10^{11} \frac{M_\odot}{h}$ to $3.16 \cdot 10^{12} \frac{M_\odot}{h}$ (is defined as $\sim 10^{12} M_\odot$).
- The virial radius of the host halo is from $1.3844 \cdot 10^2$ to $2.97818 \cdot 10^2 \frac{kpc}{h}$ (is defined as $2.18 \cdot 10^2 \frac{kpc}{h}$).
- The spatial resolution is $10^{-5} \frac{Mpc}{h}$.

3.1.1 Radial distribution results of the simulation

The spatial distribution of the subhaloes of the dark matter host defined above is presented in 15 at redshift $z=0$. Due to the mass resolution limitations the subhalos of this result are massive with mass $> 10^6 M_\odot$, much higher than the subhalos mass range of the main model. But this is not expected to be a problem as described next. The subhaloes' number is decreasing highly with increasing their mass value. Due to these large differences, in this work the normalized counts of subhalos, with different masses, are preferable for presenting the spatial characteristics of the substructure as a whole. Also, the spatial characteristics of the substructure are not expected to change in a high order for different host mass and units of $\frac{distance}{R_{vir,host}}$ are used in order to describe the result universally.

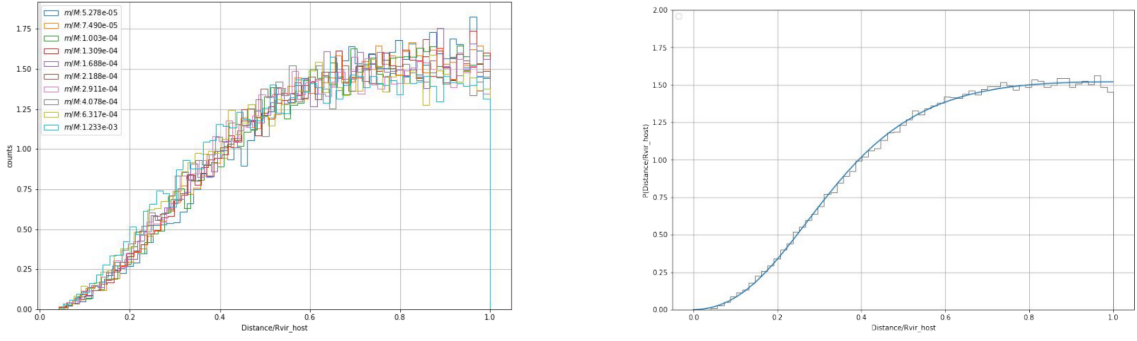


Figure 15: *Spatial distribution of subhaloes of CDM N-body simulation.*

Spatial distribution of subhaloes for different mass bins (left) and total subhaloes (right).

The radial (distance from host's center) probability density function of subhaloes calculated for different mass bins and no mass segregation was shown. All the subhaloes regardless their mass follow the same PDF regarding their position (or orbital radius value). The subhaloes position being independent from their mass simplify the substructure modeling, the same probability function can be used for all subhaloes in a physical way and not by excluding key information from the model. By the PDF of all subhaloes two functions for their linear probability density function was found. The reason that lead to two functions is due to the uncertainty on the host's virial radius but also the spatial resolution of the simulation.

$$PDF_{1D,1}(q) = \frac{1}{S(c)} \cdot \frac{c \cdot q^2}{c \cdot q^2 + (1 - c) \cdot (1 - q)^2} \quad (3.1.1)$$

$$q = \frac{distance}{R_{vir,host}}, c = 0.821 \pm 0.002, S(c) = \int_0^1 \frac{c \cdot q^2}{c \cdot q^2 + (1 - c) \cdot (1 - q)^2} dx, S(0.821) \simeq 0.658 \quad (3.1.2)$$

This function is the result of the direct fitting of the simulation's results presented above. But in the inner area the number density ($\frac{PDF}{4\pi q^2} = \frac{dN_{sh}}{4\pi q^2 dq \sum N_{sh}}$) is not as expected as it can be seen in the next figure. A second fitted function was also used and is presented below.

$$PDF_{1D,2}(q) = \frac{1}{S(c)} \cdot \frac{q^2}{(1 + (q/c)^2)^{3/\alpha}}, q = \frac{distance}{R_{vir,host}}, S(c) = \int_0^1 \frac{q^2}{(1 + (q/c)^2)^{3/\alpha}} dq \quad (3.1.3)$$

with $a = 2.2, c = 0.606, S(0.606) \simeq 0.102$

As it can be seen 16, the second spatial distribution function (simulation 2, orange line) captures better the core effect at the inner host's area and is preferable. The first function shows a physically unreasonable decrease from distance 0.2 host's virial radius and below while the second case reaches higher number density values and represents a more natural core behavior. Additionally, a spatial distribution function as a result of N-body simulation with higher resolution can be found in Aquarius Project simulation [56] with:

$$n_E(\text{distance}) = \rho_{-2} \cdot e^{(-\frac{2}{\alpha}) \cdot [(\frac{\text{distance}}{r_{-2}})^{\alpha} - 1]}, \alpha = 0.678, r_{-2} = 199 \text{kpc} = 0.81 \cdot R_{\text{vir,host}} \quad (3.1.4)$$

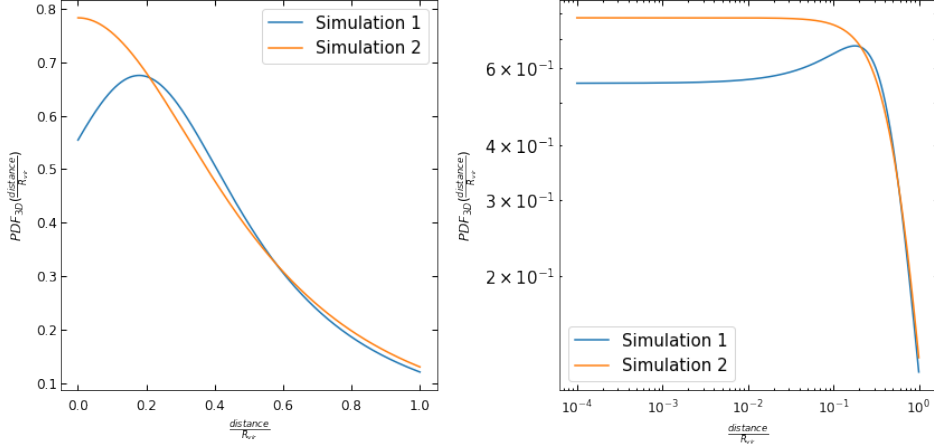


Figure 16: *Normalized number density of subhalos of N body simulation.*

Normalized number density of subhaloes functions as a result of fitting of the N body simulation's result in linear(left) and logarithmic (right) scale.

The dark matter host mass of the Aquarius project results is $1.8 \cdot M_{\odot}$, which is very close to the $\nu^2\text{GC}-H^2$ simulated host and so no high differences are expected. But it can be seen that there is a high disagreement for small distances, with the Aquarius function to have higher subhaloes number density near the core and a more smooth change of its slope at that area.

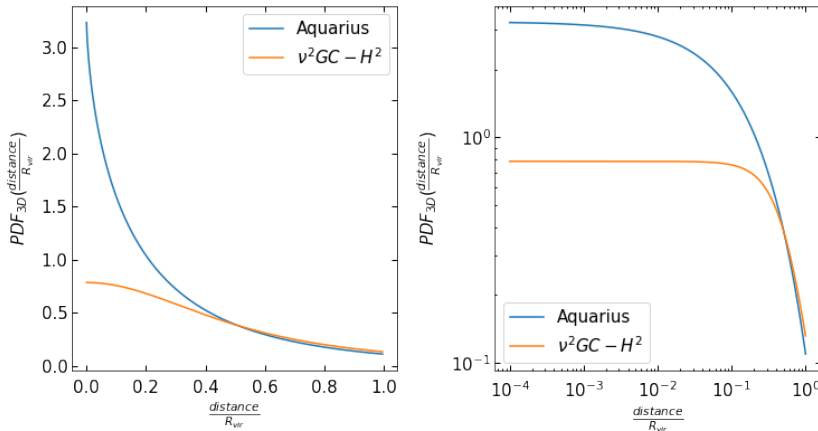


Figure 17: *Normalized density comparison of Aquarius project and $\nu^2\text{GC}-H^2$ results.*

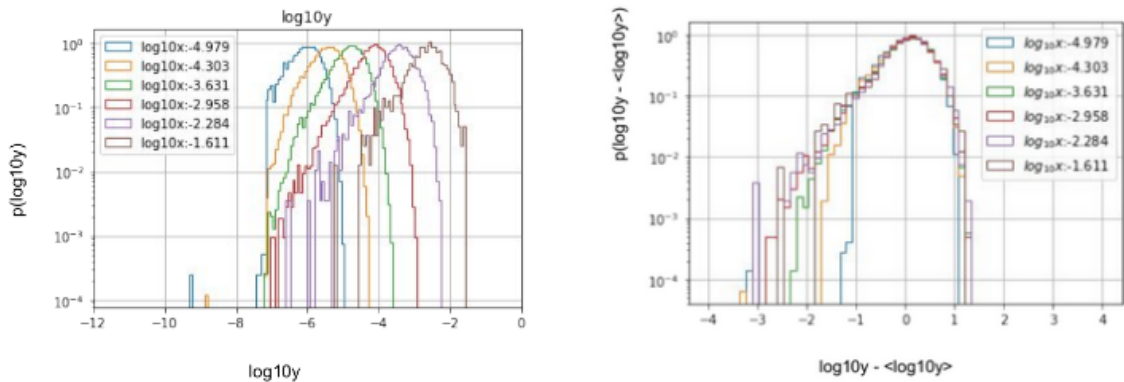
Subhalo number density profiles comparison of Aquarius project and $\nu^2\text{GC}-H^2$ results in linear(left) and logarithmic (right) scale.

This disagreement can be explained through the difference of accuracy between the two simulations, with the Aquarius simulation to be more creditable. So the Aquarius simulations results are being used for reference for the comparison of this model's results, with the range of the respected simulation to be from close to 0.01 virial radius to 1 virial radius distances.

3.1.2 Toy Model

As a first step the statistical information of the simulations results was used without attempting fitting of its subhaloes properties and subhalo spatial distribution. The model below is described as a toy model, because it has some loose physical assumptions. The N-body simulation's data with $x = \frac{m}{M_{host}}$, $y = \frac{\dot{m}}{M_{host}}$ lead to the below plots:

Figure 18: *Mass loss statistics of N-body simulation.*



Distribution of subhaloes mass loss rate values for different mass bins (left) and the distribution its difference with the respected mean mass loss rate value (right).

By fitting properly the above plots the best option is an exponential function, which is the PDF of \dot{m} (while for the main model the $\bar{\dot{m}}$ was used):

$$PDF\left(\frac{\dot{m}}{M_{host}}\right) = \frac{1}{\frac{\dot{m}/M_{host}}{\bar{\dot{m}}/M_{host}}} \cdot e^{-\frac{\dot{m}/M_{host}}{\bar{\dot{m}}/M_{host}}} \quad (3.1.5)$$

The main key result for connecting the subhaloes mass stripping with their position is the formula presented below, which resulted from the same N-body simulation.

$$CDF(r) = CCDF(\dot{m}), r = r_{subhalo}(position), \dot{m} = \dot{m}(r_{subhalo}) \quad (3.1.6)$$

So from the above relation the effects of the spatial distribution of subhaloes can be also added in the main model, by having a more accurate calculation of \dot{m} regarding the position of the subhalo and the mean value of \dot{m} . The mean value of \dot{m} is the same as the main model's formula, so the spatially \dot{m} relation is the same as before with a scale factor for different positions. At a first sight this relation seems to agree with the expected behavior of the tidal forces to be lower at higher distances from the host's center.

By knowing that the host DM halo density follows the NFW density profile it is obvious that the number of subhalos in a symmetric spherical volume would be proportional to the mass enclosed in that volume and so:

$$\begin{aligned} CDF(r_{subhalo}) \sim M(< r_{subhalo}) &\Rightarrow CDF(q) = M(q)/M(1), q = \frac{r_{subhalo}}{R_{vir}} \\ M(q) \sim \ln(1 + c \cdot q) - \frac{c \cdot q}{1 + c \cdot q} &\Rightarrow \\ CDF(q) = \frac{M(q)}{M(1)} &= \frac{\ln(1 + c \cdot q) - \frac{c \cdot q}{1 + c \cdot q}}{\ln(1 + c) - \frac{c}{1 + c}} \end{aligned} \quad (3.1.7)$$

The reason for using the variable $q = \frac{r_{subhalo}}{R_{vir}}$ (with R_{vir} being the virial radius of the dark matter host) and not $r_{subhalo}$ is because it is not affected by the r_{scale} of the host halo and can work for arbitrary massive hosts with no need for changing the formalism, while also the maximum value is 1 for all DM host cases and it is not directly affected by the R_{vir} changes for different host's masses or redshift values. The only parameter which changes in the $CDF(r)$ formula for different DM host's mass or redshift values is the host's concentration.

By using the equation 3.1.7 now it is possible to obtain the radial dependence of the subhaloes' mass loss:

$$3.1.5 \Rightarrow CCDF(\dot{m}) = 1 - CDF(\dot{m}) = e^{-\frac{\dot{m}/M_{host}}{\bar{m}/M_{host}}} \quad (3.1.8)$$

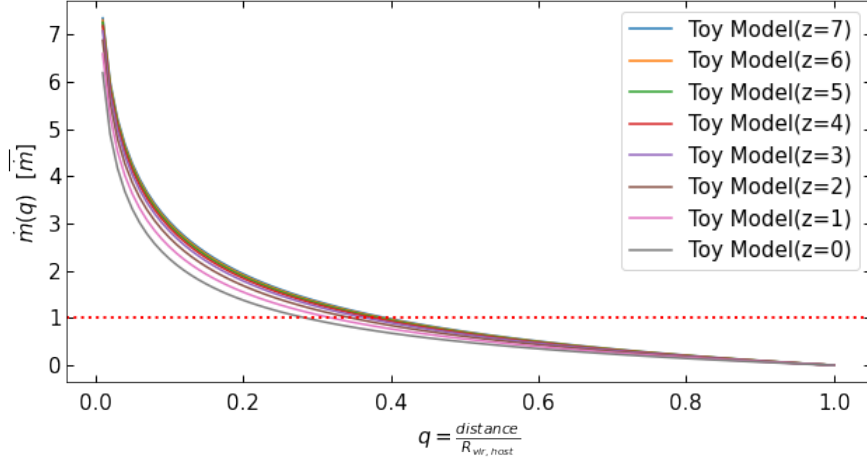
$$3.1.7, 3.1.8, 3.1.6 \Rightarrow \dot{m} = \bar{m} \cdot \ln\left(\frac{\ln(1+c) - \frac{c}{1+c}}{\ln(1+c \cdot q) - \frac{c \cdot q}{1+c \cdot q}}\right) \quad (3.1.9)$$

The mass of subhaloes at the wanted redshift can be found by solving the differential equation (D.E.):

$$\dot{m}_{sh} \cdot \frac{dt}{dz} = \bar{m}_{sh} \cdot \ln\left(\frac{\ln(1+c) - \frac{c}{1+c}}{\ln(1+c \cdot q) - \frac{c \cdot q}{1+c \cdot q}}\right)$$

where $c = c(M_{host}, z)$ is the defined halos' concentration model 2.2.4 and $\bar{m} = \bar{m}(M_{host}, m_{subhalo}, z)$ is given by 2.3.9, 2.3.10, 2.3.1 and is the mean mass loss rate. This D.E. has to be solved with initial condition $m_{sh} = m_{sh,acc}$ at $z = z_{acc}$ for a wide range of $m_{sh,acc}$ and z_{acc} values, in order to calculate the m_{sh} at a wanted z_0 for all accreted subhaloes. In comparison with the main model, the position parameter q has also to be defined for calculating the final mass of subhaloes.

Figure 19: Mass loss function toy model case.



Mass loss-subhaloes' position function for different redshift values for a cold dark matter host with mass 10^{12} solar masses. The red dotted line represents the mass loss of the model without spatial information.

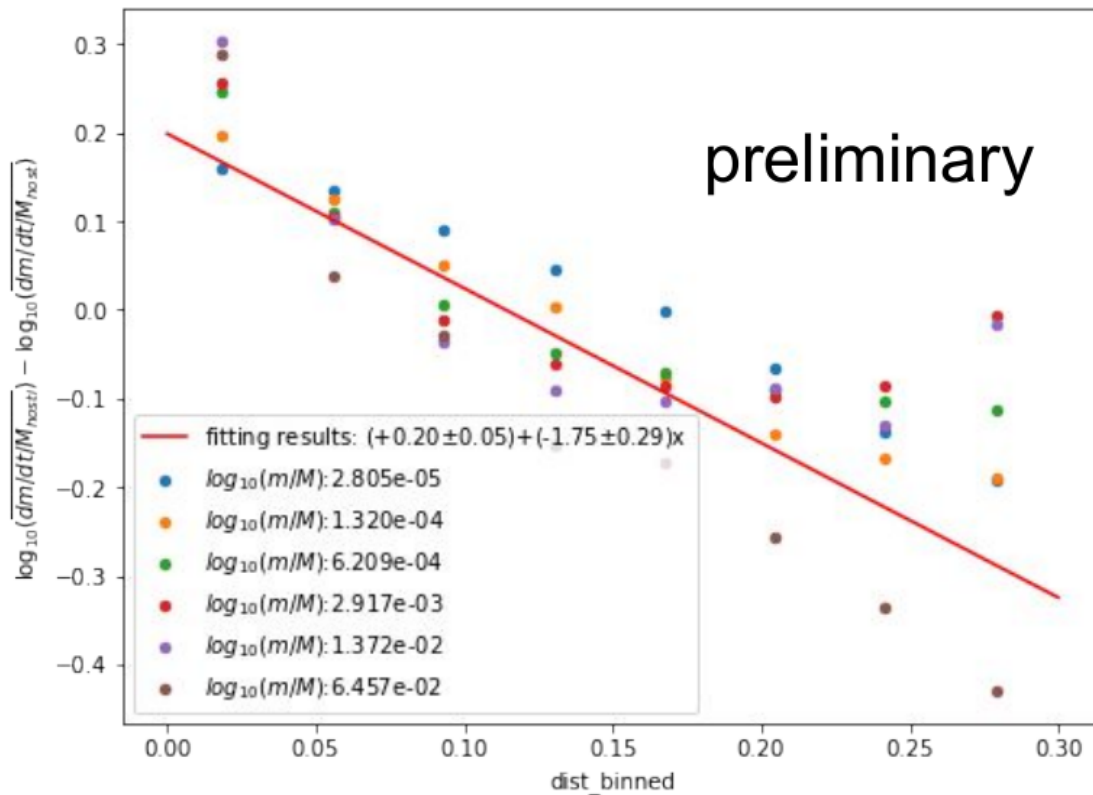
It can be seen in 19 that the behavior of the mass loss close to the center is similar to a force as a result of a classical gravitational potential (it also tends to infinity at the center of the host) but at high distance values from the host's center the mass loss rate is close to 0. This of course is not physical since the host's substructure extends further than its virial radius, so this mass loss model is reasonable for small distance values.

3.1.3 Mass loss function from simulation (second case)

For this part the subhaloes mass loss information was extracted from the mentioned N-body simulation. There is a high degree of uncertainty of the mass loss rate value due to the calculation of the truncate radius of subhaloes, there are different algorithms for this calculations based on different approximations. This result of the mass loss rate function is the best results based on the whole spatial range which is covered from the N-body simulation. This mass loss model is labeled as model 2, since model 1 is considered the initial model.

Mass loss results in contrast to subhaloes' position, the y axis is the logarithmic difference (with base 10) of the \bar{m} without spatial information and the observed $\bar{m}(distance)$ in different distances form the host's center, x axis is the distance from host's center in units of Mpc:

Figure 20: *Mass loss model case 2.*



Mass loss rate results of the N-body simulation (first case).

The above results show the deviation from the mass loss of the main model relation (mean mass loss rate for subhaloes independently from their position) for different subhaloes' mass bins. Differences between the subhaloes mass bins could indicate correlation between mass loss rate distance relation and subhalos mass but this is a reckless thought. The limitations due to the resolution of the N-body simulation can lead to wrong conclusions, interpreting calculation's effects as physical. It is shown in 20 that for different mass bins the mass loss rate is not changing with the same rate as distance is increasing but this effect will not be taken under consideration, since it is an effect of the simulation's resolution. Also, the difference of the mass loss rate from the mean mass loss rate value is observed to be relatively small for all distance values. These results leads to the new radial dependent mass loss relation:

$$\log_{10}\left(\frac{\bar{m}(d)}{M_{host}}\right)_{spatial} - \log_{10}\left(\frac{\bar{m}}{M_{host}}\right)_{initial} = f_1(d) \quad (3.1.10)$$

This relation can be transformed to a mass loss rate function:

$$f_1(d) = 0.2 \pm 0.05 - (1.75 \pm 0.29) \cdot d, d : position[Mpc] \Rightarrow \dot{m}_2 = \bar{m}(z, m_{subhalo}) \cdot 10^{f_1(d)} \quad (3.1.11)$$

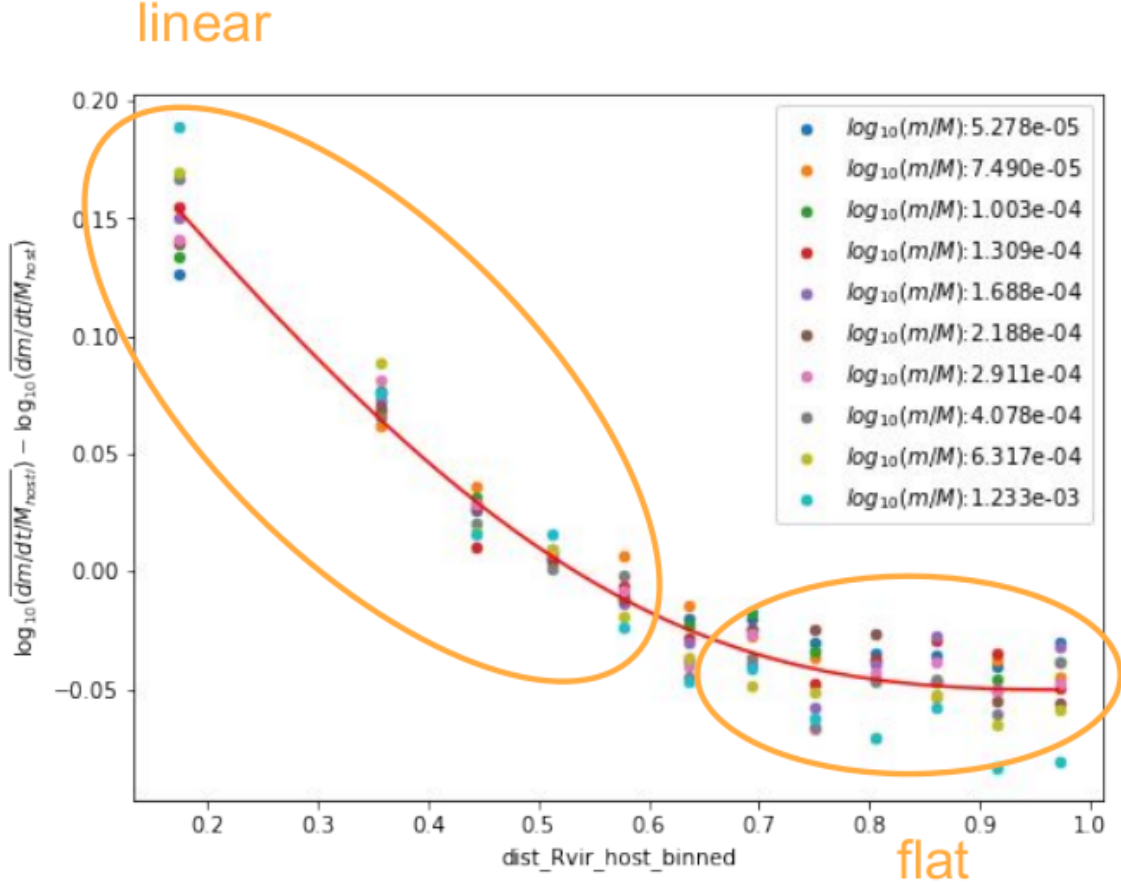
In order to have a global function for cold dark matter hosts the function $f(d)$ has to be independent from host's virial radius, and so from host's mass values. So using the value $R_{vir,host} \simeq 0.3Mpc$ of the specific host of the simulation the transformation below has to be made:

$$f_1(d) = 0.2 \pm 0.05 - (1.75 \pm 0.29) \cdot \frac{d}{R_{vir}} \cdot R_{vir}[Mpc] \Rightarrow f_1(q) = 0.2 \pm 0.05 - (0.525 \pm 0.087) \cdot q \quad (3.1.12)$$

3.1.4 Mass loss function from simulation (third case)

After using different spatial binning additional mass loss rate relations was calculated. In this part a second mass loss rate is presented with a slightly different spatial behavior from the first case.

Figure 21: *Mass loss model case 3.*



Mass loss rate results of the N-body simulation second case.

In the figure above the same formalism as before was used. It can be seen that the mass loss rate variation from the mean mass loss is linear in the inner host's area while at the outer area a plateau behavior is observed with a constant value, for $q > 0.7$, which is very different from the first case. From these results the following mass loss rate relations calculated:

$$f_2(q) = a - b \cdot (1 + (1 + q)^c)^{\frac{-1}{c}}, q = \frac{distance}{R_{vir,host}} \quad (3.1.13)$$

with $a = 1.34 \pm 0.07, b = 1.39 \pm 0.07, c = 2.87 \pm 0.1$

$$\dot{m}_3 = \bar{\dot{m}}(m_{subhalo}, M_{host}, z) \cdot 10^{f_2(q)} \quad (3.1.14)$$

An important comment for the results above is that the data which were used were in the range $q \in [0.2, 1]$ and an extrapolation was used for the range $q \in [0, 0.2)$. This approach is not well physically justified and it should not easily trusted without further study.

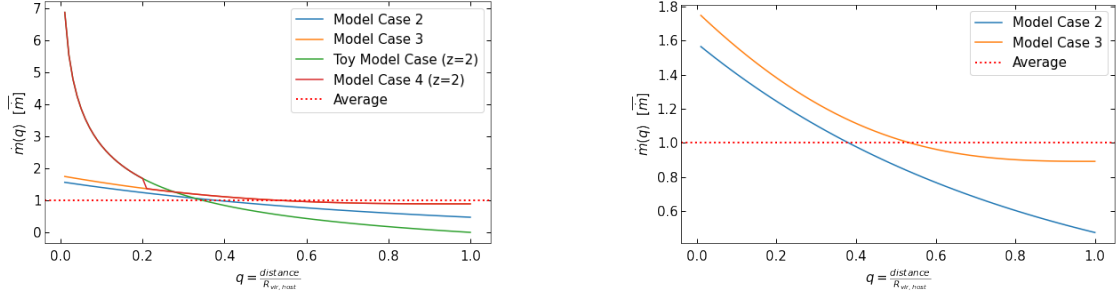
3.1.5 Mass loss function combining simulation's results with the toy model

The mass loss rate of the previous section is trustworthy only for $\frac{distance}{R_{vir,host}} \in [0.2, 1]$ and for the $[0, 0.2]$ spatial area instead of an extrapolation a different approach can be followed. For the inner area the toy model is used while for the outer area the mass loss rate of case 3, this process is more physical and solves the problems of each case alone.

$$\dot{m}_4(q) = \begin{cases} \bar{\dot{m}}(m_{subhalo}, M_{host}, z) \cdot \ln\left(\frac{\ln(1+c(z)) - \frac{c(z)}{1+c(z)}}{\ln(1+c(z) \cdot q) - \frac{c(z) \cdot q}{1+c(z) \cdot q}}\right) & 0 \leq q \leq 0.2 \\ \bar{\dot{m}}(m_{subhalo}, M_{host}, z) \cdot 10^{f_2(q)} & 0.2 \leq q \leq 1 \end{cases} \quad (3.1.15)$$

Below all the mass loss rate models described so far are presented for comparison.

Figure 22: Mass loss function models.



Mass loss functions used in this project with all models (left) and the N-body simulations mass loss functions only (right), with the red dotted line to be the mean mass loss value.

The mass loss for the model 4 and toy model cases have much higher values near the host's core while the other two cases have a linear relation with no high difference between the value at the center and at the virial radius (but also all its values are close to the mass loss mean value).

3.2 How the spatial information is added in the model

The main model assigns weights to subhaloes based on the Yang model at accretion. The weights of each subhalo are calculated by the Yang model and they are dependent on the subhalo mass at accretion, accretion redshift, "final" host mass and "final" redshift. These weights are completely independent from subhalo masses after the tidal stripping and are the same regardless the position of the subhaloes and the tidal stripping process. Due to the independence of Yang weights from the orbital radius of the subhaloes an additional weight term has to be added, without a spatial dependent term the model is not physical.

In this project the weights of subhaloes are calculated by the Yang model only once and the final mass after the tidal stripping process for different radial values, while the radial values "cover" uniformly all the values in $[0, R_{vir,host}]$. Each radial value has an additional probabilistic term which follow the subhaloes spatial distribution at the wanted ("final") redshift for a defined host halo. Due to the absence of mass segregation effects this additional term does not depend on the subhalo masses and is the same for all subhaloes. Each of those radial cases have the same Yang weights and so their weights need to be normalized by dividing with the number of radial values in the end.

After the calculation of the final masses and the Yang weights the total weights of each subhalo is defined by the probability function of the final position of the subhalos. The mathematical relation which describes the above process is the relation with P_{Yang} being the weights of Yang model, $P_{spatial}$ being the weights due to the initial radial distribution of the subhaloes and P_{total} being the final weight of each subhalo:

$$P_{Yang} = P_{Yang}(m_{subhalo}(z = z_{acc}), z_{acc}, z_0, M_{host}(z_0)), P_{total} = P_{Yang} \cdot P_{spatial}\left(\frac{distance}{R_{vir,host}}\right) \quad (3.2.1)$$

3.3 How the final distribution of subhaloes is defined

A common simplistic assumption for the spatial distribution is that subhaloes follow the same NFW density profile as the host's dark matter particles at a given redshift. This assumption is followed also in this model:

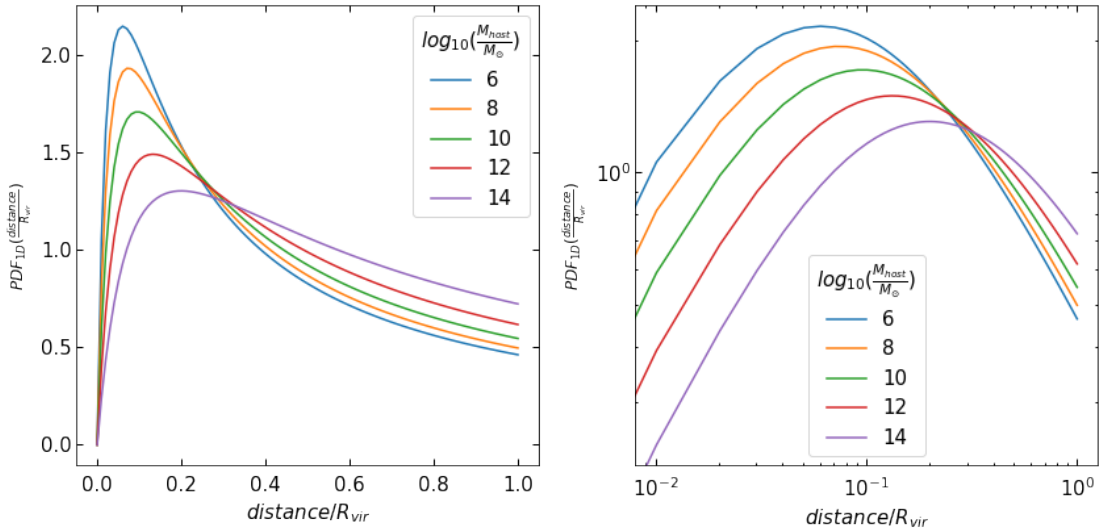
$$\begin{aligned} CDF(r_{subhalo}) &\sim M(< r_{subhalo}) \Rightarrow CDF(q) = M(q)/M(1), q = \frac{distance}{R_{vir,host}} \\ M(q) &\sim \ln(1 + c \cdot q) - \frac{c \cdot q}{1 + c \cdot q} \Rightarrow CDF(r) = \frac{M(q)}{M(1)} = \frac{\ln(1 + c \cdot q) - \frac{c \cdot q}{1 + c \cdot q}}{\ln(1 + c) - \frac{c}{1 + c}} \\ \Rightarrow PDF(q) &= \frac{d}{dq}(CDF(q)) = \frac{1}{M(1)} \cdot \frac{q \cdot c^2}{(1 + c \cdot q)^2} \end{aligned} \quad (3.3.1)$$

The linear probability density function of subhaloes' position is preferred from the volume (three-dimensional) probability density since for the first one $\lim_{q \rightarrow 0} PDF_{1D}(q) = 0$ and the latter one $\lim_{q \rightarrow 0} PDF_{3D}(q) = \infty$. The probability density function depends, beside the distance quantity q , on the concentration of the host which is depending on host's redshift and mass. The quantity $M(1)$ is the virial mass of the host and acts as a normalization constant of the function.

The weights which are used for the subhaloes are based on the given PDF are:

$$P_{spatial}(q) = PDF_{1D}(q) \cdot dq \quad (3.3.2)$$

Figure 23: Subhaloes' distance PDF (NFW).



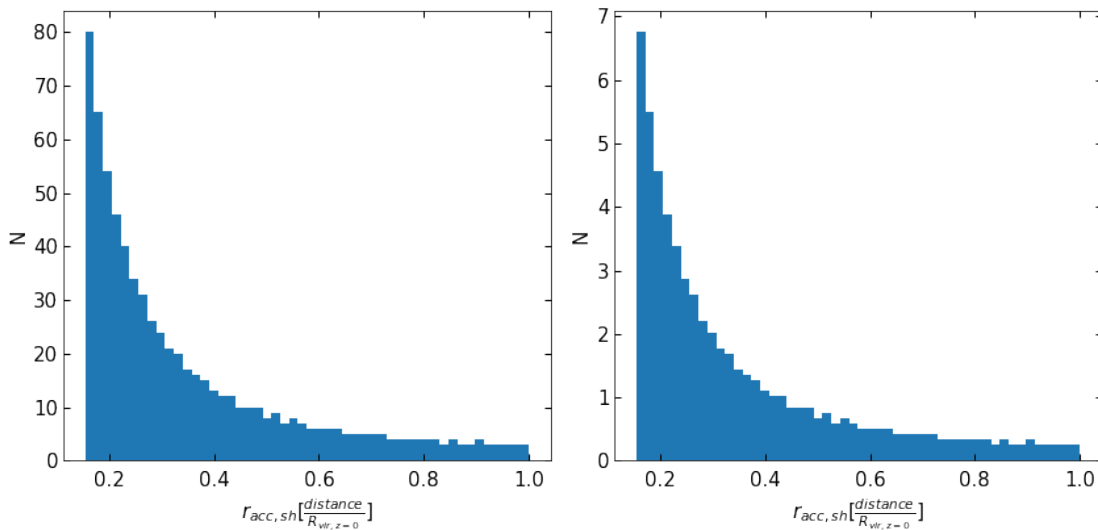
Probability density function based on the NFW density profile, for a host halo with different mass values at $z=0$ in linear (left) and logarithmic (right) scale.

The main assumption which is used for now is that the subhaloes are following the above radial density profile regardless the infall redshift and infall distance of subhaloes from the host's center. The latter assumption means that the host's spatial evolution is also ignored, since as the redshift is getting lower the mass of the host is increasing and so its volume.

3.4 Adding more information in the model

In this section more information is used in the model beside the previous assumptions, based on well defined physical characteristics of dark matter haloes. A key effect that is not considered in the previous defined model is the accretion position of subhaloes for different accretion redshift values.

Figure 24: Subhaloes accretion position.



Accretion position of subhaloes for different accretion redshift values for $z \in [0, 7]$ with $dz=0.05$ for a host halo with mass $10^{12} M_\odot$ (left) and normalized (right).

Accretion is happening for subhaloes which are placed near the virial radius of the host (0.8 to 1.2 host's virial radius is a realistic assumption) at that time (accretion redshift). The radius at $z=7$ is 0.13 times the host's virial radius at $z=0$, it would be reasonable to expect subhaloes with smaller accretion position to be placed closer to the host's center. Also, the accretion positions at higher than redshift equal to 2, or distance smaller than 0.4 virial radius, are highly concentrated close to the host's center while outside this range or redshift (and accretion position) values the differences are much higher.

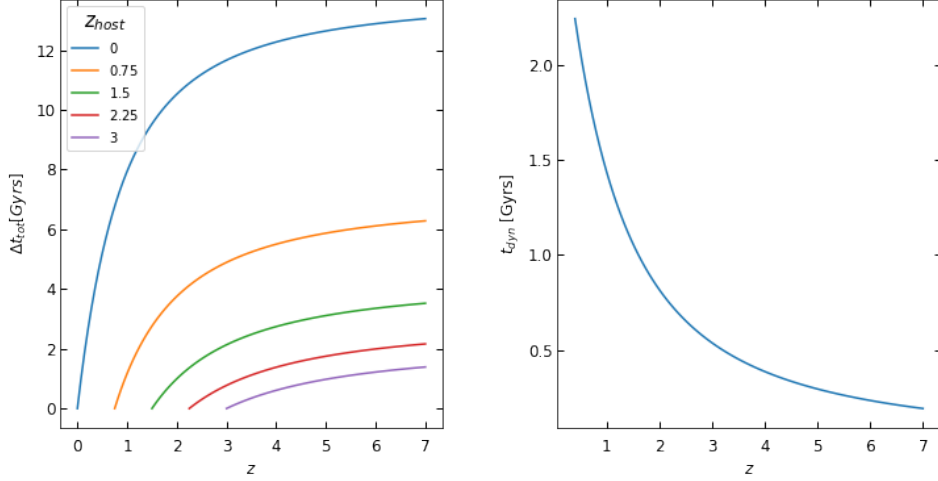
An additional important term which affects this spatial bias is the redshift difference from accretion to the "final" redshift. The more time a subhalo orbits, which means that those subhaloes have completed more orbits, the more close their spatial distribution is expected to be to the NFW density profile and their minimum position to the host's center. For quantifying the number of subhaloes' completed orbits for a given accretion redshift, the quantities of look back time and the subhalos dynamical timescale have to be defined from previous work [46].

$$t_{dynamical}(z) = 1.628 \cdot h^{-1} \cdot \left(\frac{\Delta_c(\Omega_z - 1)}{178.0} \right)^{-0.5} \cdot \left(\frac{Hz(z)}{H_0} \right)^{-1} \quad (3.4.1)$$

$$lt(z) = \int_{z_i}^{z_f} \frac{-1}{(1+z) \cdot Hz(z)} dz, \quad z_i > z_f \quad (3.4.2)$$

Both look back time (lt) and dynamical timescale ($t_{dynamical}$) depend only on redshift and the cosmological parameters, which in this project are the common values of the Λ CDM model.

Figure 25: Redshift effects on subhaloes.

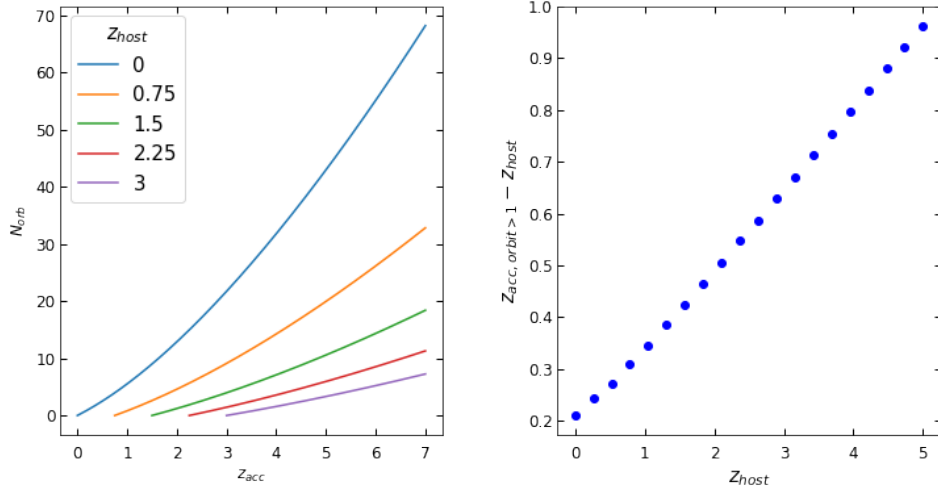


Look back time (left) and dynamical timescale of subhaloes for different redshift values (right).

Based on the two above plots the number of orbits of subhaloes can be defined as:

$$N_{orbits}(z_{acc}) = \frac{lt(z_{acc})}{t_{dynamical}(z_{acc})} \quad (3.4.3)$$

Figure 26: Subhaloes completed orbits.



Number of orbits of subhaloes for different subhaloes accretion redshift (left) and minimum accretion redshift value of subhaloes for one orbit to be completed.

The models' assumptions are not physically grounded for subhaloes which have not completed at least one orbit and so they have not reach equilibrium. In reality, a subhalo needs more than one orbit in order to reach its equilibrium orbit but for simplicity the one orbit condition is used, since after one orbit a subhalo losses a high fraction of its mass.

The ways for increasing the agreement of subhaloes' spatial distribution results of this model with the expected distribution of Aquarius project can be split in two categories. Firstly, some preferable values of the used parameters are tested. The concentration in the PDF_{1D} function of the NFW profile can lead to subhaloes' spatial distribution results closer to the wanted Einasto profile, assuming that subhaloes can show slightly different gravitational bounding from the dark matter particles with the host halo and thus subhaloes follow different trajectories than dark matter particles (with the latter to follow the NFW profile of the host with its concentration at $z=0$). Also the subhaloes with number of orbits smaller than 1 could be neglected due to the uncertainty and use a different approach for them. The other category is by adding an abstract spatial condition in the model and after fitting with the wanted Einasto profile, to try to translate it to physical quantities. As it can be seen from the results' section the latter approach is the most successful.

3.5 Results and application of the model

The defined model so far is suitable for cold dark matter haloes' substructure, regarding that the used N-body simulation's information is the result of cold dark matter haloes. But this model can be expanded to the warm dark matter case assumed that spatially there are no high differences from the cold dark matter case and the mass loss remains the same. The main difference between CDM and WDM models is due to the free streaming effects, which happen only for cases of low mass dark matter particles, leading the warm dark matter substructure to be much less than the cold dark matter case and biased to higher subhalo mass values. The huge number of low mass subhalos of the CDM case are not present in the WDM substructure as a result of the top to bottom structure formation. Additionally, the model with the extra information is applied, while in general the most interesting cases of WDM particles lies in the range of few keV and so the results are presented for the 1.5 and 3 keV cases. But there is not an extensive study of warm dark matter substructure like the Aquarius project for CDM, so the results cannot be tested and be trusted since further studies are needed for that.

The results of this model contain the spatial distribution and the distributions of important characteristics of subhaloes such as their concentration, density and scale radius. These results are studied for all the mass loss cases introduced in this thesis and also for a model with additional information. In more details, the main quantities of dark matter substructure which are shown are the mass function, the subhaloes number density and satellite galaxies formed in subhaloes.

An important application of this model is the calculation of the substructure's gamma-ray emission. Although there is high uncertainty regarding the interactions of dark matter particles there are theoretical models involving WIMPs annihilation channels which can possibly lead to the production of photons. If dark matter particles emits light it may be possible to detect a signal, which would be an indirect detection of dark matter and would prove its existence. For this reason the annihilation boost factor, which is the substructure's luminosity in units of host's luminosity, is calculated and the spatially dependent boost factor function can be found. This function is calculated for not only the new model with the additional information but also for the toy model and model 4 cases of mass loss, in order to test the effects of the different models in the final result. A further applications of this boost factor function which is shown is the possible luminosity templates of the substructure's photons, as a 2D projection of the total substructure enclosed in the virial radius of the host. These results can contribute to indirect searches of dark matter through luminosity observations from galactic halos or can be used as a toy model for testing the observational constraints and signal analysis techniques for dark matter particles.

4. Results

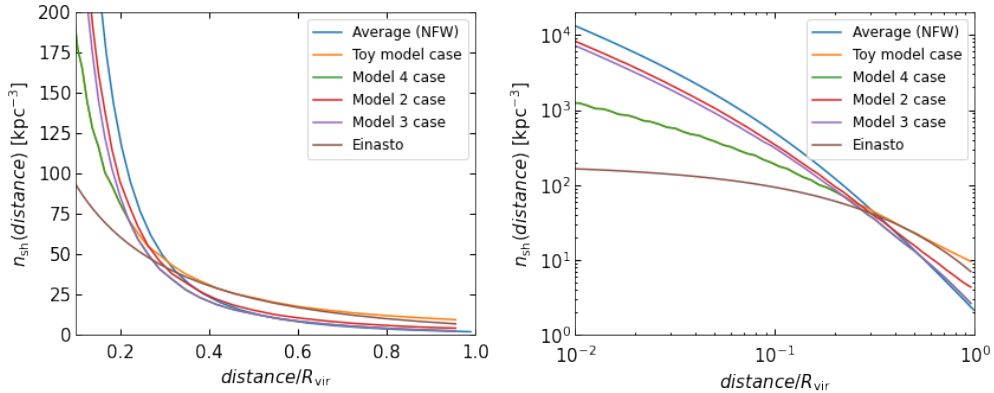
In this section all the results of the model defined previously are presented. In the first part the results of the main assumptions are presented and then an extensive study of the resulted subhaloes' characteristics are shown in order to detect and mention the possible problems. Next, the cases with additional information are presented and discussed. Also the warm dark matter results are presented. Finally, the main application of the model is presented regarding the dark matter gamma ray emission.

4.1 Cold Dark Matter Case

The results of the dark matter subhalos for the cold dark matter case are presented. The main part of results which is the most important is the spatial distribution of the subhaloes.

4.1.1 Basic model's assumptions

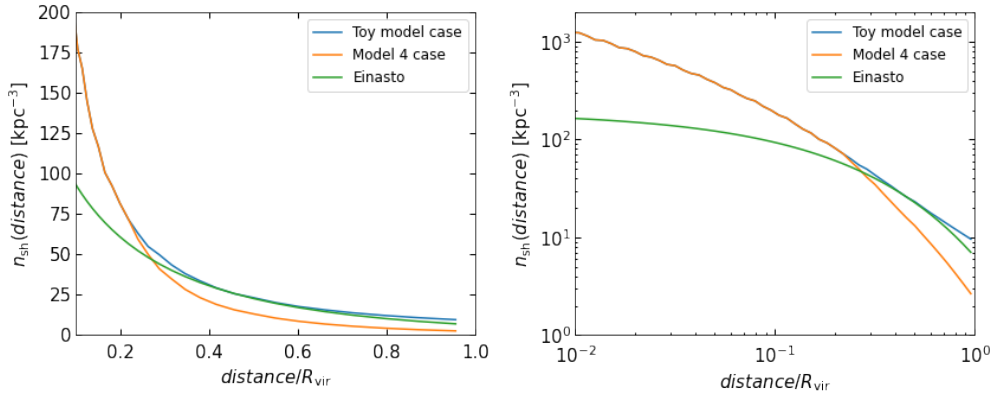
Figure 27: Subhaloes' number density.



Subhaloes' number density for a dark matter host with 10^{12} solar masses at redshift $z=0$ for all the presented mass loss models.

The mass loss models 2 and 3 cases disagrees by a large magnitude with the expected Einasto profile, while the other cases seem better and a closer look is needed.

Figure 28: Subhaloes' number density (closer look).

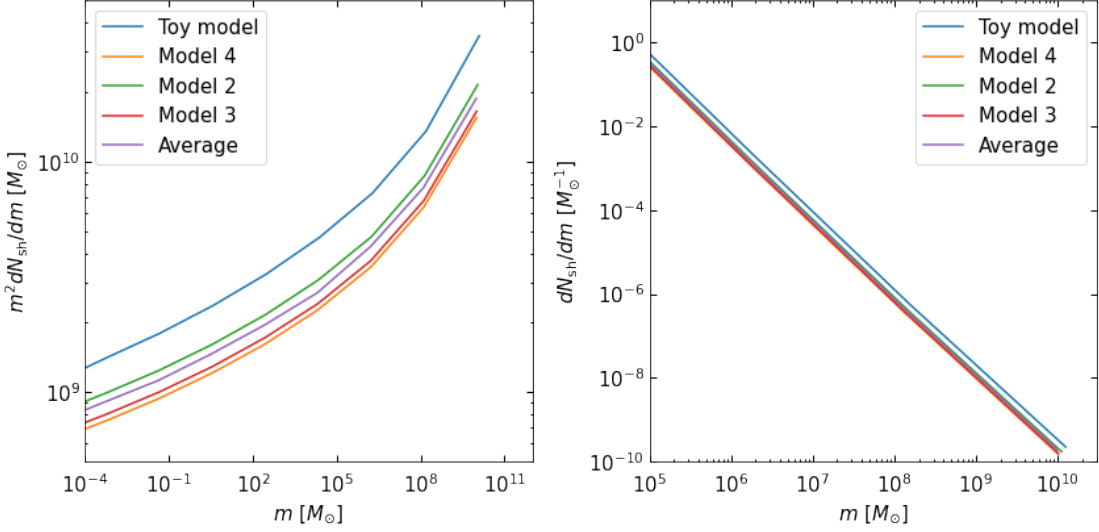


It is obvious that the mass loss model 2 and 3 did not lead to realistic subhaloes' number density and are very similar to the NFW profile, while the expected result is the presented Einasto

profile. The model 4 and toy model cases are closer to the expected profile near the core, while far from the core the toy model is close to the Einasto profile and the model 4 is close to the NFW profile.

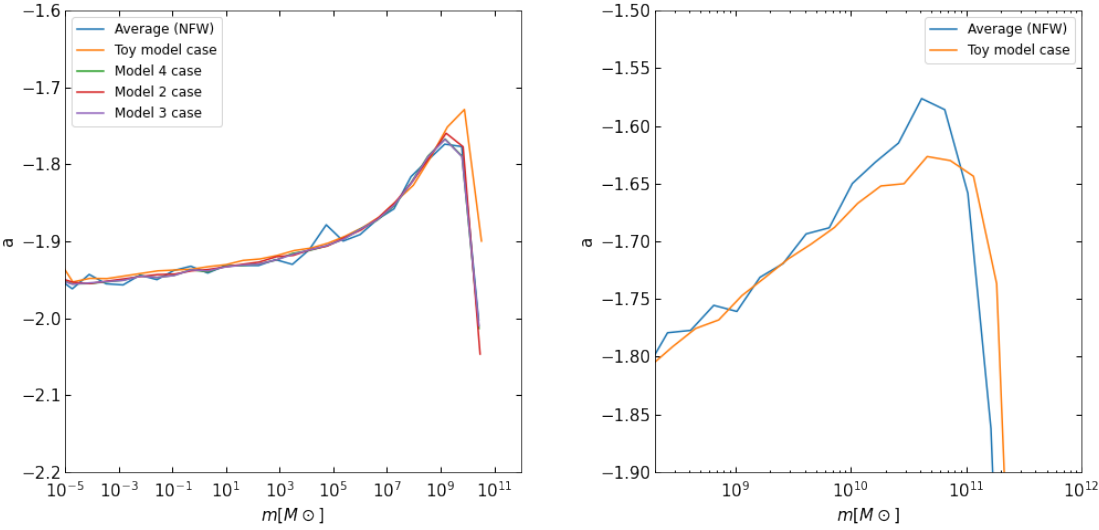
Another important quantity of the host's substructure is the mass function, which shows the mass distribution of subhaloes and is the quantity $m_{sh}^2 \frac{dN_{sh}}{dm_{sh}}$. The number of subhalos for different mass values in general is expected to follow the relation $\frac{dN_{sh}}{dm_{sh}} \sim m_{sh}^{-\alpha}$. An additional quantity of the mass function is this α parameter which is called slope of the mass function and can be calculated by $\alpha = -\frac{d\ln(dN_{sh}/dm)}{d\ln m}$.

Figure 29: Subhaloes' mass function.



Mass function of substructure(left) and the satellite galaxies with formation condition of maximum velocity higher than 18 km/s(right) for all mass loss models.

Figure 30: Subhaloes' mass function slope.



Mass function slope for all models(left) and closer look for the toy model and average model at the high mass subhalo values area(right).

The mass loss model 2 and toy model only seem in 29 to have higher mass function than the initial model, with the toy model to have much more massive subhalos. The expected mass function, and also the respected slope, has to be generally close to the initial model and all mass models satisfy this criterion expect the toy model. This effect leads to much higher subhalo mass fraction as it can be shown in 31 for the toy model, with the initial model's mass fraction to be close to 0.1, while the other mass loss models are close to the initial model's result.

Figure 31: Subhaloes' mass fraction.

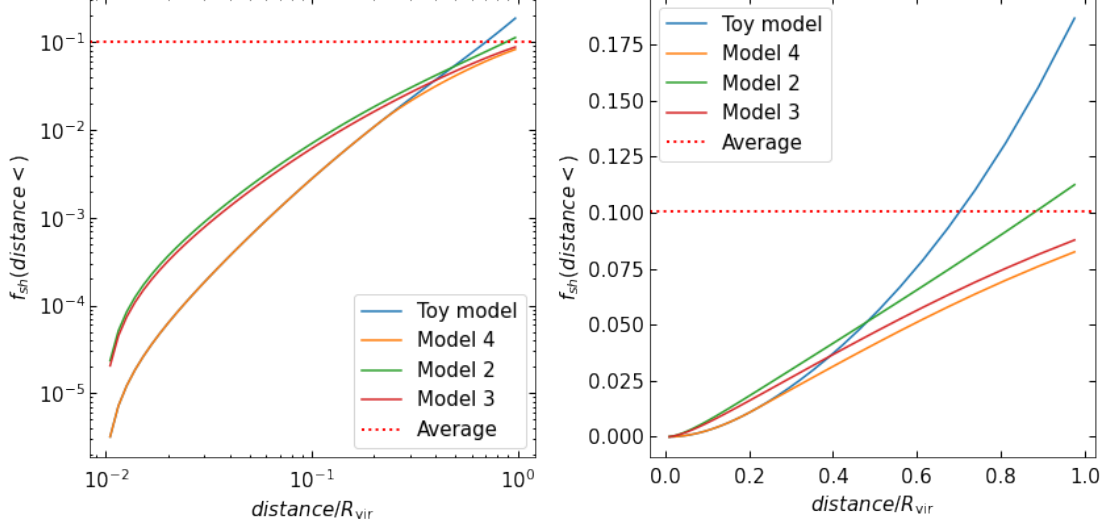
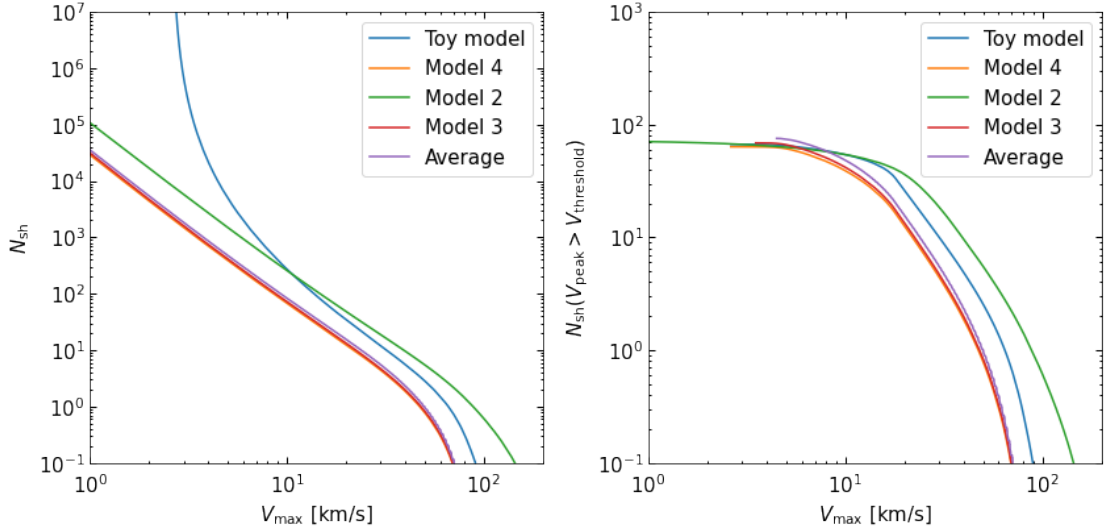


Figure 32: Satellite galaxies.



Subhaloes' maximum velocity cumulative distribution (left) and with the additional condition of $V_{sh,peak} > 18\text{ km/s}$ which form a satellite galaxy (right).

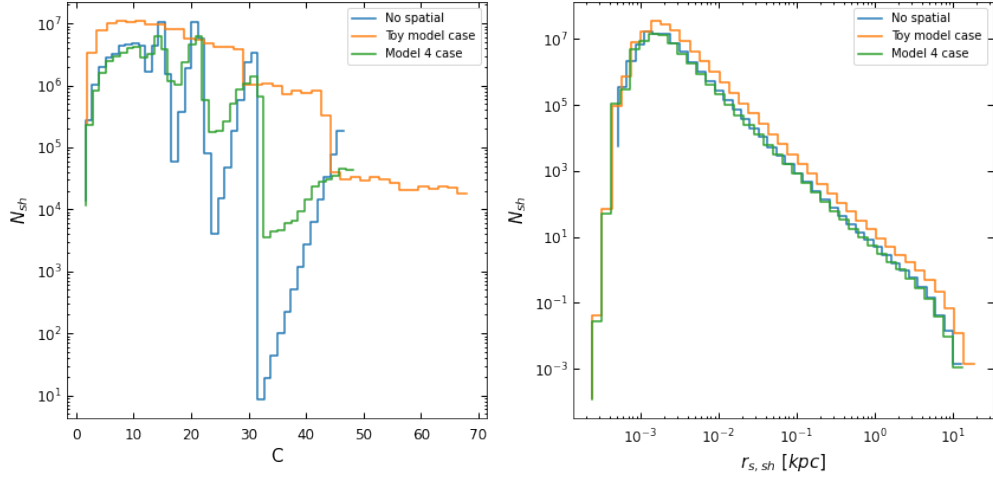
It is expected that some of the subhalos are able to form satellite galaxies. A "satellite-forming condition" has to be applied to subhalos with a simple case to be the $V_{sh,peak} > 18\text{ km/s}$, which roughly corresponds to the threshold of hydrogen cooling. It is obvious in 32 that the number of satellites galaxies which please this given condition do not differ importantly for different mass loss

rate models.

4.1.2 Subhaloes characteristics' distributions

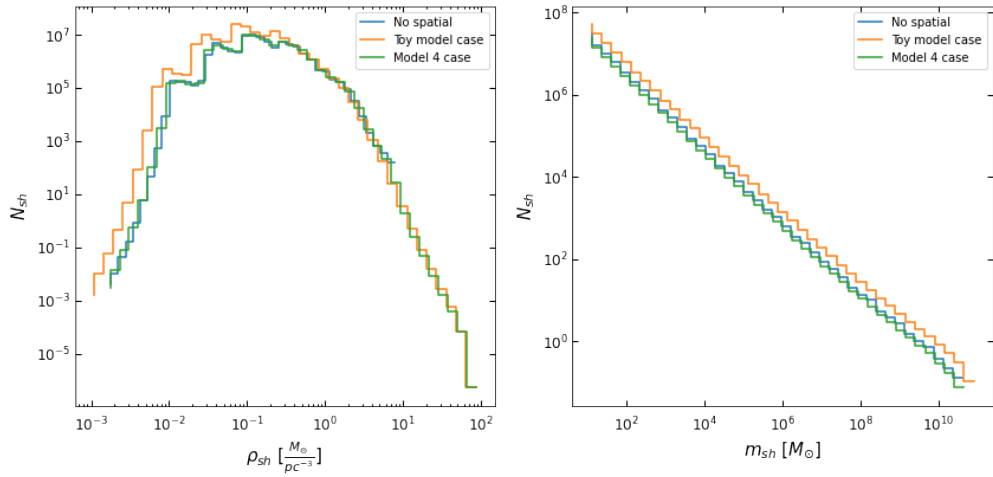
So far it is obvious that the expected plateau behavior of the subhalos number density at the area near the host core can be seen only for the toy model and model 4 case of mass loss models. These models are the most prominent for accomplishing the expected Einasto profile, with the toy model to have better agreement far from the core. But regarding the mass function results it can be seen that the toy model leads to much higher substructure mass while the mass function slope at the range of high mass values also disagrees with the model with no spatial information. For this part the toy model and model 4 results have to be studied further for choosing the most prominent model.

Figure 33: *Subhaloes concentration and scale radius statistics.*



Subhaloes' concentration (left) and scale radius (right) distribution for the toy model and model 4.

Figure 34: *Subhaloes density and mass statistics.*

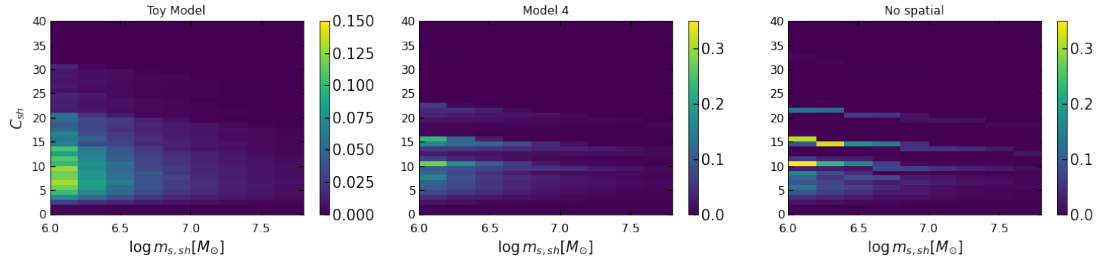


Subhaloes' density (left) and mass (right) distribution for the toy model and model 4.

Regarding the subhaloes properties distributions the subhaloes density, mass and scale radius have good agreement for both models with the expected behavior of the initial model. A difference is observed in the subhaloes' concentration distribution, the toy model has a very different distribution from the expected reaching much higher concentration values. The model 4 case is close to the initial's model results but there are also differences, which suffer also from effects of the less substructure of model 4 results. The toy model concentration results can be explained from the toy model mass loss relation, at the outer area of the host the mass loss tends to 0 and so these subhaloes do not experience any tidal forces and so mass loss.

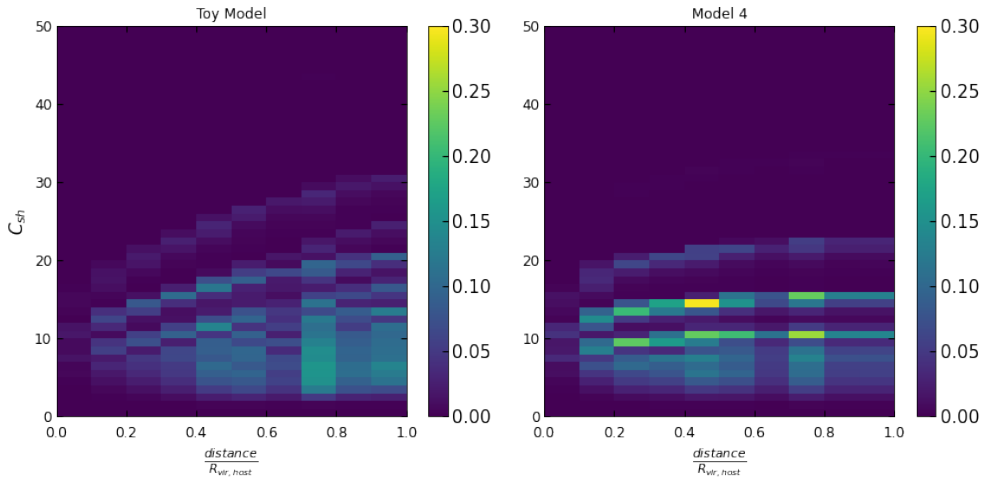
A more extensive study of the effects of each mass loss model on subhalos concentration results has to be shown in order to identify potential problems and the most prominent cases for further study.

Figure 35: Subhaloes' concentration and mass histogram.



Two-dimensional histogram of subhaloes mass and concentration for the mass loss function cases of toy, model 4 and initial.

Figure 36: Subhaloes' concentration and position histogram.



Two-dimensional histogram of subhaloes' position and concentration for the mass loss function cases of toy and model 4.

It can be seen that the subhalos mass-concentration relation is almost identical between the initial model and model 4 mass loss cases but the toy model's result differs significantly again. Due to the large decrease of subhaloes' number as subhaloes mass bins increased the mass range $[10^6, 10^8]$ solar masses was chosen, the same 2D distribution holds identically in the other mass ranges. The toy model have a close to uniform concentration distribution for a given subhalo mass value, while the other cases show discrete values of concentration to be highly probable. The 2-dimensional histogram of subhaloes' concentration and position of toy model and model 4 cases

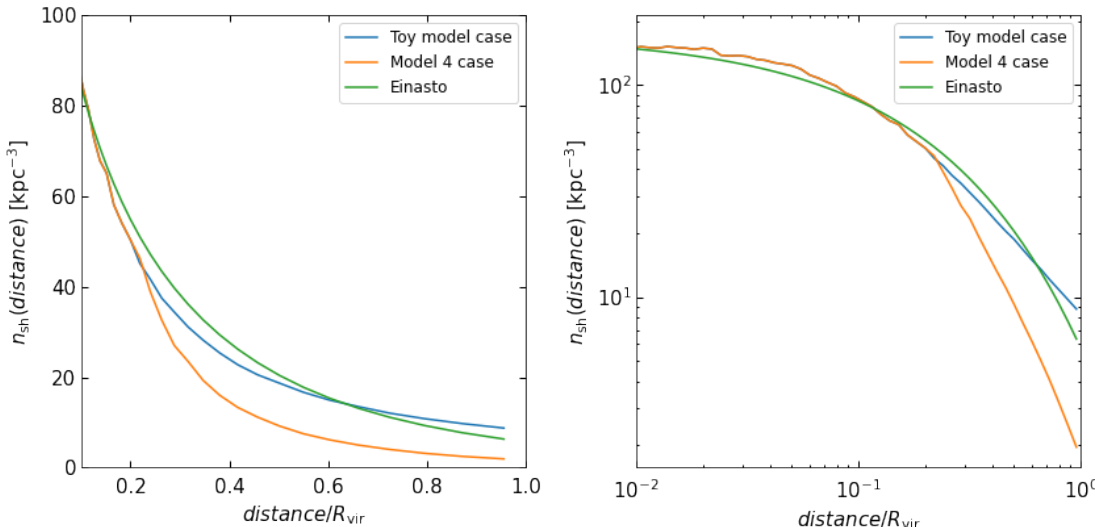
do not show very different behavior but the concentration of the toy model can be seen again to reach higher values. The toy model mass loss shows problems regarding the subhalos concentration values and the model 4 case would be preferable.

4.1.3 Preferred variable values

In this section different parameters' values and ranges are tested in order to correct the model's disagreements with the wanted results.

From the figure of subhalos accretion redshift in contrast to at least one orbit has completed, for a host with redshift $z=0$, subhaloes with smaller than 0.2 accretion redshift do not have completed a full orbit in the host halo. In this small redshift range $z \in [0, 0.2]$ the results of the model with the basic assumptions is not trustworthy. The spatial distribution of subhaloes when the subhaloes with accretion redshift in this range are excluded is presented below for the mass loss models of the toy and 4 cases.

Figure 37: Subhaloes number density with orbital condition.

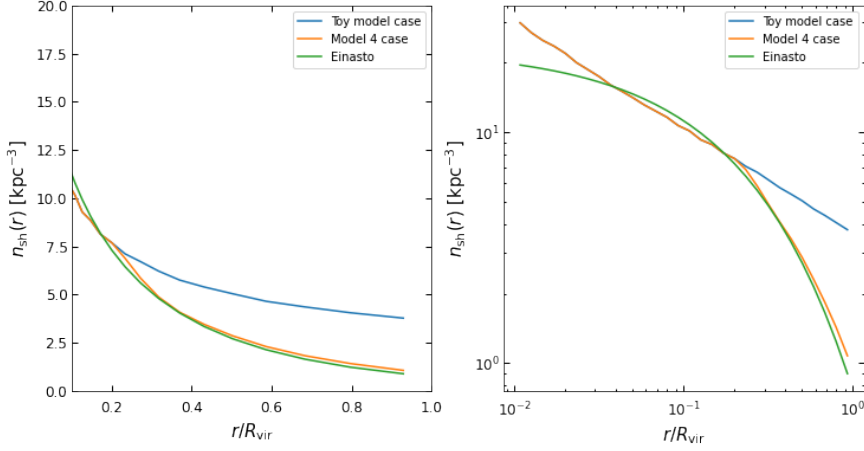


Subhaloes number density for a dark matter host with 10^{12} solar masses at redshift $z=0$ for subhalos with accretion redshift higher than 0.2, only for the mass loss models toy and 4.

With the condition of subhaloes which have not completed at least one orbit to be excluded, the number density of the toy model and model 4 mass loss models have a better agreement with the expected Einasto profile. This condition was tested to hosts at higher redshift values and this relation leads to the same improvement, the number density having a plateau behavior near the core area. The toy model as it is shown in the previous subhaloes distributions' results do not agree with a variety of expectations but in this case it has the best agreement with the wanted spatial distribution.

If the same spatial distribution at the outer host's spatial area was the case for the model 4 case the result would be more acceptable. This result could be shown with changing the NFW final distribution profile of subhaloes with a fixed concentration $c=1$. This extreme and non realistic value physically means that $R_{vir} = R_{200}$ and do not represent an expected condition by far. Practically this condition leads to substructure to be biased to outer host's area. As it can be seen the model 4 mass loss case has an almost perfect agreement with the Einasto profile far from the host's core but at the inner host's area fails to follow the wanted behavior. A more physically realistic case of low c value in the NFW would be at least higher than ~ 2 , which is the value of a host at its early evolution stages (z higher than 7). This condition could be translated as a different gravitational bounding between dark matter particles of the host and its substructure, but this condition is not observed in N body simulations.

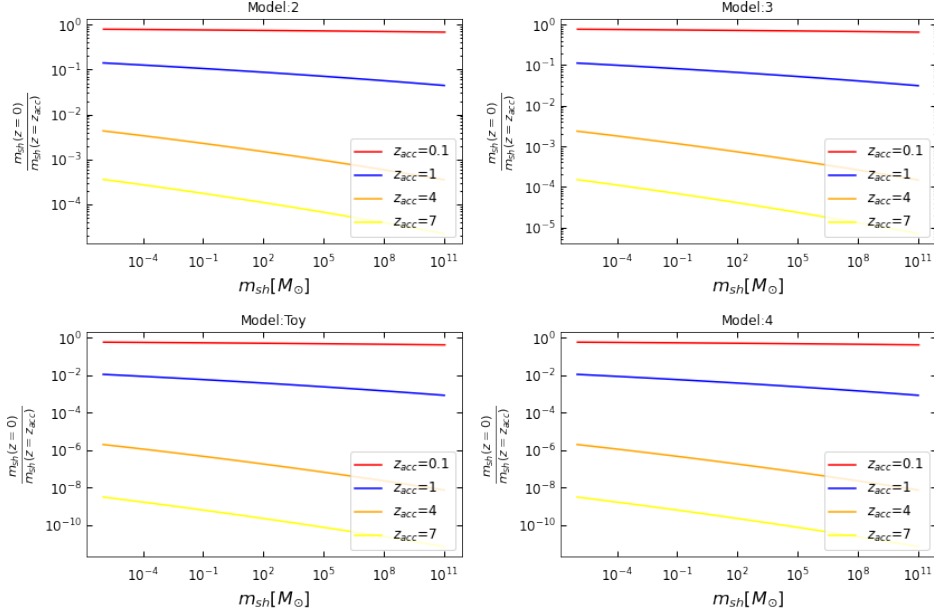
Figure 38: Subhaloes' number density with different host's concentration condition.



Subhalos number density for a dark matter host with 10^{12} solar masses at redshift $z=0$ with the host's NFW profile to have concentration parameter $c=1$, only for the mass loss models toy and 4.

Although choosing parameters' values for getting the wanted spatial results and be justified, as a fine tuning problem with physical explanation, the toy model mass loss function at the inner host's area (and so model 4) shows nonphysical results.

Figure 39: Mass loss rate effects of all models.



The fraction of final mass, after the total tidal stripping, of subhaloes to their mass at accretion for all the mass loss models at the host's inner area at $0.1 R_{vir}$ distance, for different subhalos accretion redshift values.

For the mass loss of toy model (and model 4) the subhalos with accretion redshift higher than ~ 4 are almost destroyed or at least suffered huge mass loss while the other models do not show such extreme mass stripping. For distances even closer than $0.1R_{vir}$ the subhaloes suffer even

more mass stripping for these mass loss models. As a result, the high mass subhalos near the host's center have to be accreted at a redshift close to the final redshift value. This behavior is not expected and subhalos with different accretion redshift contributes to the inner host's substructure density. This approach of a mass loss model similar to the toy model near the host's center would be applicable only in case of different mass stripping theoretical expectations than the current ones will be observed.

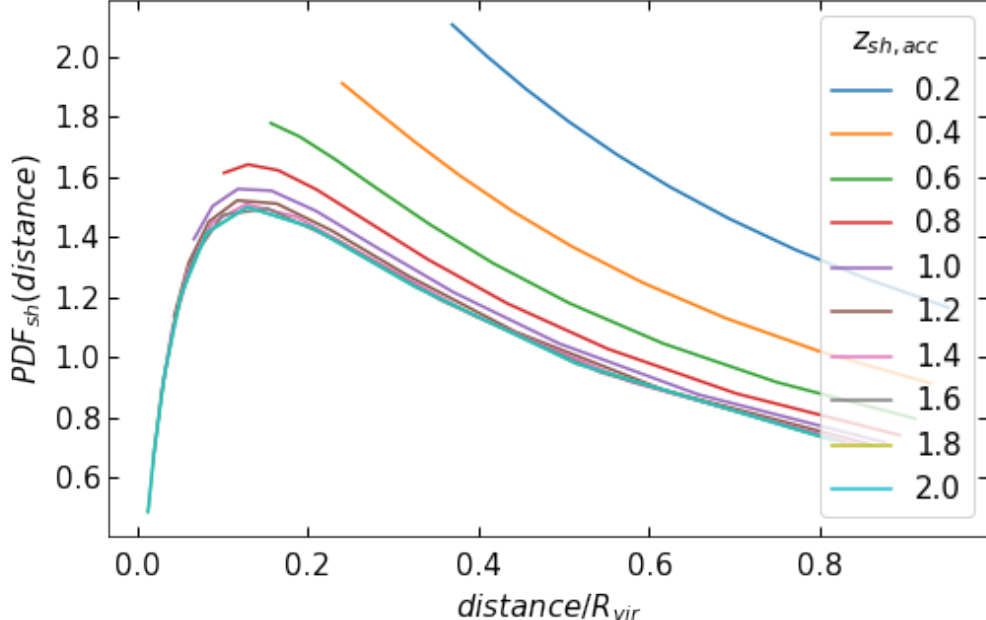
4.1.4 Adding more information in the model

An additional process was added to the model by adding a spatial condition dependant to subhaloes accretion redshift. This approach was successful only for the mass loss model case 2 and in this section only this mass loss model is used. The way this condition affects the subhalos positions is by imposing a minimum position q_{min} of subhalos, while for positions higher than q_{min} the subhalos follow the host's NFW spatial distribution. This condition is the result of fitting given that the wanted spatial distribution result is the defined Einasto profile and is:

$$q_{min}(z_{acc}) = \frac{1}{2} \cdot e^{-2 \cdot z_{acc}}, q = \frac{\text{distance}}{R_{vir}} \quad (4.1.1)$$

Considering the minimum distance from the host's center to be 0.01 host's virial radius, for subhaloes having q_{min} smaller than this value the subhaloes minimum position is defined to 0.01 since smaller distances from the host's center lies outside the model's range.

Figure 40: *New model subhaloes spatial weights.*

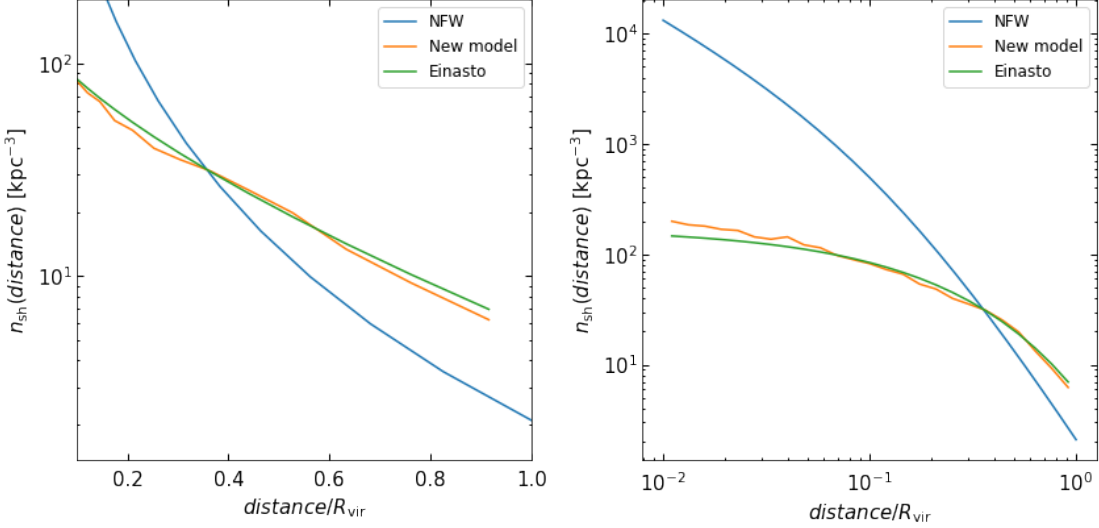


Subhaloes radial probability density function based on the NFW density profile of a host, with mass 10^{12} solar masses at $z=0$, after the addition of the q_{min} condition for different subhalos accretion redshift values.

This model is labeled as new model and is the best case of this project regarding the substructure's spatial distribution.

The same plots as previously presented are shown here for this new model.

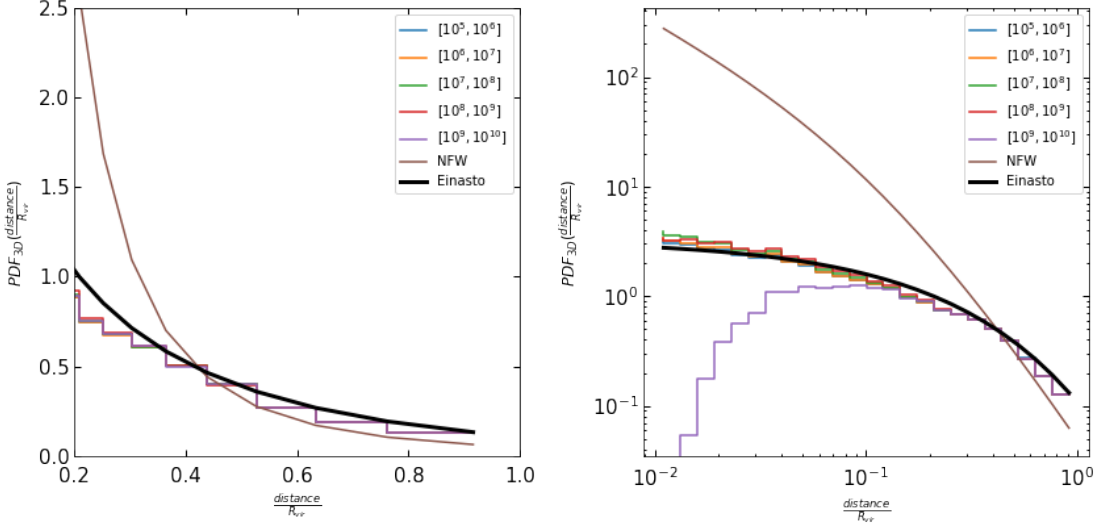
Figure 41: Subhaloes number density: new model.



In the plot above the agreement between the model's spatial results and the wanted Einasto profile is easily observed. Additionally, the spatial distribution of subhaloes with different masses has to be the same in terms of function's profile so no mass segregation is taking place. This can be done through the PDF_{3D} quantity for different subhalo's mass bins, this quantity represents the normalized number density of subhaloes.

$$PDF_{3D}(q) = \frac{PDF_{1D}(q)}{4\pi q^2}, PDF_{1D}(q) = \frac{dN_{sh}}{dq}, q = \frac{distance}{R_{vir}} \quad (4.1.2)$$

Figure 42: Subhaloes number density for different subhalo mass: new model.



Subhaloes' normalized number density of the new model for different subhalo mass bins.

No mass segregation is observed for subhaloes with mass lower than 10^9 solar masses and all subhalos follow the same density profile with great agreement to Einasto profile.

Regarding the mass function and the substructure's mass fraction it can be observed that is higher from the initial model's results. This is expected since the spatial distribution of this new model is biased to outer host's area in contrast to the NFW profile and in that area subhalos suffer less tidal stripping. This difference is an increase on the accuracy of the initial model's results on mass of subhaloes' values and statistics.

Figure 43: Subhaloes mass function: new model.

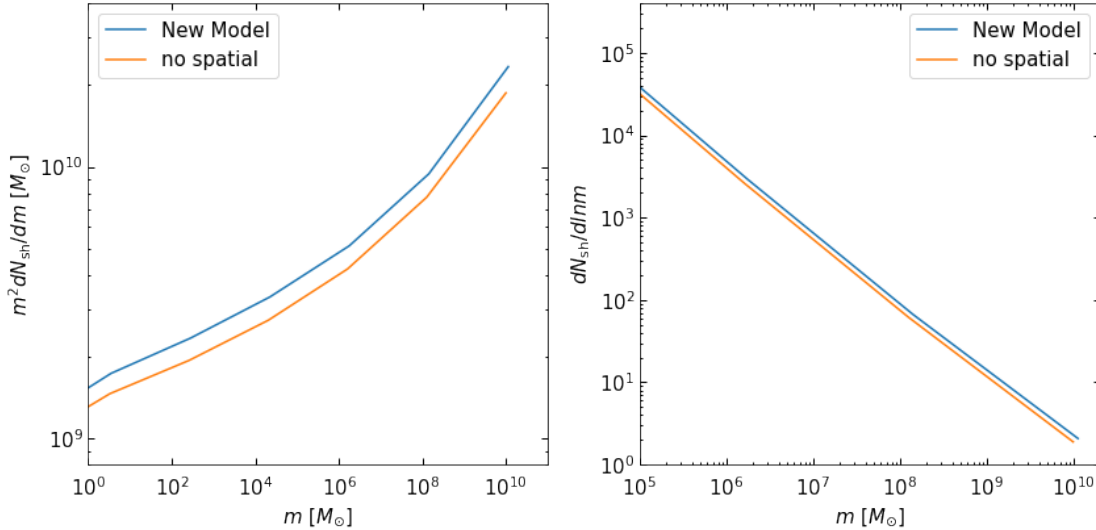
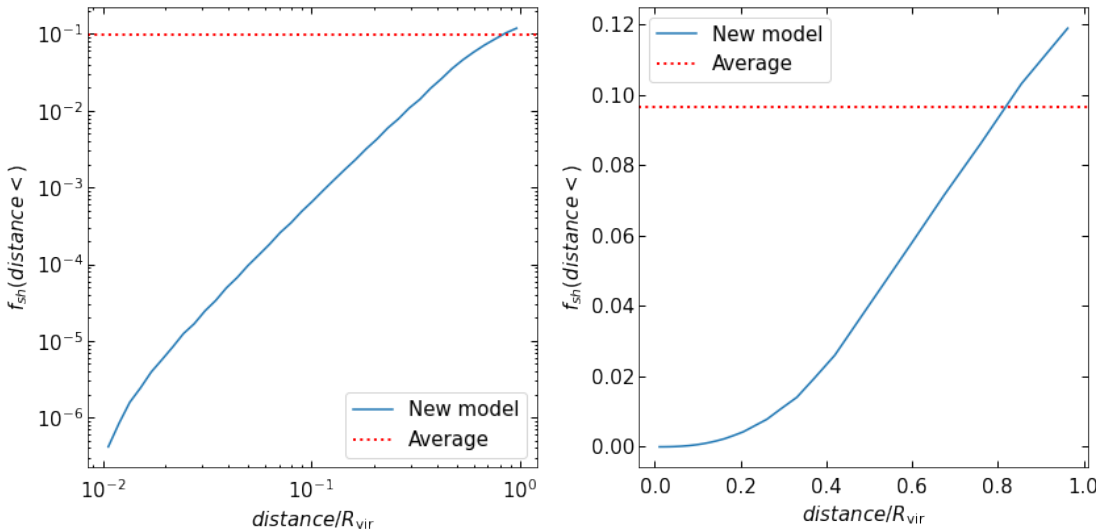
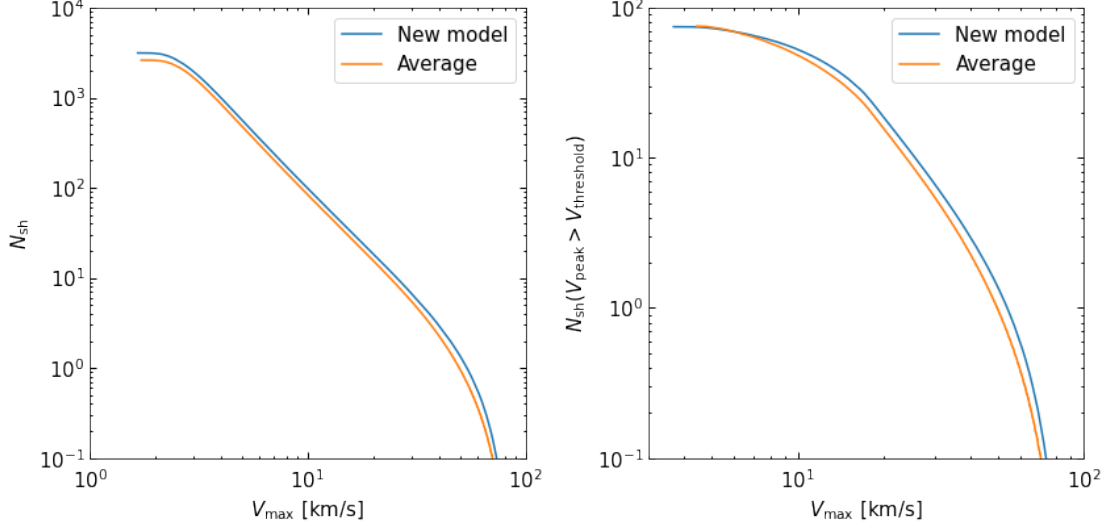


Figure 44: Subhaloes mass fraction: new model.



The satellite galaxies under the same formation conditions as before are shown also for the new model case.

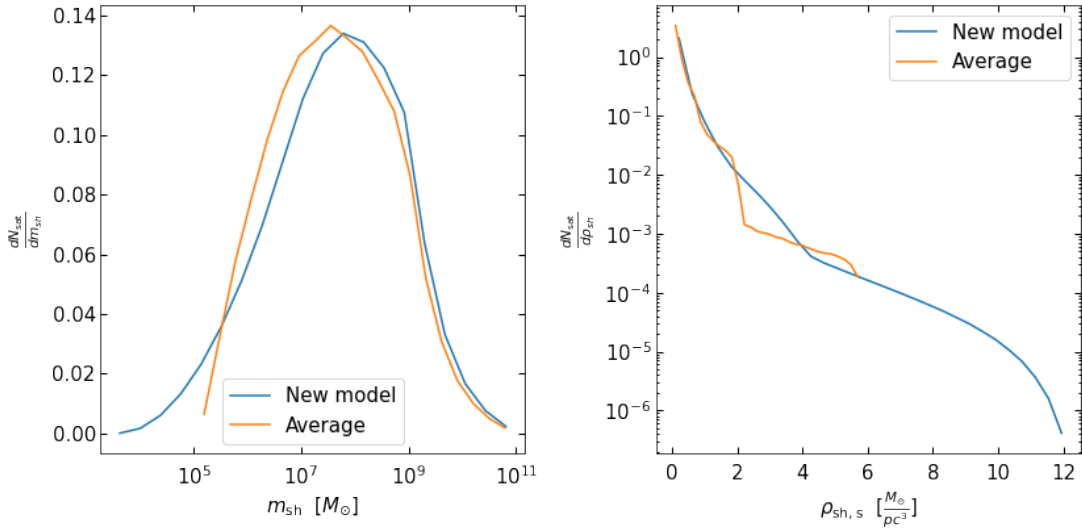
Figure 45: *Satellite galaxies: new model.*



The number of satellite galaxies do not differ from the number of the initial's model importantly, the initial model predicts 81-82 while the new model 83. Ideally due to the missing satellites problem on cold dark matter physics a decrease of satellite galaxies would be preferable but this is not observed, this can be explained from the substructure mass difference between the two models.

Further comparison of satellites galaxies of the initial model and new model can be done on their density and mass values.

Figure 46: *Satellite galaxies mass and density.*



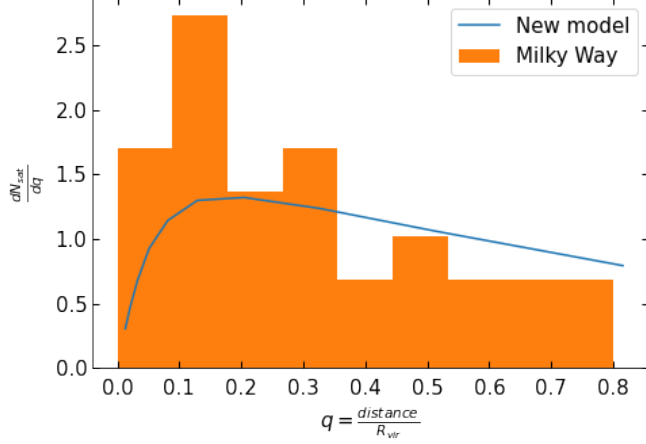
Satellite galaxies mass (left) and density (right) probability function for the new model and the initial model.

The satellite galaxies of the new model have similar density and mass probability functions. The only important difference can be observed in the satellite galaxy's minimum mass, the new

model leads to one order of magnitude smaller satellite galaxy mass values.

By the new model the radial probability density of satellite galaxies can be found.

Figure 47: *Satellite galaxies positions.*



Satellite galaxies radial probability function of new model and Milky Way's satellite galaxies [57].

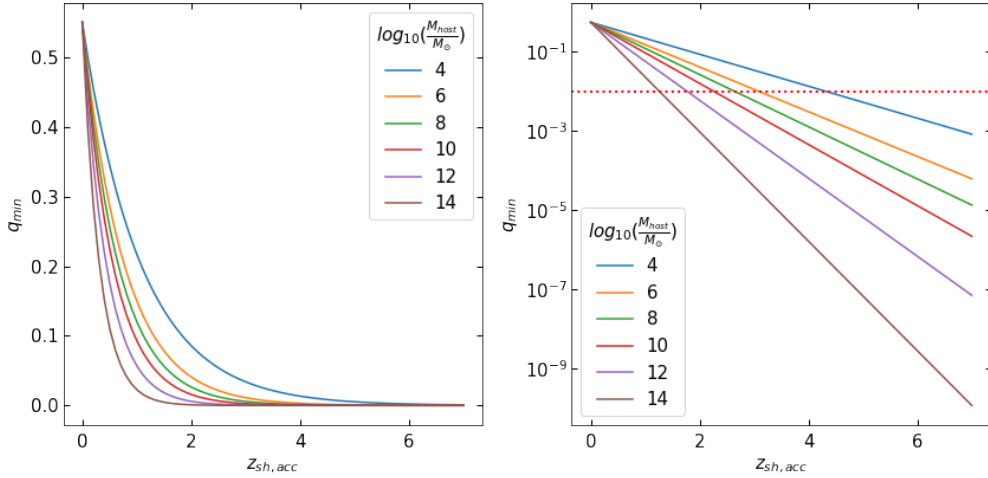
Although this additional condition works for host haloes similar to Milky Way, this relation for q_{min} has to be generalized for a wide host's mass range $[10^4, 10^{15}]$ solar masses and for host's redshift range $[0, 5]$:

$$q_{min}(z_{acc}, M_{host}) = 0.55 \cdot e^{-f(M_{host}) \cdot (z_{acc} - z_0)} \quad (4.1.3)$$

$$f(M_{host}) = 0.023 \cdot \log_{10}^2\left(\frac{M_{host}}{M_\odot}\right) - 0.256 \cdot \log_{10}\left(\frac{M_{host}}{M_\odot}\right) + 1.941 \quad (4.1.4)$$

where M_{host} is the host's mass at final redshift value z_0 .

Figure 48: *General condition of the new model.*



Minimum position of subhaloes through the additional spatial condition of the new model for different host mass values in linear (left) and logarithmic scale (right). The red dotted line is the distance value of 0.01 host's virial radius distance, which is the lowest considered distance value of subhaloes position.

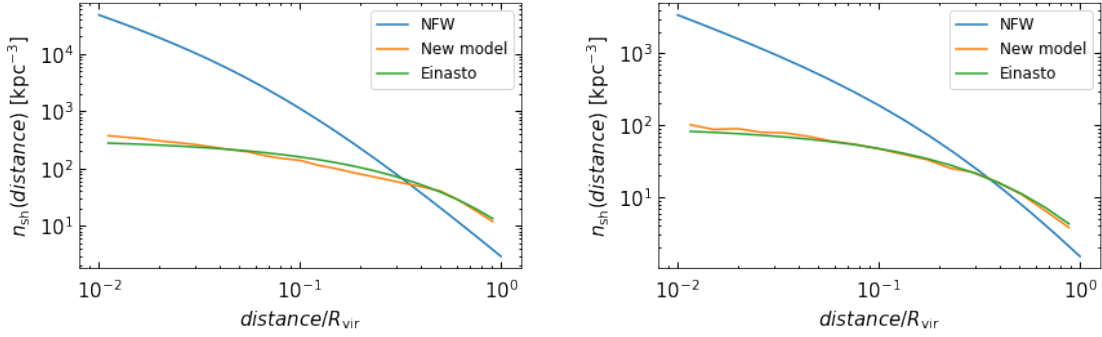
The q_{min} relation can be expressed also in host's virial radius R_{vir} as:

$$f(R_{vir}) = 0.185 \cdot \log_{10}^2(R_{vir}) - 0.02 \cdot \log_{10}(R_{vir}) + 1.168, R_{vir} \text{ in [kpc]} \quad (4.1.5)$$

The generalized q_{min} relation implies that subhaloes are moving towards to host's center faster in more massive hosts, which could be the result of the lower concentration and the higher gravitational pulling of more massive hosts. Additionally, a relation such this is also correlated with the dynamical friction of hosts but also with the mass of subhaloes, with more massive hosts to be accreting more massive subhaloes.

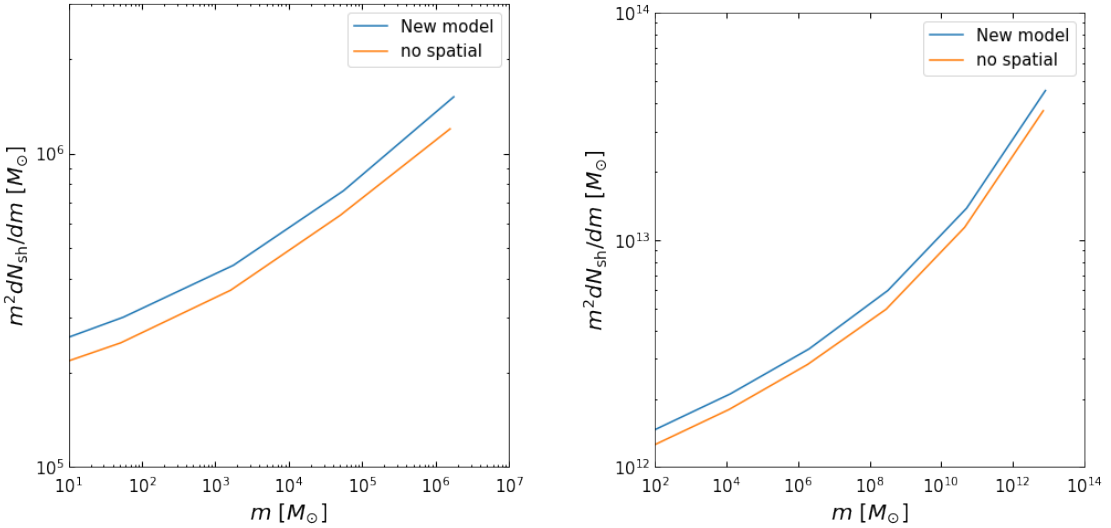
The new model after the generalized q_{min} relation can be applied to arbitrary host mass values. Below the results of a dark matter host halo with low and high mass are presented, 10^8 and 10^{15} solar masses respectively, regarding their number density and mass function. The subhalo number density is close to the Einasto profile for both cases, the new model is more accurate for high mass values of a host halo. The same effect of higher mass function of the new model in comparison with the initial model can be also observed here, with the difference to not be significantly large.

Figure 49: Subhaloes number density for different host mass values.



Subhaloes number density of the new model for host's mass values of 10^8 (left) and 10^{15} solar masses (right) at $z=0$.

Figure 50: Subhaloes mass function for different host's mass values.



Subhaloes mass function of the new model and initial model for host mass values of 10^8 (left) and 10^{15} solar masses (right) at $z=0$.

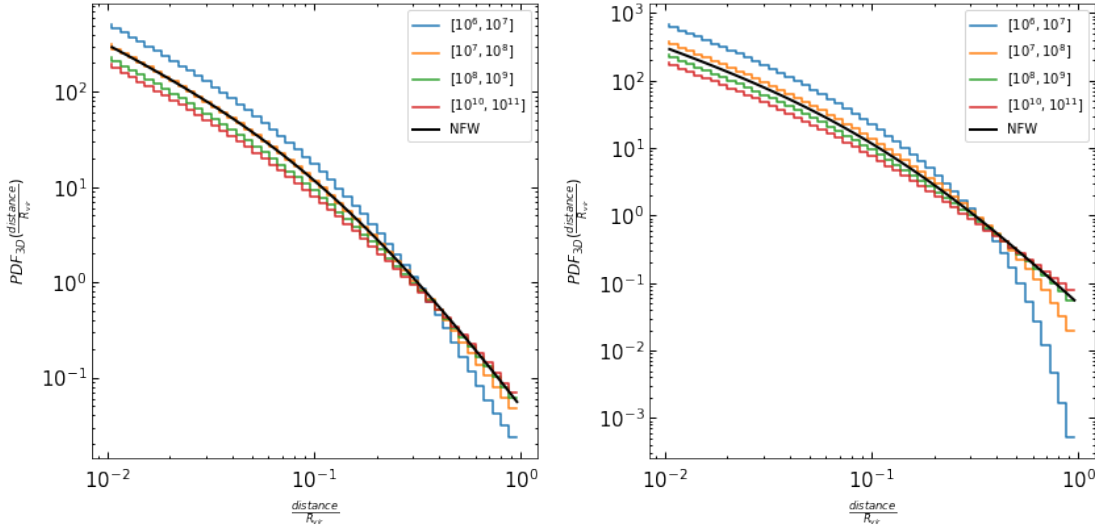
4.2 Warm Dark Matter Case

4.2.1 Model with basic assumptions

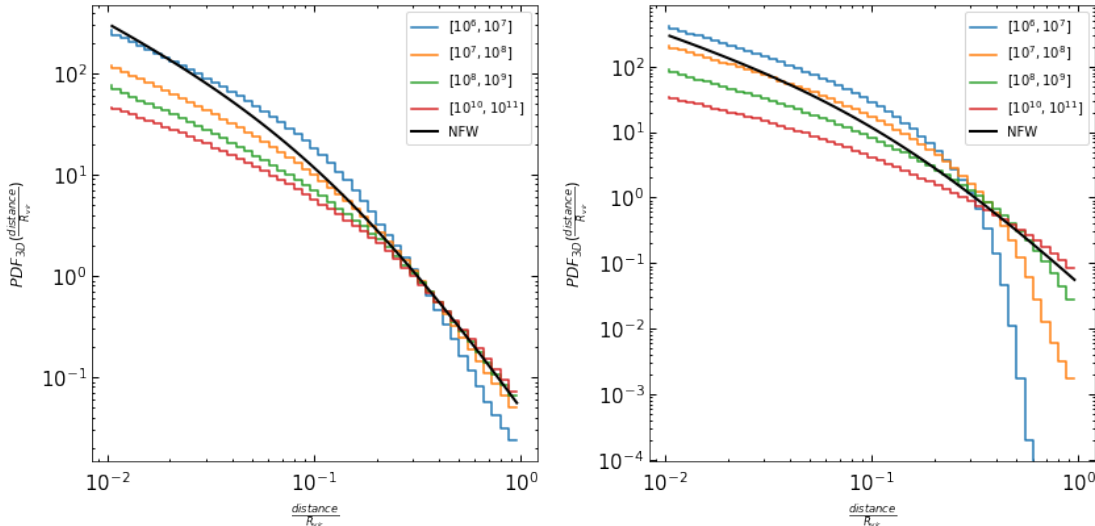
The same model used in the cold dark matter as previously discussed, applied also to warm dark matter particles with the respected main model to be same as [58]. The spatial relation of the tidal force from the host and the spatial distribution of subhalos are assumed to be the same as the CDM case, while the accretion rate is different following the appropriate power spectrum. For the WDM case the mass of the dark matter particle had to be chosen and the interesting values, especially considering recent X-ray observations, are in the range of a few keV and especially 1.5 keV and 3 keV. Below the spatial distribution of a warm dark matter particle with mass $m_{WDM} = 1.5\text{keV}$ are presented.

Figure 51: Warm dark matter subhaloes number density for $m_{WDM} = 1.5\text{keV}$

(a) Subhaloes' number density for the case of warm dark matter, for the mass loss models 2 (left) and 3 (right) with $M_{host} = 10^{12}M_\odot$ at $z=0$.



(b) Subhaloes' number density for the case of warm dark matter, for the mass loss models toy (left) and 4 (right) cases with $M_{host} = 10^{12}M_\odot$ at $z=0$.

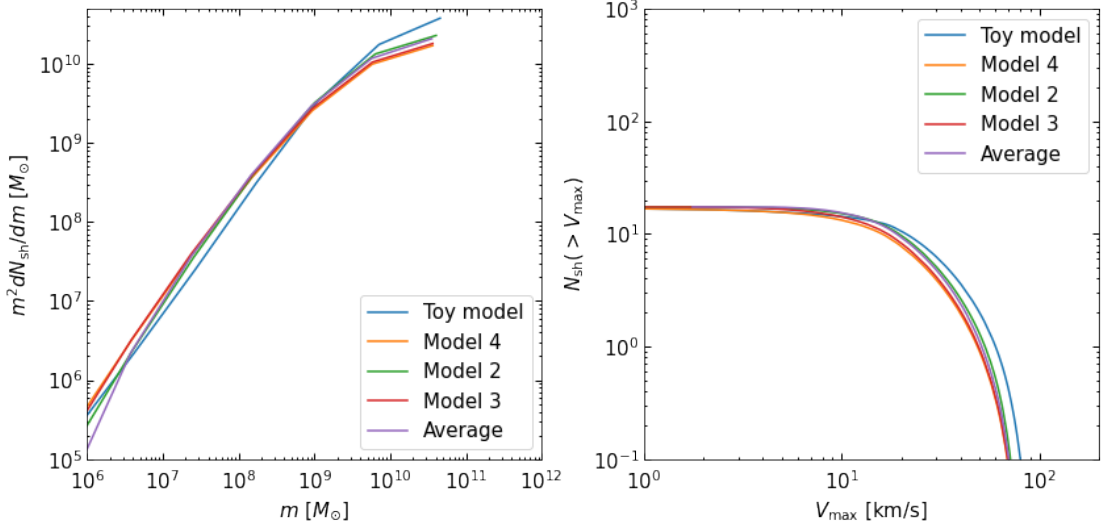


It can be seen that mass segregation is taking place in the WDM case. This is caused by

the expected Yang weights of warm dark matter, which follow different profiles as functions for different subhalo mass values. The free streaming effects are also a part of the cause for the mass segregation effects by the top to bottom structure formation, the host's spatial area where the tidal forces are higher the higher number density of low mass subhalos is expected. The mass loss model 2 leads to subhalos spatial distribution close to the NFW profile, while model 3 follows the same behavior as the NFW in the inner host's area, while the low mass subhalos are much less (or even not present) at the outer area of the host. The toy mass loss model shows substructure's subtraction at the inner area of the host and close to the NFW profile results at the outer area. The model 4 shows the same behavior as the toy model at the inner area and as model 3 at the outer area of the host halo.

Similarly to the CDM case, the mass function and the number of satellite galaxies are shown for the WDM case in 52. The number of galaxies does not change by using different mass loss model, while the difference of the mass function for different mass loss models from the initial model results have the same behavior as the CDM case. The mass function of warm dark matter particles is highly different from the CDM case, as subhalo mass value is decreasing from its maximum the number of subhalos is decreasing rapidly in comparison to CDM. This result is expected due to the free streaming effect imposing a minimum mass for accreted subhalos, for the given value of WDM particle the minimum mass of accreted subhalos is close (and higher) to 10^7 solar masses. For heavier particles this minimum mass value is getting lower, and so the number of subhalos (especially with lower masses) is increased and similarly increasing the total number of subhalos. As the m_{WDM} value is reaching masses higher than 100 keV the dark matter is getting to the cold dark matter regime, with masses at GeV and TeV ranges to be the most common CDM masses, the results of the WDM model used is leading to results close to the presented CDM case.

Figure 52: Warm dark matter subhaloes mass function and satellite galaxies for $m_{WDM} = 1.5 \text{keV}$



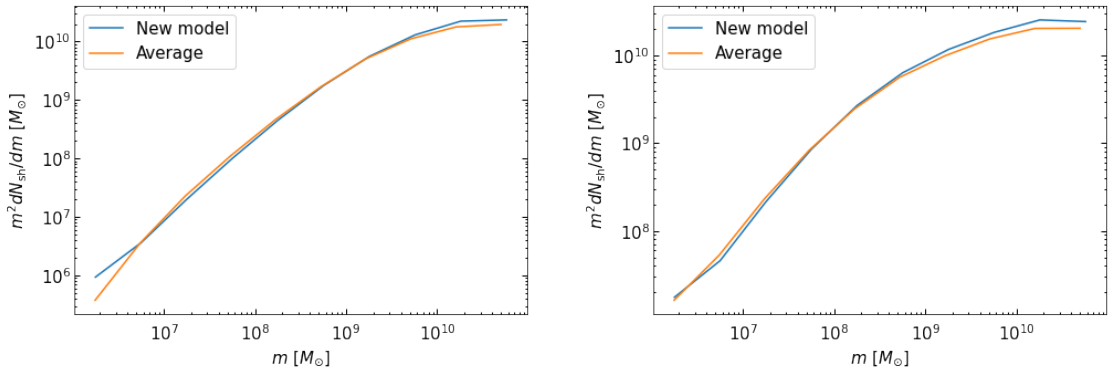
Mass function (left) and satellites galaxies (right) for the WDM case with $m_{WDM} = 1.5 \text{keV}$, for all the mass loss models with $M_{host} = 10^{12} M_\odot$ at $z=0$.

The substructure observed in the WDM case is extremely lower from the CDM case in terms of subhalos' number, but WDM subhalos although their low numbers have close total mass fraction to the CDM case, because WDM subhalos are very massive. The exact number of subhalos expected for this tested case is only 19! For the CDM case the same number is huge in comparison to 19, while this number depends on the used lower mass of a subhalo (lower minimum mass, much more subhalos). Assuming the lower CDM subhalo mass to be 10^{-6} solar masses the total number of subhalo are in the order of magnitude of 10^{15} , this is the greatest difference of CDM and WDM models regarding their small scale characteristics.

4.2.2 Model with additional information

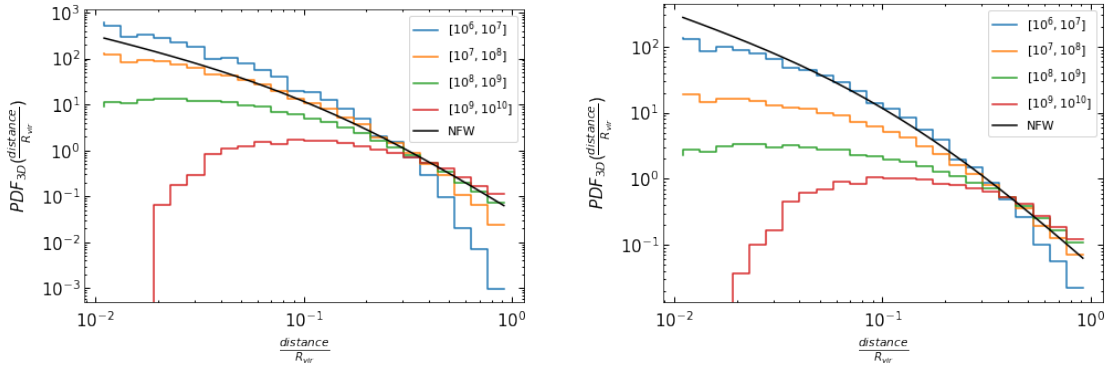
The base model assumptions used above may not break down for the case of WDM, mainly due to the very small number of subhalos inside the host not causing additional complex effects of subhalo-subhalo interactions. But since there are not many data from N-body simulations for WDM host halos and their results highly depend on the mass of the WDM particle, while the mass resolution in small masses range is limited, there is not enough certainty to know which approach of the two is a better fit or even which mass loss model is preferable in the previous section. The same approach of adding information in the model through the q_{min} term is applied additionally, since dynamically considering the gravitational effects of the host on each subhalo individually not many differences are expected from the CDM substructure. The same results as previously are presented for the case with the addition of the q_{min} relation for WDM particles with mass 1.5 keV and 3 keV.

Figure 53: *Warm dark matter subhaloes mass function : new model*



Subhaloes mass function for WDM particles with mass 1.5 keV (left) and 3 keV (right) using the new model, for a host halo with mass 10^{12} solar masses at $z=0$.

Figure 54: *Warm dark matter subhaloes number density : new model*



Subhaloes normalized number density for WDM particles with mass 1.5 keV (left) and 3 keV (right) using the new model, for a host halo with mass 10^{12} solar masses at $z=0$.

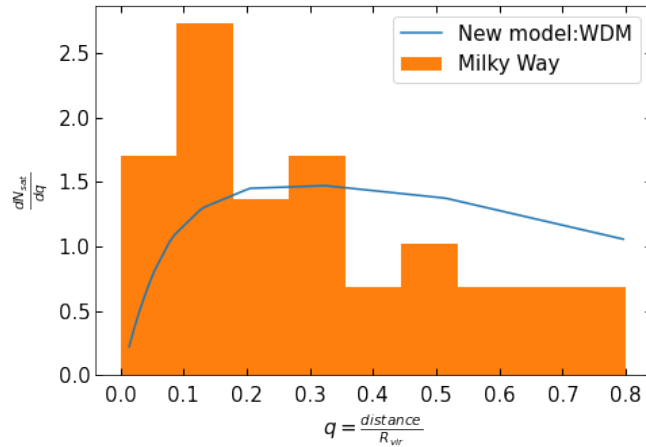
The mass function results of the new model for WDM are slightly higher than the initial model's results for both m_{WDM} values, with this difference to be expected due to the spatial bias of subhalos to outer area of the host in comparison to the NFW profile. Also, the increase of subhalos number at lower masses for higher m_{WDM} can be easily seen as expected. Regarding the spatial distribution results it can be observed that mass segregation still exist, with lower mass subhalos to be concentrated to lower distances from the host's center and higher subhalos to higher

distances. The more massive subhalos have number density which tend to a plateau in the core of the host, while at the outer area are similar to NFW profile. As the mass of the WDM particle is increasing the normalized density values close to the core are subtracted and the low mass subhalos values at the outer area is increased. For extremely high m_{WDM} values at GeV or TeV range, and so working at the cold dark matter mass range, the results are the same as the CDM new model results as expected.

Regarding the satellite galaxies number, again the initial model and the new model did not appear to have high differences for both m_{WDM} values. As expected, the total subhalos increased for the case of the $m_{WDM} = 3$ keV from 19 to 86, with the number of formed satellite galaxies to change from 17 to 45 respectively. The total mass fraction of subhalos similarly is slightly higher than the initial's model's results for the new model as in the CDM case, while by the increase of m_{WDM} the total mass fraction is increasing tending to reach the CDM value for m_{WDM} tending to CDM particle mass range.

For the case of satellite galaxies spatial distribution, the case of $m_{wdm} = 3$ keV used but there is not difference from the $m_{wdm} = 1.5$ keV case.

Figure 55: *Satellite galaxies positions : WDM*



Satellite galaxies radial probability function for warm dark matter particle with mass 3 keV, for a host with 10^{12} solar masses at $z=0$ and Milky Way's satellite galaxies [57].

It can be seen that the WDM model satellite galaxies spatial distribution has less agreement with the Milky Way's respected observations than the CDM case. The WDM satellite galaxies are predicted at higher distances than the CDM case and the observations, with the probability of satellites at the outer area of the host to be increased but also to not showing high differences as distance changes at that area.

4.3 Annihilation boost factor

Dark matter particle such as WIMPs are self interacting particles [59]. Theoretically, when two dark matter particles collide with each other, they “annihilate” and turn into quark, lepton and other particles of the standard model. These unstable particles will decay and turn into more stable particles, such as positrons and electrons, protons and antiprotons, neutrinos, and photons, etc. For this section the gamma ray annihilation is the part of interest, since this annihilation channel is better understood and could lead to indirect detection of dark matter from large cosmic objects such as galactic halos.

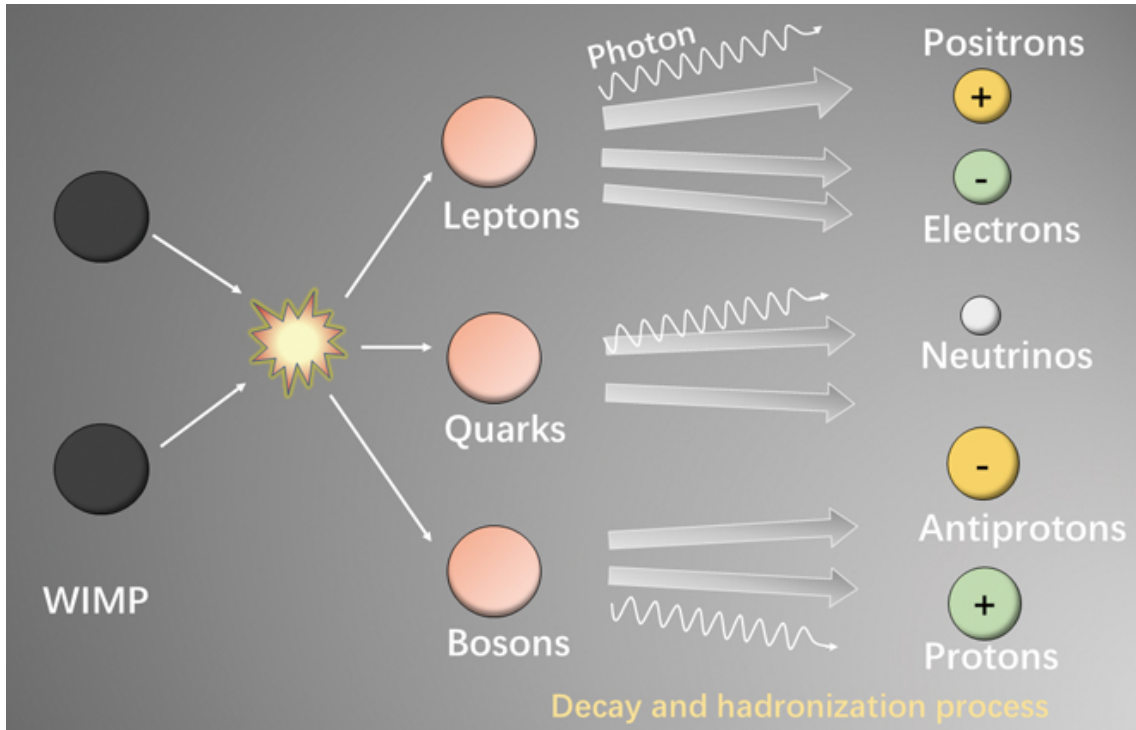


Figure 56: Principle of indirect detection of dark matter. (Image by GAO Linqing and LIN Sujie)

One of the goals of this project is to provide the gamma ray signal from dark matter subhalos, since the respected signal of a host halo with density profile as the NFW profile has been calculated. For the case of smooth subhalos the gamma-ray luminosity from dark matter annihilation in the smooth NFW component of the host halo with mass M and redshift z can be calculated through the formula [42]:

$$L_{host}(M) \sim dc_{vir} P(c_{vir}|M, z) \cdot \rho_s^2 r_s^3 \left(1 - \frac{1}{(1 + c_{vir})^3}\right) \quad (4.3.1)$$

where $P(c_{vir}|M, z)$ is again the log-normal distribution of the host’s concentration parameter given M and z , and the scale radius r_s and the characteristic density ρ_s are both dependent on c_{vir} as well as on M and z . The constant of proportionality of this relation includes particle physics parameters such as the mass and annihilation cross section of dark matter particles, but since here we are interested in the ratio of the luminosity between the subhaloes and the host, their dependence cancels out. The subhaloes’ boost factor quantifies the contribution of all the subhaloes to the total annihilation gamma-ray signal compared with the contribution of the host. It is defined as

$$B_{sh}(M) = \frac{L_{sh}^{total}(M)}{L_{host}(M)} \quad (4.3.2)$$

such that the total luminosity from the halo is given as $L_{total} = (1 + B_{sh}) \cdot L_{host}$. The luminosity from a single subhalo i characterized with its accretion mass $m_{acc,i}$ and redshift $z_{acc,i}$, as well as its virial concentration $c_{vir,acc}$ is

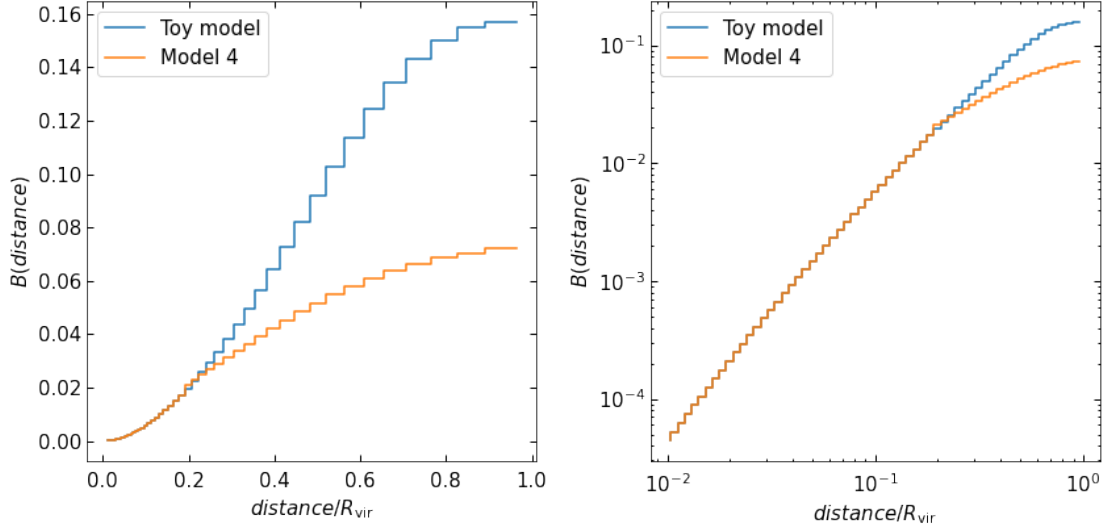
$$L_{sh,i} \sim \rho_{s,i} r_{s,i}^3 \left(1 - \frac{1}{(1 + r_{t,i}/r_{s,i})^3} \right) \quad (4.3.3)$$

where $r_{s,i}$, $r_{t,i}$, and $\rho_{s,i}$ are the scale radius, truncation radius, and characteristic density of the subhalo i after it experienced the tidal mass loss, and hence they are functions of $m_{acc,i}$, $z_{acc,i}$, and $c_{vir,acc}$ as well as the mass of the host M and redshift z. The total subhalo luminosity $L_{sh}^{total}(M)$ is then obtained as the sum of $L_{sh,i}$ with weight w_i and averaged over $c_{vir,acc}$ with its distribution:

$$L_{sh}^{total}(M) = \sum_i w_i d c_{vir,acc} P(c_{vir,acc} | m_{acc,i}, z_{acc,i}) L_{sh,i}(z | c_{vir,acc}) \Theta[r_{t,i}(z | c_{vir,acc}) - 0.77 r_{s,i}(z | c_{vir,acc})] \quad (4.3.4)$$

From the results of the model which was presented in the previous sections the substructure's boost factor at different areas of the host halo can be calculated. For only the basic model's assumptions, the most efficient mass loss models (without any additional information) are the toy and 4 case and so their results are presented.

Figure 57: Boost factor at different distance : first results.



Boost factor at different distance from the halo's center in units of host halo's virial radius for model 4 and toy model cases.

The total boost factor for the initial model is 1.38, while for the toy model and model 4 cases is 2.21 and 1.13 respectively showing that the boost factor is proportional to substructure's mass fraction. The Boost factor near the host center has the same behavior for the two models and the relation between the boost factor and the distance from host's center is a power law relation, while for large distances a polynomial relation seem to be more efficient. The next step is to fit the boost factor results based on the power law assumption for small distances and polynomial for large distances. The best fitting results are presented below:

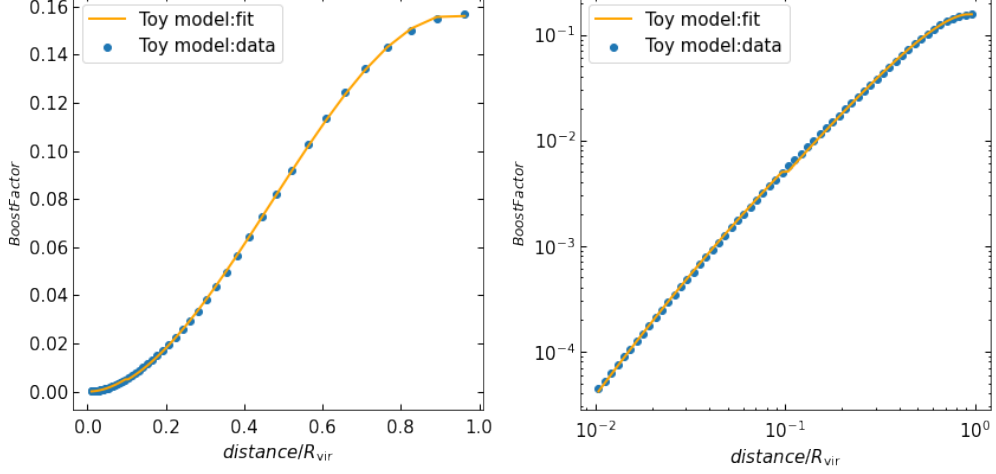
$$B_{toy}(q) = \begin{cases} 10^{-0.28 \cdot \log_{10}(q) + 1.31 \cdot \log_{10}(q) - 0.68} & q \leq 0.1 \\ -0.39 \cdot q^3 + 0.548 \cdot q^2 - 0.004 \cdot q & q \geq 0.1 \end{cases}, q = \frac{\text{distance}}{R_{vir}} \quad (4.3.5)$$

$$B_4(q) = \begin{cases} 10^{-0.28 \cdot \log_{10}(q) + 1.31 \cdot \log_{10}(q) - 0.68} & q \leq 0.2 \\ -0.069 \cdot q^2 + 0.149 \cdot q - 0.008 & q \geq 0.2 \end{cases}, q = \frac{\text{distance}}{R_{vir}} \quad (4.3.6)$$

$$B_{4,alt}(q) = 10^{-0.25 \cdot \log_{10}^3(q) - 1.25 \cdot \log_{10}^2(q) + 0.11 \cdot \log_{10}(q) - 1.15}, q = \frac{\text{distance}}{R_{vir}} \quad (4.3.7)$$

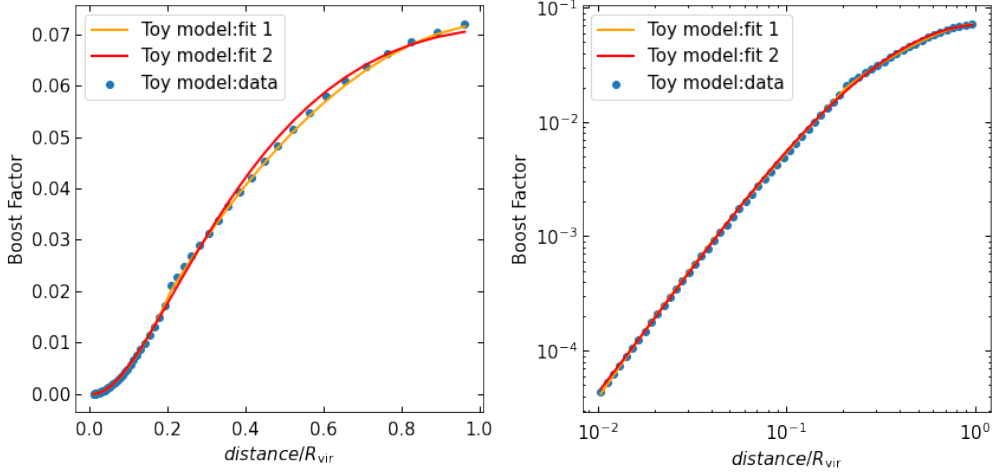
For the process of fitting for large distances a polynomial function was used while for small distances a power law.

Figure 58: Boost factor fitting: toy model.



Fitting of the boost factor for the case of the toy mass loss model.

Boost factor fitting: model 4 case.



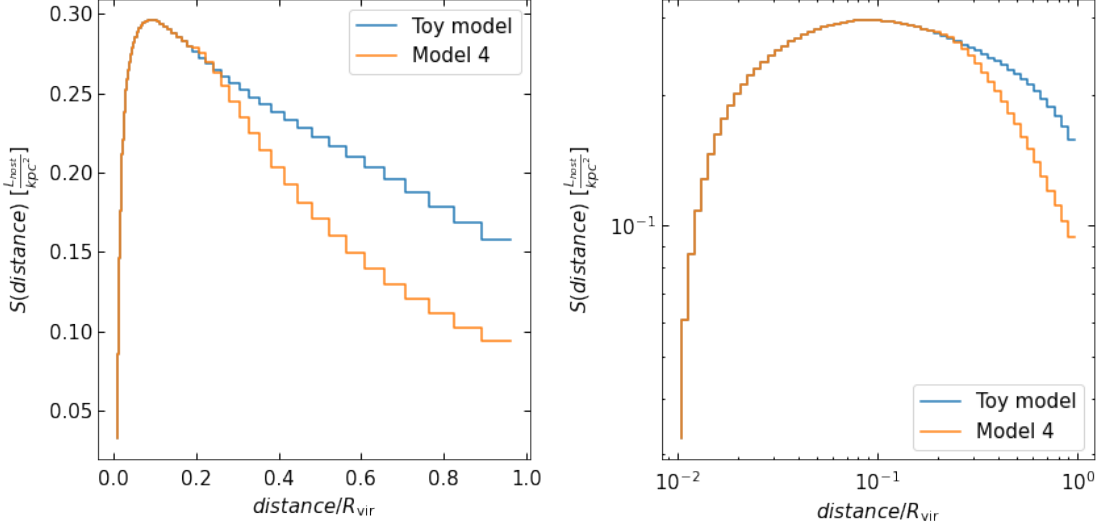
Fitting of the boost factor for the case of the mass loss model 4.

The fitting functions are very close to the data accurately while they are continuous functions. For the case of model 4 mass loss function there two fitting function with one being the combination of a power law and a polynomial to be more accurate but a power law function could lead to close results but with less accuracy from the other fitting.

An additional result which can be extracted from the boost factor spatial formula is the substructure's surface brightness, since it is equal to the total subhalos' gamma ray emission at a distance divided by this distance's spherical area.

$$S_i(q) = \frac{B_i(q <)}{4\pi q^2}, q = \frac{\text{distance}}{R_{vir}}, i = \text{toy, 4} \quad (4.3.8)$$

Figure 59: Surface brightness : first results.

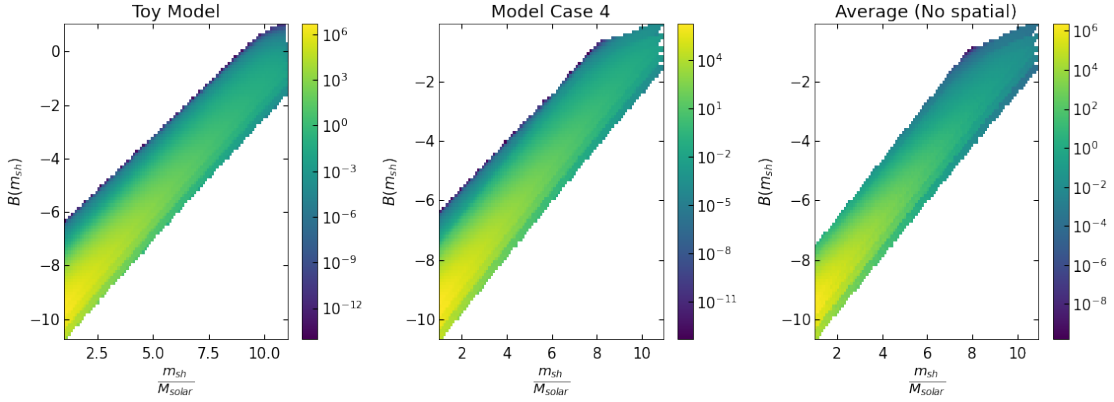


Surface brightness at different distance from the halo's center in units of host halo's virial radius for model 4 and toy model cases.

4.3.1 Dark matter substructure's gamma-ray emission

A very useful application of the previously calculated boost factor is the creation of mock signals for dark matter halos' substructure for the field of indirect searches of dark matter. The ideal case would be to create a Monte Carlo catalogue with all the subhalos according to the model's results, but this is computationally not efficient due to the huge number of small mass subhalos. The other way would be the creation of a template based on the weights of the subhalos which was calculated from the model with the assumption of spherical symmetry for the host.

Figure 60: Boost factor-mass correlation.

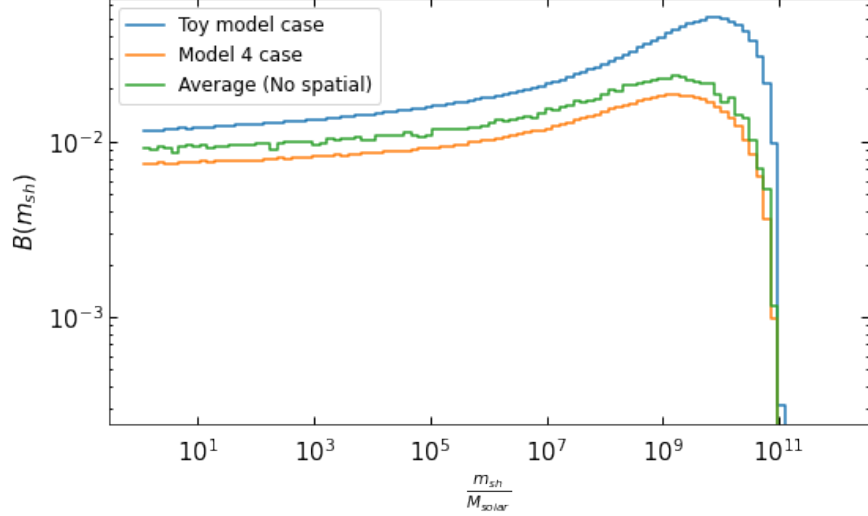


Boost factor and mass correlation for different subhalo masses for the cases of toy model, model 4 and the model without spatial information.

Based on the mass-boost factor plots it is obvious that a power law behavior exist for all mass loss models with the more massive subhalos to have significantly higher gamma ray emission. But the number of subhalos to be much lower as their mass increases, so the contribution to the total substructure's boost factor of each mass bin of substructure has to be taken into consideration.

The low mass subhaloes' bins have almost equal contribution to the total boost factor with

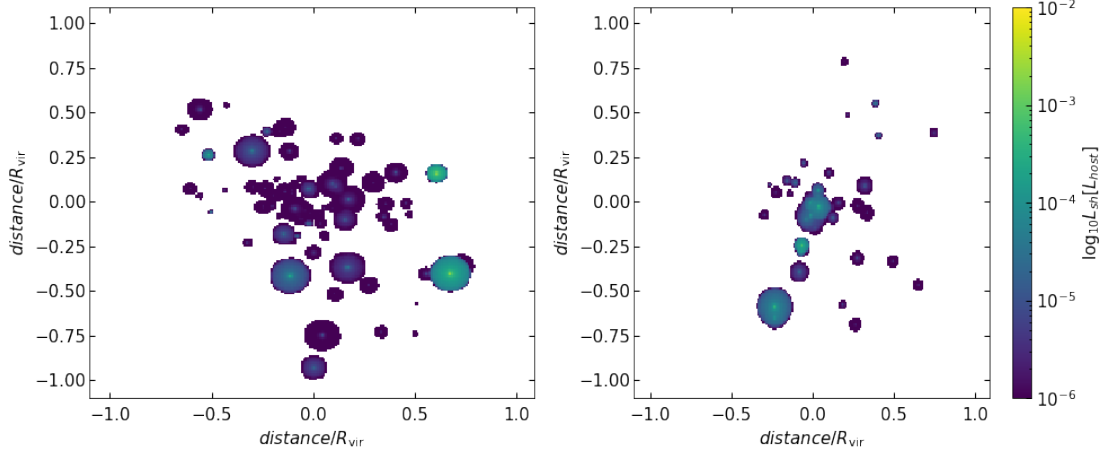
Figure 61: Subhalo mass boost factor relation.



Subhalo mass bin contribution to the total annihilation boost factor of a host.

their number to be extremely high. So for low mass subhaloes a spherically symmetric template can be used in which the distinct spatial characteristics of subhaloes are not taken into account. The high mass subhaloes, with mass higher than $10^7 - 10^8$, are few and so realistically they appear as distinct spherical structures.

Figure 62: Simulated subhaloes luminosity.



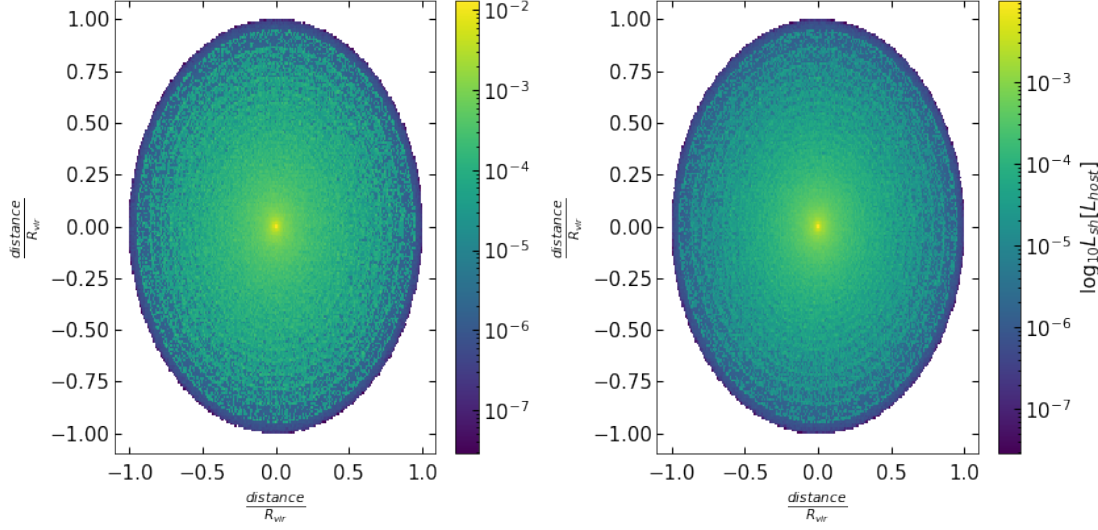
Subhaloes' Monte Carlo mock catalogues based on the results of toy model (left) and model 4 (right) with mass higher than $5 \cdot 10^7$, with the subhaloes' luminosity to be presented.

The simulated subhaloes of the toy model have higher number than the toy model's ones, while they also have higher luminosity values. But from their luminosity values a few of them are expected to be visible from the total luminosity of all the host's substructure emission.

For the subhaloes with low masses, smaller or equal to $5 \cdot 10^7$, the boost factor values at a given distance are divided spatially to a large number of angular values $(\theta, \phi) \in ([-\pi/2, \pi/2], [0, 2\pi])$ which are projected to a two dimensional plane. This 2D plane is vertical to an axis parallel to the line of sight of the host halo. This assumption of course is based on the perfect spherical symmetry

of the host and the large distance between the host and the observer.

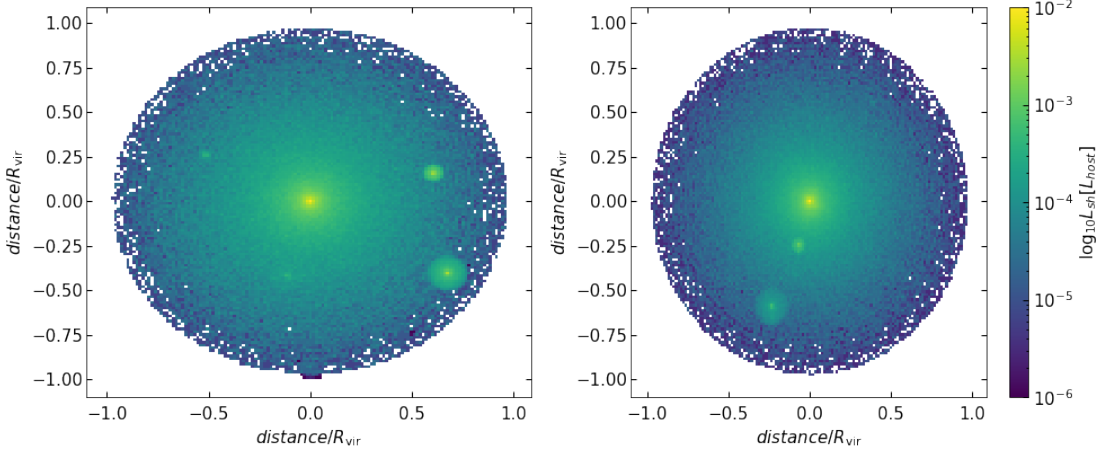
Figure 63: Low mass subhaloes luminosity.



Subhaloes' luminosity template for the toy model (left) and the model 4 (right) cases for subhaloes with mass smaller than $5 \cdot 10^7$.

The luminosity template above can be added to the simulated high mass subhaloes luminosity leading to the total substructure's luminosity in units of host's luminosity.

Figure 64: Total luminosity template : Toy and 4 mass models.



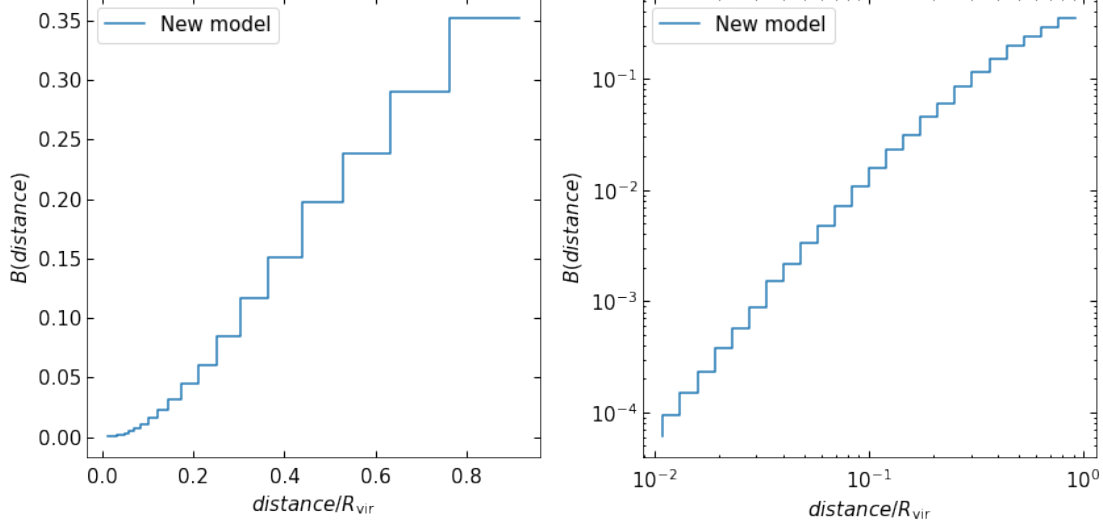
Subhaloes' luminosity template for the toy model (left) and the model 4 (right) cases.

It is observed that a very small number of subhalos can be seen clearly as a different part from the total substructure's luminosity, with the further from the host's center for a subhalo to be the more easier to be visible.

4.3.2 Model with additional information

The same process of the previous section was completed also for the model with the additional information. These results are the most accurate results of this project regarding the resulting spatial distribution of subhalos to be the wanted Einasto profile.

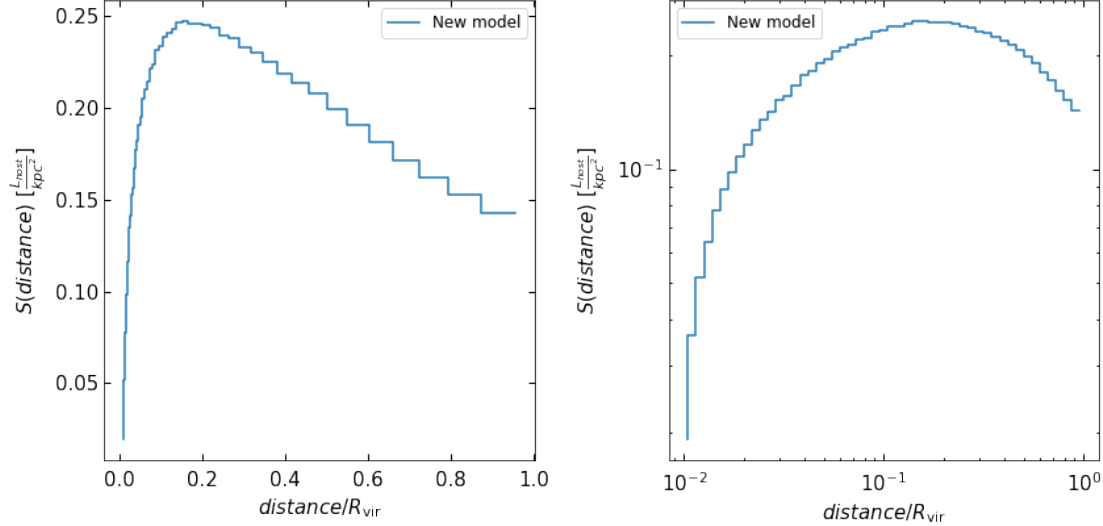
Figure 65: Boost factor at different distances : new model



The total substructure's boost factor value is 1,64 with the initial model's to be 1,38. This increase of the boost factor is expected due to the mass fraction increase in the new model. The boost factor distance function do not differ importantly from the cases of the toy model and model 4 mass loss cases as a function profile and so a similar fitting function was applied:

$$B(q) = 10^{-0.13 \cdot \log_{10}^3(q) - 0.79 \cdot \log_{10}^2(q) + 0.9 \cdot \log_{10}(q) - 0.41}, q = \frac{\text{distance}}{R_{vir}} \quad (4.3.9)$$

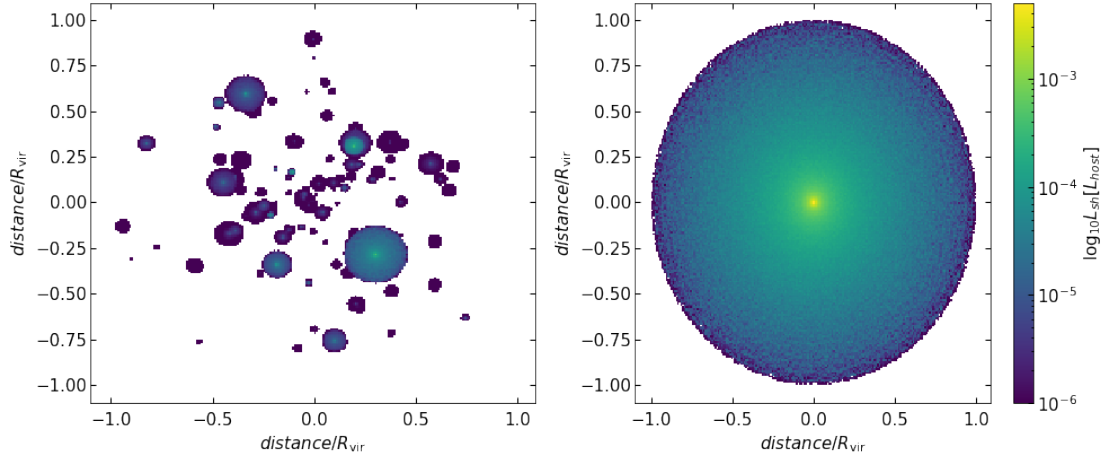
Figure 66: Surface Brightness : new model.



The surface brightness of the substructure is also shown and no important differences are

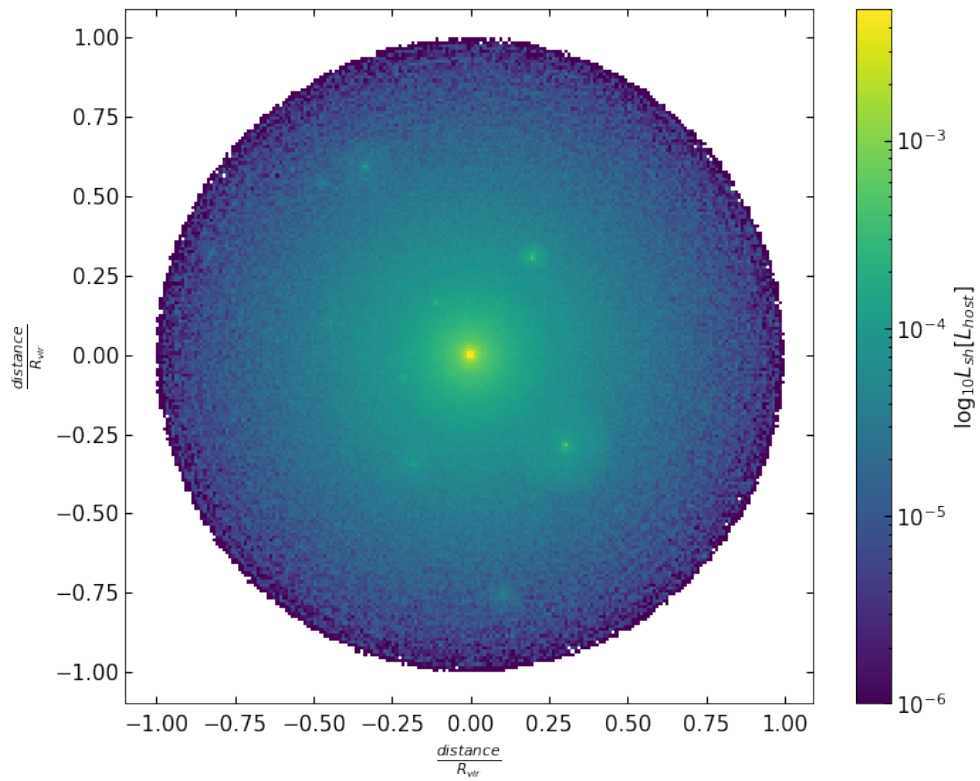
observed with the mass loss cases of toy and model 4. The luminosity templates with the same process as before are shown below.

Figure 67: Luminosity templates: new model.



Monte Carlo simulated subhaloes (left) with $m_{sh} > 5 \cdot 10^7$ solar masses and spherical uniform (right) luminosity template with $m_{sh} < 5 \cdot 10^7$ solar masses, for a host halo with mass $10^{12}[M_\odot]$ at $z=0$.

Figure 68: Total luminosity template: new model.



5. Discussion

From the results of the presented model it can be seen that there are still a lot of limitations of a simplistic model based on general physical assumptions. The final results looks promising but more study and physical information is needed for capturing more characteristics of a host's substructure.

The main assumptions only are not enough for capturing the spatial characteristics of the substructure. The mass loss rate models which resulted from N-body simulations needed more information in order to be sufficient, without the additional assumption the substructure follows a density function very close to the NFW profile and thus very far from the realistic cases. It was shown that the initial assumptions (without information of subhaloes' accretion positions) break down significantly for the mass loss models based on the N-body simulation, while the case of the toy mass loss model showed a slightly better subhaloes' number density result. Although the toy model (and model 4) could be manipulated to lead to a core number density profile for the subhaloes near the host's center, it is physically unreasonable since the early accreted subhalos are completely disrupted near the core and this is not compatible with simulations' results. Also, for this mass loss case the only subhaloes which survive near the host's core are the subhalos with very small accretion redshift ($z_{sh,acc} < 0.4$), which is not reasonable regarding the huge distance and the small number of completed orbits of these subhalos.

Regarding substructure's characteristics, the mass loss rates from the N-body simulation results lead to results in agreement with the initial model. This is expected and so these cases are preferable, the toy model case leads to subhaloes with higher mass and concentration due to the mass loss tending to 0 at distances close to the host's virial radius. The toy model mass loss (and similar relations) is not reasonable mass loss rate function. From the comparison of substructure's mass fraction the toy model shows completely unreasonable results, while the other models are close to the initial model's results. After the addition of more information in the model the substructure's mass fraction is increased. This result is expected by comparing the NFW density profile with the wanted Einasto profile. Subhaloes which follow the latter spatial distribution are relatively biased to higher distance values from the host's core area where the tidal stripping forces are smaller. This last difference is a key addition to the results of the initial model.

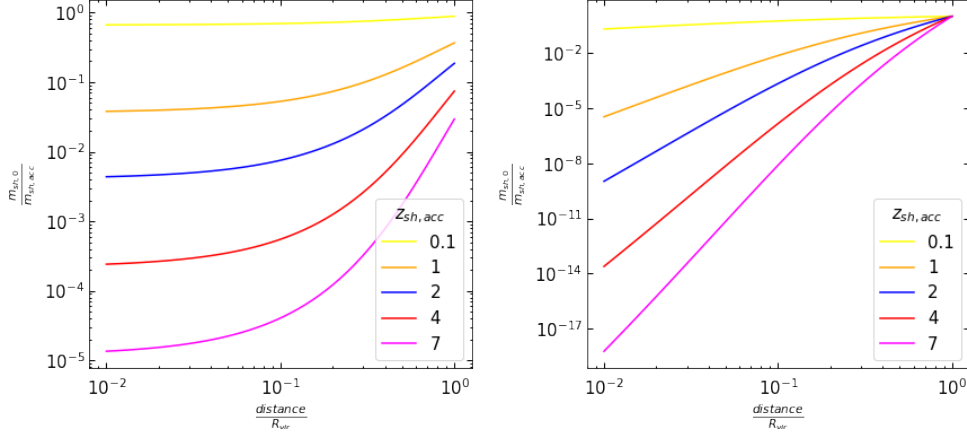
For the warm dark matter case results there is high uncertainty due to the lack of extensive studies. The main difference from the CDM case is the mass segregation effect, which is an effect of both the top to bottom structure formation and the respected accretion rate. It can be seen that the model with only the base assumptions leads to substructure spatial distribution near the core close to the NFW profile with a plateau behavior to be expected, while the mass function and satellite galaxies number differences from the initial model have the same effects as the CDM case. The low mass subhaloes seem to be biased to closer distances from the host's center and to be almost absent from the host's outer area. This can be easily explained from the structure formation of the WDM, at the area of higher mass loss more low mass subhaloes are expected. For the WDM model with the additional relation it can be seen that the subhaloes with high masses follows a spatial distribution with a similar to Einasto behavior. Also, the higher the mass of the WDM particle, the more suppressed is the substructure near the core, while the subhaloes number density at the outer area is increased. With increasing the WDM particle mass also the total substructure is increased, with the cut off mass due to free streaming to getting lower. These results of course need more work in order to be credible, the additional relation of q_{min} can be significantly different for the WDM case considering the much less substructure of the host.

Another important result of this model is one of the few works on the dark matter annihilation boost factor function with spatial dependency. This relation cannot safely tested since there is not a broad literature and it have to be tested in future with more studies. Through this relation mock gamma ray emission templates of dark matter halos can be produced, adding these templates with the respected galactic emission templates can lead to the large structures emission such as galaxies or galactic clusters with all their components. The more reliable boost factor results are for the case of the model with additional information (new model), but other important mass loss models results are presented. This application of the model can improve the indirect dark matter searches and test the ability of the new observational instruments and analysis methods, providing a strong tool for indirect dark matter searches.

5.1 Comparison with similar models

In previous work on dark matter halo's substructure modeling [60], [61] different approaches were used. In [60] the assumptions used led to the wanted Einasto profile, the main assumption for the mass loss was $\frac{m_{sh,0}}{m_{sh,acc}} \sim \text{distance}$. But an assumption like this one do not consider the accretion redshift effects on the mass loss, this effect can be shown for this project and clearly this is not the case.

Figure 69: Accretion redshift effects on mass loss.



The ratio of the subhaloes masses at $z=0$ to their mass at accretion, for different accretion redshift values, for the mass model 2 case (left) and toy model case (right) at 0.05 host's virial distance from the host's center.

In [61] an orbital decay function of subhaloes' circular orbit radius based on the Chandrasekhar formula is used, an approach which has high uncertainty due to the high complexity of the dynamical evolution of the substructure. Both of these models did not considered the evolution of all the substructure for a wide range of subhaloes' accretion redshift and mass values.

5.2 How to further improve this model

A better approach would be to include through simulations results the relation between the subhaloes accretion and "final" spatial distribution, especially for the later accreted subhaloes. Although the NFW profile for subhaloes' spatial distribution is expected in general as an assumption with limitations, while its range of credibility is better suited for subhalos which have completed several orbits and so reached a stable equilibrium orbit.

An important question is how this model can be improved, by changing the physical assumptions to more realistic cases or by including more information. The key sections which need improvements are:

- Mass loss rate with spatial dependency for different redshift and host halo mass values from N-body simulations.
- Subhaloes final spatial distribution for different subhalo accretion redshift.
- Test of the additional subhalo's spatial assumption of minimum distance related to accretion redshift.
- Host halo and subhaloes elliptical shapes.
- Subhaloes elliptical orbits.

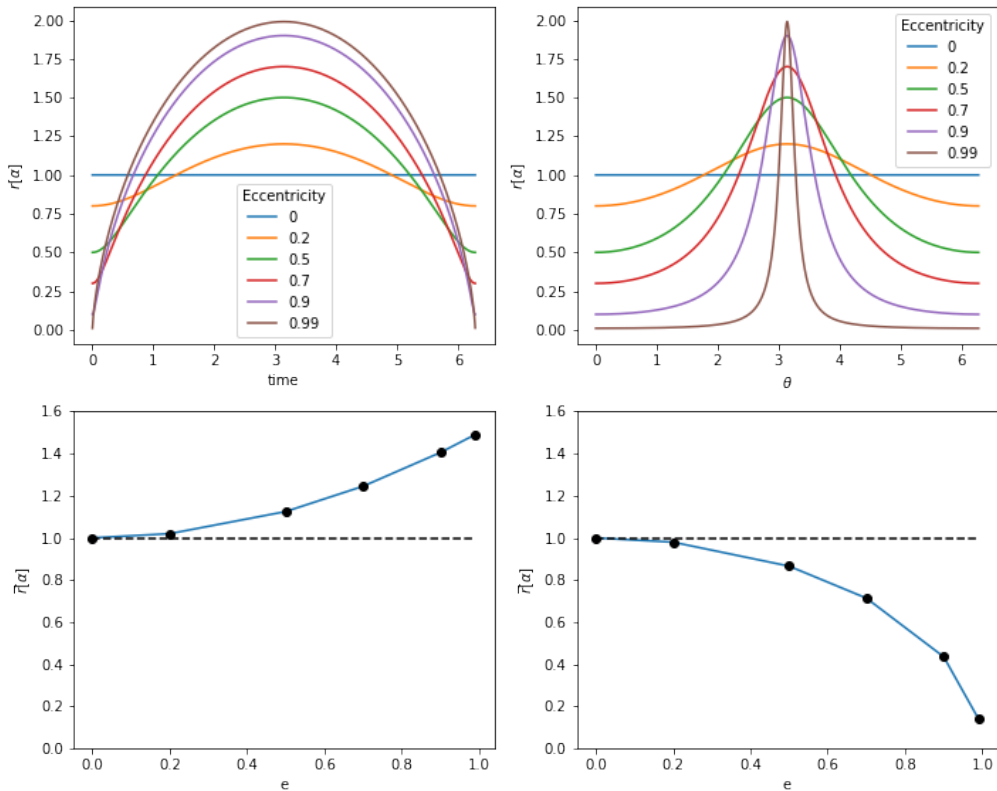
First of all, the mass loss rate formulas which are used in this project are based completely on the result of a host mass with one mass value at redshift 0. It would be important to test this relation for different host's mass values but also to test its dependence on redshift. Additionally,

the subhaloes' final spatial distribution could be different for different accretion redshift due to the difference on accretion positions and number of orbits. Results from N-body simulations could provide this information which seems to be crucial for the effectiveness of a substructure model. These results could also test the additional spatial assumption on subhaloes with different accretion redshift.

5.2.1 Haloes elliptical orbit effect

A big difference between the model of this project and the physical reality, is that for this model the subhaloes follows only circular orbits but this is far from true. The subhalos, as most of the astrophysical objects, tend to follow elliptical orbits with eccentricity in a wide range of values. Their eccentricity is depending on a variety of parameters which define a subhalo's dynamical evolution such as its energy, angular momentum and the gravitational interaction with the host's gravitational potential.

Figure 70: *Elliptical orbit effect.*



Orbits with different eccentricity (up), their radial values for different time and angle values during their trajectory (middle) and the mean position over time and angle for these different eccentricity values (down).

It is obvious that objects with elliptical orbits tend to "spend" more time at their apocenter and so it is more probable to observe them with an orbital radius value higher than its semi major axis, which can be assumed to be equal to the circular orbit defined in this model. The spatial distribution of subhalos extracted by N-body simulations measure the distance of subhalos form the host's center at a defined redshift value and so it is expected to be a bias to have higher orbital radius than the assumed circular orbital radius, this effect can be quantified by the mean radial position with time:

$$\bar{r}_{elliptical} = \alpha \cdot \left(1 + \frac{e}{2}\right) \quad (5.2.1)$$

where α is the semi major axis and e is the subhaloes eccentricity, for the latter information from works such as [62] can be used for increasing the accuracy of the model.

5.3 Additional used approaches on the problem

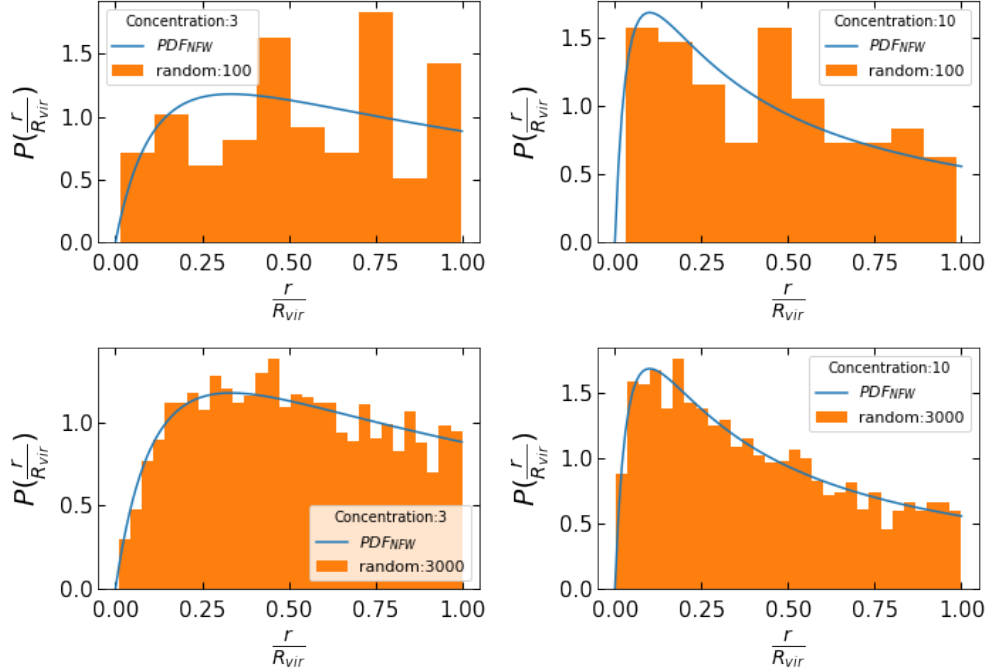
For the model without the additional information more assumptions were used in order to improve the subhaloes spatial distribution results. Briefly, this included an assumption for the host's virial radius, different spatial distributions and a different way for adding spatial information in the initial model. An additional assumption which was tested was the subhaloes having a cut condition in their positions equal to the host's virial radius at their accretion redshift value. This approach led to even higher subhalos' number density near the core and so it was resulting to even worst final subhalos spatial distribution. Also, a different concentration parameter in the NFW profile was used, the smaller the concentration the more biased is the NFW profile towards higher distance values. This assumption can be connected to different gravitational effects of subhaloes from the dark matter particles, but also this change did not improve the model significantly.

An additional process of adding spatial information in the model was tested, which would be applicable to the case of mass segregation effects in the halo's substructure. From simulations results and theory it is not expected such an effect, but if that would be the case the subhaloes positions should have been defined randomly (or the final positions probability distribution to be mass dependent). For this process the approach which was used included the selection of the positions of the subhaloes to be assigned randomly based on the algorithm of previous work [63] for random position selection from the NFW density profile:

$$r([0, 1]; c) = q(p = \text{Uniform}[0, 1]; c), q = -\frac{1}{c} \left[1 + \frac{1}{W_0(e^{-pM(1)-1})} \right] \quad (5.3.1)$$

where W_0 is a Lambert W function and $c, M(1)$ is the concentration and the total mass of the host halo (which works as a normalization term). But choosing random values of a given probability density distribution has an accuracy which is highly dependent on the number of random values.

Figure 71: Random selection of subhaloes position.

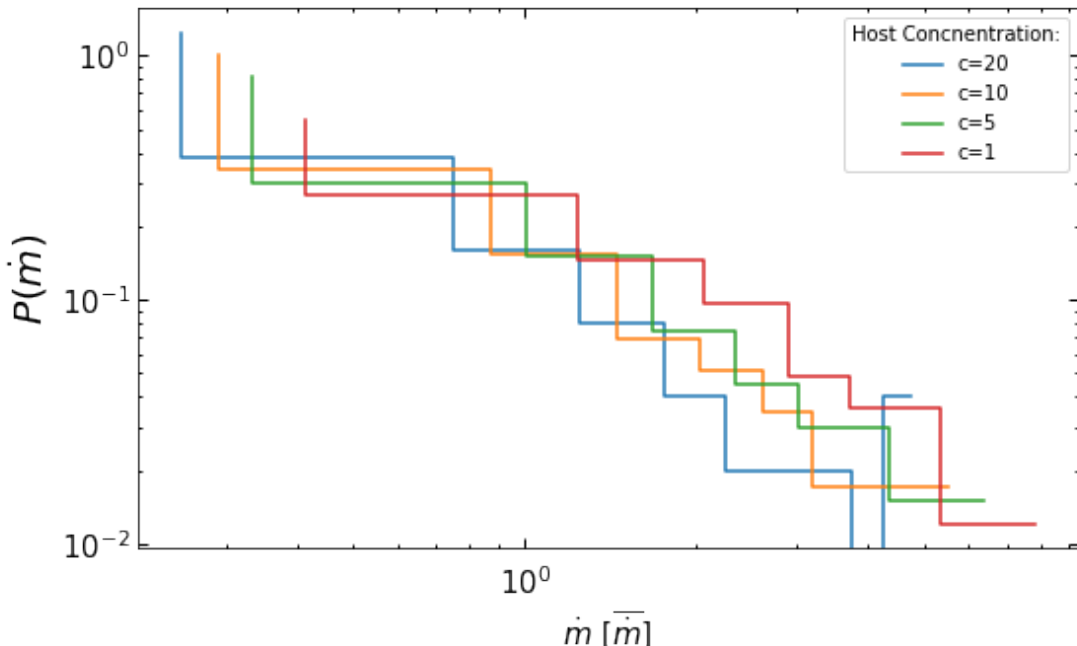


Comparison between the random positions' distribution and the wanted NFW density profile for different number of random values and host's concentration values.

This approach seem to require high computational power, the distribution of the positions of subhaloes in order to have a sufficient agreement with the NFW profile needs around 1000 random values, while the concentration of the host do not change this correlation importantly. For reaching values at very low orbital radius values of subhalos (host's core area) this approach would be extremely slow. This approach was explored by using the toy mass loss model case, the main reason was the absence of the N-body simulation spatial results at the first stages of this project.

An important test of this different process is the probability of the mass loss rate at different distances from the host's center. In order for this model to be proper the mass loss rate distribution should be close to the toy model mass loss rate presented in the methodology section.

Figure 72: *Mass loss statistics.*



By using the random position selection process for adding spatial information in the main model the mass loss rate probability at different distances from the host's core are presented in units of virial radius.

It can be seen that the mass loss rate have a similar behavior as the toy model mass loss rate (exponential PDF) and so it would be credible to add the spatial information in the initial model through this process, but as it has been mentioned it would not be practical due to the extremely high computational work for the same accuracy as this project's process. Through this different modeling more characteristics on the subhaloes could be added such as elliptical shapes and elliptical orbits of subhaloes, with also providing the possibility of randomness in the model's results (which could be useful in making realistic mock catalogues of subhalos).

5.4 Gravitational lensing applications

The gravitational effects of massive haloes on photons' paths due to their huge amount of mass have been observed. These effects can be at weak lensing or strong lensing regime, but in this section the strong lensing is discussed since it is easier to be observed. The strong lensing leads to arcs and rings of light in the sky. For these shapes to happen a light source of photons, such as a galaxy or a quasar, before reaching us (the observer) they pass through another object, such as galactic clusters, which works as a lens. Depending on the line of sight and the alignment of the lens and the source, arcs and rings have been observed, with the perfect alignment with our line of sight leading to the Einstein rings. These rings' radius can be easily calculated by:

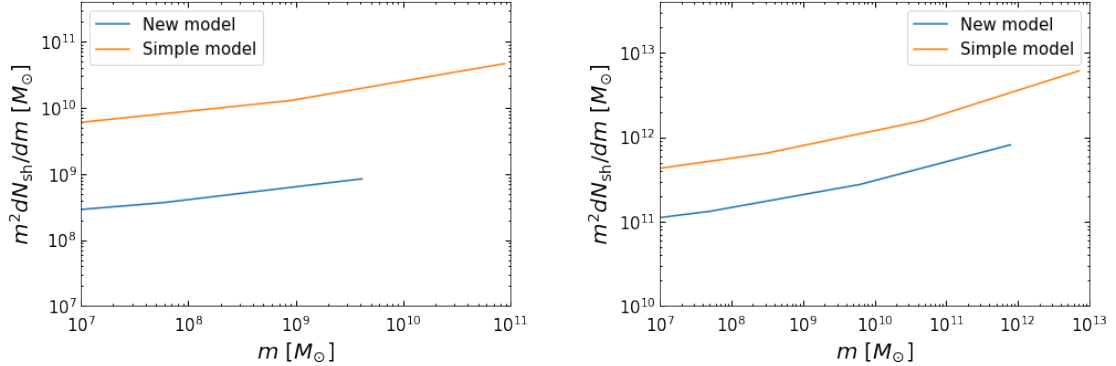
$$R_E = \left(\frac{4GM}{c^2} \frac{D_{LS}}{D_S \cdot D_L} \right) \quad (5.4.1)$$

where M is the mass of the lens, D_L is the distance from the lens, D_S is the distance from the source and D_{LS} is the distance between the lens and the source.

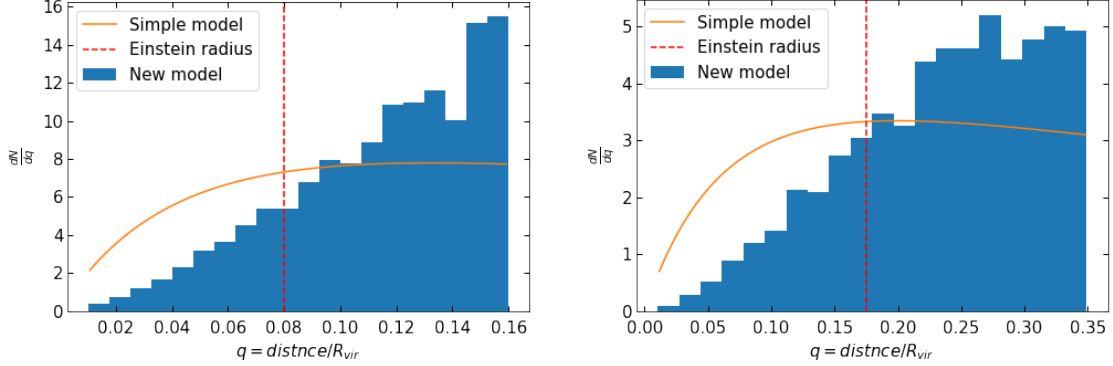
A lot of recent models on the gravitational lensing research sector involves statistical inference and machine learning techniques for discovering the underlying mass which causes such effects. The host halos which are massive are expected to create arcs and rings, but subhalos also can effect the lensing causing distortions from the host alone lensing image. This kind of observations is the best opportunity for the indirect detection of dark matter and their characteristics, especially in this decade with the number of strong lensing observations expected to be highly increased. For these studies mock catalogues of subhalos following basic assumptions are used, broadly it is used for subhalos spatial distribution the NFW profile of the host halo and for their mass the $\frac{dN_{sh}}{dm_{sh}} \sim m_{sh}^{-\alpha}$ relation with α given by N-body simulations results. But this approach ignores the effects of tidal stripping on the substructure and the model of this thesis could be useful for having more accurate subhaloes information.

For this reason briefly the differences between this model's results and the simplistic version used in gravitational lensing are shown for subhaloes' mass, position and number. Commonly there are spatial ranges and subhalos mass ranges where the lensing effects are expected to be measurable, the area of 2 Einstein ring radius and subhalo's mass higher than 10^7 solar masses are defined respectively. The cases of hosts with masses at 10^{12} and 10^{14} at $z=0.2$ as a lens and the source being at $z=0.7$ are used, with their Einstein radius to be around 0.08 and 0.175 host's virial radius respectively. For the case of a simplistic model the α parameter can be find different for different models but in this case the initial model is used for subhaloes mass and the simple NFW profile for their position.

Figure 73: *Lensing effects : subhalos mass.*



Subhaloes mass function within 2 Einstein radius for the cases of the new model and the simplistic model, for host with mass 10^{12} (left) and 10^{14} (right) solar masses at $z=0.2$.

Figure 74: *Lensing effects : subhaloes radius.*

Subhaloes linear probability function within 2 Einstein radius for the cases of the new model and the simplistic model, for host with mass 10^{12} (left) and 10^{14} (right) solar masses at $z=0.2$.

The spatial differences of the two approaches differs highly, while tidal effects leads to less massive subhaloes at the given range. In the new model the number of subhalos in the given mass and spatial range are reduced significantly from 84 to 20 for $M_{host} = 10^{12}$ and from 9108 to 1374 for $M_{host} = 10^{14}$. But this is not a complete study, since subhaloes do not follow circular orbits but elliptical ones. A great modification of the new model's results could be further upgraded by assuming the resulting circular orbit radius to be the semi major axis of their orbit and by using the distribution of subhaloes ellipticity to choose a random value of time for their positions. This situation is very close to the expected behavior of subhaloes in reality, with the subhalos of the outer host's area, which are much more but also more massive, to be able to contribute to lensing effects.

6. Conclusions

The formation and evolution of dark matter halos and subhaloes is an extremely complex problem to solve analytically. This process starts from the early stages of the halos creation by overdensities gravitationally collapsing in an expanding universe and continues until the later years of the universe, when halos are colliding, merging and accreting each other. The instabilities of overdensities' collapsing solutions leads to diversity of haloes characteristics, while halos' interactions as evolving add more complexity by their broad range of momentum, angular momentum, mass and position values, making an analytical solution for substructure to be impossible to be found. The best way for gathering information for dark matter structures is N-body simulations, but the current computational power have limited spatial and mass resolution, while the time needed for a N-body simulation to be completed can be huge. This project's model can provide a semi-analytical tool to tackle these problems, by not having resolution limitations, being fast and calculating a variety of halo's substructure characteristics.

The best case of model resulted in this project is the presented new model, which can be used further for studying even more effects of dark matter in small scale. The possible results and dark matter substructure insights which this model can provide did not cover fully and so there is more work to be done. For example, spatial effects on different subhaloes characteristic distribution can be found for a more wide range of host halo's mass and redshift values. Also, by the annihilation boost factor the dark matter contribution to gamma-ray intensity of known observations can be used for updating current constraints on dark matter mass and annihilation cross section values. Last but not least, the satellite galaxies can be studied with also their spatial characteristics by this model, while a tool for testing different galaxy formation condition and comparing them fully with the respected observations.

This project seem to accomplish reaching results close to the expected values, leading to an Einasto spatial distribution for subhaloes and subhaloes' properties similar to the N-body simulations. Beside the goal of creating an effective halo's substructure model, an important additional goal was to stress the idea of a simplistic model with the lowest amount of information included. This is the reason for studying the basic assumptions extensively, with these assumptions to be generic physical expectations but also well tested dark matter N-body simulation's results. As it is shown, the initially defined assumptions are not enough to explain the observed spatial (in simulations) Einasto profile through only tidal forces effects, and an abstract spatial assumption had to be introduced. This new assumption of course has to be further tested, with its presented results to have a great agreement with the wanted behavior. Although such broad parameter's range approaches are rare, in this project it is shown that a simplistic semi-analytic model can be accurate and provide a wide variety of useful results, especially if it will be further studied as discussed by including more information. Additionally, with more data from observations and simulations of warm dark matter to be expected the presented model can be further adjusted to warm dark matter particles, but at this stage the shown results are not well tested.

The applications of this model are shown to be very helpful for the indirect dark matter searches. The main applications of this model could be in dark matter searches through gravitational lensing and gamma-ray observations, providing substructure information which includes tidal forces (with these forces to be usually neglected for simplicity). The first case is briefly discussed and is shown that the differences with the commonly used models can be important, leading to much different lensing effects but also increasing the possibility of measuring individual massive subhaloes. For the other case, the annihilation boost factor with spatial dependency which was calculated in this project is one of the few (if not the first) existing results. The substructures contribution in the total dark matter luminosity is higher than the predicted initial model's, and if the subhalos of subhaloes (and further to smaller subhaloes) gamma-ray emissions are considered the luminosity of dark matter substructure can be further increased. Also, the luminosity templates shown could be extremely useful for gamma-ray studies of galaxies and galactic clusters, especially if the gamma-ray contribution of the host is added by some well tested dark matter particles' annihilation models in the NFW density profile. If the presented luminosity templates have all the dark matter components the first such result of full gamma-ray mock images of dark matter halos can be produced, which could be used in analysis studies of gamma-ray observations for identifying possible contribution of dark matter through statistical inference techniques.

Dark matter is hiding from physicists for a long time and this decade more insights are expected from the instruments of this era, via direct and indirect detection experiments. Models like this projects can contribute to dark matter searches with accurate results, based on the current dark matter knowledge, providing a flexible tool to stress different dark matter models and analysis techniques.

References

- [1] Wikipedia contributors, *Dark matter — Wikipedia, the free encyclopedia*, https://en.wikipedia.org/w/index.php?title=Dark_matter&oldid=1097841883, [Online; accessed 15-July-2022], 2022.
- [2] Z. F., ‘On the masses of nebulae and of clusters of nebulae,’ *The Astrophysical Journal*, vol. 86, pp. 217–246, 1937. DOI: [10.1086/143864](https://doi.org/10.1086/143864).
- [3] F. K.C., ‘On the disks of spiral and s0 galaxies,’ *The Astrophysical Journal*, vol. 160, pp. 811–830, 1970. DOI: [10.1086/150474](https://doi.org/10.1086/150474).
- [4] R. V. C. and F. W. Kent, ‘Rotation of the andromeda nebula from a spectroscopic survey of emission regions,’ *The Astrophysical Journal*, vol. 159, pp. 379–403, 1970. DOI: [10.1086/150317](https://doi.org/10.1086/150317).
- [5] Corbelli and Salucci, ‘The extended rotation curve and the dark matter halo of m33,’ *Monthly Notices of the Royal Astronomical Society*, vol. 311, pp. 441–447, 2 Jan. 2000. DOI: <https://doi.org/10.1046/j.1365-8711.2000.03075.x>. [Online]. Available: arxiv.org/abs/astro-ph/9909252.
- [6] E. Allen and Mantz, ‘Cosmological parameters from clusters of galaxies,’ *Annual Review of Astronomy and Astrophysics*, vol. 49, pp. 409–470, 1 2011. DOI: <https://doi.org/10.1146/annurev-astro-081710-102514>. [Online]. Available: arxiv.org/abs/1103.4829.
- [7] Clowe, G. Bradac, J. Markevitch Randall and Zaritsky, ‘A direct empirical proof of the existence of dark matter,’ *The Astrophysical Journal Letters*, vol. 648, pp. L109–L113, 2 2006. DOI: <https://doi.org/10.1086>. [Online]. Available: arxiv.org/abs/astro-ph/0608407.
- [8] P. Collaboration, ‘Planck 2015 results. xiii. cosmological parameters,’ *Astron. Astrophys.*, vol. 594, Oct. 2016. DOI: <https://doi.org/10.1051/0004-6361/201525830>. [Online]. Available: [arXiv:1502.01589](https://arxiv.org/abs/1502.01589).
- [9] H. J. Z. et al, ‘Stellar velocity dispersion: Linking quiescent galaxies to their dark matter halos,’ *The American Astronomical Society*, vol. 859, 2018. DOI: <https://doi.org/10.3847/1538-4357/aabe31>.
- [10] J. e. a. Peacock, ‘A measurement of the cosmological mass density from clustering in the 2df galaxy redshift survey,’ *Nature*, vol. 410, pp. 169–173, 2001. DOI: <https://doi.org/10.48550/arXiv.astro-ph/0103143>. [Online]. Available: [arXiv:astro-ph/0103143](https://arxiv.org/abs/astro-ph/0103143).
- [11] A. Garzilli, A. Magalich, C. S. F. Tom Theuns, C. Weniger, O. Ruchayskiy and A. Boyarsky, ‘The Lyman – α forest as a diagnostic of the nature of the dark matter,’ *Monthly Notices of the Royal Astronomical Society*, vol. 489, pp. 3456–3471, 2019. DOI: <https://doi.org/10.48550/arXiv.1809.06585>. [Online]. Available: [arXiv:1809.06585](https://arxiv.org/abs/1809.06585).
- [12] L. J. Chang, ‘Dark matter in the milky way,’ Ph.D. dissertation, Princeton University, 2020.
- [13] M. Esra Bulbul, A. F. Markevitch, R. K. Smith, M. Loewenstein and S. W. Randall, ‘Detection of an unidentified emission line in the stacked x-ray spectrum of galaxy clusters,’ *The Astrophysical Journal*, vol. 789, 2014. DOI: <https://doi.org/10.48550/arXiv.1402.2301>. [Online]. Available: [arXiv:1402.2301](https://arxiv.org/abs/1402.2301).
- [14] A. R. Edward W. Kolb Daniel J. H. Chung, ‘Wimpzillas!’ *AIP Conf. Proc.*, vol. 484, pp. 91–105, 1 Apr. 1999. [Online]. Available: [arXiv:hep-ph/9810361](https://arxiv.org/abs/hep-ph/9810361).
- [15] T. T. Misao Sasakia Teruaki Suyamab and S. Yokoyamad, ‘Primordial black holes- perspectives in gravitational wave astronomy,’ DOI: <https://doi.org/10.1111/j.1365-2966.2004.08304.x>. [Online]. Available: [arXiv:1801.05235](https://arxiv.org/abs/1801.05235).
- [16] M. S. Bernard Carr Florian Kuhnel, ‘Primordial black holes as dark matter,’ *Monthly Notices of the Royal Astronomical Society*, vol. 457, pp. 1208–1223, 2 Apr. 2016. DOI: <https://doi.org/10.1093/PhysRevD.94.083504>. [Online]. Available: [arXiv:1607.06077](https://arxiv.org/abs/1607.06077).
- [17] Bharadwaj, S. S. Somnath Bhavsar and J. V, ‘The size of the longest filaments in the universe,’ *Astrophys J.*, vol. 606, pp. 25–31, 1 2004. [Online]. Available: [arXiv:astro-ph/0311342](https://arxiv.org/abs/astro-ph/0311342).

- [18] F. van den Bosch, *Theory of galaxy formation*, 2020. [Online]. Available: http://www.astro.yale.edu/vdbosch/Theory_of_Galaxy_Formation.pdf.
- [19] R. A. César A. Chacón-Cardona and Casas-Miranda, ‘Millennium simulation dark matter haloes: Multi-fractal and lacunarity analysis with homogeneity transition,’ *MNRAS*, vol. 427, pp. 2613–2624, 3 2012. DOI: <https://doi.org/10.1111/j.1365-2966.2012.22095.x>.
- [20] J. F. Navarro, C. S. Frenk and S. D. M. White, ‘Universal density profile from hierarchical clustering,’ *Astrophys. J.*, vol. 490, pp. 493–508, 1997. DOI: <https://doi.org/10.48550/arXiv.astro-ph/9611107>. [Online]. Available: <arXiv:astro-ph/9611107>.
- [21] A. D. Popolo and M. L. Delliou, ‘Small scale problems of the Λ CDM model: A short review,’ *Galaxies*, vol. 5, 1 Feb. 2017. DOI: <https://doi.org/10.3390/galaxies5010017>. [Online]. Available: <arXiv:1606.07790>.
- [22] Moore, ‘Evidence against dissipation-less dark matter from observations of galaxy haloes.,’ *Nature*, vol. 370, pp. 629–631, 1994.
- [23] Moore, S. Quinn Governato and Lake, ‘Cold collapse and the core catastrophe.,’ *Monthly Notices of the Royal Astronomical Society*, vol. 310, pp. 1147–1152, 1999. [Online]. Available: <astro-ph/9903164>.
- [24] V. Klypin Kravtsov and Pradae, ‘Where are the missing galactic satellites?’ *The Astrophysical Journal*, vol. 522, pp. 82–92, 1999. [Online]. Available: <arXiv:astro-ph/astro-ph/9901240>.
- [25] van den Bosch, Burkert and Swaters, ‘The angular momentum content of dwarf galaxies: New challenges for the theory of galaxy formation,’ *Monthly Notices of the Royal Astronomical Society*, vol. 326, pp. 1205–1215, 2001. [Online]. Available: <astro-ph/0105082>.
- [26] Pawłowski, M. Famaey Jerjen, D. Kroupa *et al.*, ‘Co-orbiting satellite galaxy structures are still in conflict with the distribution of primordial dwarf galaxies,’ *Monthly Notices of the Royal Astronomical Society*, vol. 442, pp. 2362–2380, 2014. DOI: <1406.1799>.
- [27] McGaugh, ‘Novel test of modified newtonian dynamics with gas rich galaxies.,’ *Physical Review Letters*, vol. 106, 2011. [Online]. Available: <arXiv:astro-ph.CO/1102.3913>.
- [28] Navarro and Steinmetz, ‘Dark halo and disk galaxy scaling laws in hierarchical universes.,’ *Astrophys. J.*, vol. 538, pp. 477–488, 2000. DOI: <https://doi.org/10.48550/arXiv.astro-ph/0001003>. [Online]. Available: <arXiv:astro-ph/0001003>.
- [29] Navarro and Benz, ‘Dynamics of cooling gas in galactic dark halos,’ *Astrophys. J.*, vol. 380, pp. 320–329, 1991. DOI: <10.1086/170590>. [Online]. Available: <https://ui.adsabs.harvard.edu/abs/1991ApJ...380..320N/abstract>.
- [30] G. Sommer-Larsen and Vedel, ‘Formation of disk galaxies: Feedback and the angular momentum problem,’ *Astrophys. J.*, vol. 519, pp. 501–512, 1999. DOI: <https://doi.org/10.48550/arXiv.astro-ph/9801094>.
- [31] L. Del Popolo, Fabris and Rodrigues, ‘A unified solution to the small scale problems of the cdm model,’ *Journal of Cosmology and Astroparticle Physics*, vol. 21, 2014. DOI: <https://doi.org/10.48550/arXiv.1404.3674>.
- [32] Wikipedia contributors, *Cuspy halo problem — Wikipedia, the free encyclopedia*, https://en.wikipedia.org/w/index.php?title=Cuspy_halo_problem&oldid=1079231782, [Online; accessed 15-July-2022], 2022.
- [33] J. e. a. Navarro, ‘The cores of dwarf galaxy haloes,’ *Monthly Notices of the Royal Astronomical Society*, vol. 283, pp. L72–L78, 3 1996. DOI: <https://doi.org/10.48550/arXiv.1106.049>. [Online]. Available: <arXiv:1106.0499>.
- [34] A. e. a. Pontzen, ‘How supernova feedback turns dark matter cusps into cores,’ *Monthly Notices of the Royal Astronomical Society*, vol. 421, pp. 3464–3471, 4 2012. DOI: <https://doi.org/10.48550/arXiv.1106.0499>. [Online]. Available: <arXiv:1106.0499>.
- [35] O. e. a. Elbert, ‘Core formation in dwarf haloes with self-interacting dark matter: No fine-tuning necessary,’ *Monthly Notices of the Royal Astronomical Society*, vol. 453, pp. 29–37, 1 2015. DOI: <https://doi.org/10.48550/arXiv.1412.1477>. [Online]. Available: <arXiv:1412.1477>.

- [36] M. e. a. Lovell, ‘The haloes of bright satellite galaxies in a warm dark matter universe,’ *Monthly Notices of the Royal Astronomical Society*, vol. 420, pp. 2318–2324, 3 2012. DOI: <https://doi.org/10.48550/arXiv.1104.2929>. [Online]. Available: [arXiv:1104.2929](https://arxiv.org/abs/1104.2929).
- [37] M. Goetz and J. Sommer-Larsen, ‘Galaxy formation: Warm dark matter, missing satellites, and the angular momentum problem,’ *Astrophys. Space Sci.*, vol. 284, pp. 341–344, 2003. DOI: <https://doi.org/10.48550/arXiv.astro-ph/0210599>. [Online]. Available: [arXiv:astro-ph/0210599](https://arxiv.org/abs/astro-ph/0210599).
- [38] P. B. et al., ‘Beyond Λ CDM: Problems, solutions, and the road ahead,’ *Physics of the Dark Universe*, vol. 12, pp. 56–99, Jun. 2016. DOI: <https://doi.org/10.48550/arXiv.1512.05356>. [Online]. Available: [arXiv:1512.05356](https://arxiv.org/abs/1512.05356).
- [39] A. H. G. P. Stacy Y. Kim and J. R. Hargis, ‘There is no missing satellites problem,’ *Phys. Rev. Lett.*, vol. 121, 2018. DOI: <https://doi.org/10.48550/arXiv.1711.06267>. [Online]. Available: [arXiv:1711.06267](https://arxiv.org/abs/1711.06267).
- [40] M. S. Pawłowski, ‘The planes of satellite galaxies problem, suggested solutions, and open questions,’ *Modern Physics Letters A*, vol. 33, 2018. DOI: <https://doi.org/10.48550/arXiv.1802.02579>. [Online]. Available: [arXiv:1802.02579](https://arxiv.org/abs/1802.02579).
- [41] A. M. Brooks, A. Z. Michael Kuhlen and D. Hooper, ‘A baryonic solution to the missing satellites problem,’ *The Astrophysical Journal*, vol. 765, 2013. DOI: <https://doi.org/10.48550/arXiv.1209.5394>. [Online]. Available: [arXiv:1209.5394](https://arxiv.org/abs/1209.5394).
- [42] S. A. Nagisa Hiroshima and T. Ishiyama, ‘Modeling evolution of dark matter substructure and annihilation boost,’ *Phys. Rev.*, vol. 97, 2018. [Online]. Available: [arXiv:1803.07691](https://arxiv.org/abs/1803.07691).
- [43] P. Collaboration, ‘Planck 2013 results xvi cosmological parameters,’ *Astron. Astrophys.*, vol. 571, 2014. [Online]. Available: [arXiv:1303.5076](https://arxiv.org/abs/1303.5076).
- [44] C. A. Correa, J. S. J. S. B. Wyithe and A. R. Duffy, ‘The accretion history of dark matter haloes – i. the physical origin of the universal function,’ *Mon. Not. Roy. Astron. Soc.*, vol. 450, pp. 1514–1520, 2 2015. DOI: <https://doi.org/10.48550/arXiv.140.5228>. [Online]. Available: [arXiv:1409.5228](https://arxiv.org/abs/1409.5228).
- [45] Correa, S. Wyithe and Duffy, ‘The accretion history of dark matter haloes – iii. a physical model for the concentration–mass relation,’ *Mon. Not. Roy. Astron. Soc.*, vol. 452, pp. 1217–1232, 2 2015. DOI: <https://doi.org/10.48550/arXiv.1502.00391>. [Online]. Available: [arXiv:1502.00391](https://arxiv.org/abs/1502.00391).
- [46] F. Jiang and F. C. van den Bosch, ‘Statistics of dark matter substructure – i. model and universal fitting functions,’ *Monthly Notices of the Royal Astronomical Society*, vol. 458, pp. 2848–2869, 2016. [Online]. Available: [arXiv:1403.6827](https://arxiv.org/abs/1403.6827).
- [47] A. R. Wetzel, ‘On the orbits of infalling satellite halos,’ *Mon. Not. Roy. Astron. Soc.*, vol. 412, 2011. DOI: <https://doi.org/10.48550/arXiv.1001.4792>. [Online]. Available: [arXiv:1001.4792](https://arxiv.org/abs/1001.4792).
- [48] J. Penarrubia, M. G. W. A. J. Benson, A. M. G. Gilmore and L. Mayer, ‘The impact of dark matter cusps and cores on the satellite galaxy population around spiral galaxies,’ *Monthly Notices of the Royal Astronomical Society*, vol. 406, 2010. DOI: <https://doi.org/10.48550/arXiv.1002.3376>.
- [49] X. Yang, Y. Z. H. J. Mo and F. C. v. d. Bosch, ‘An analytical model for the accretion of dark matter subhaloes,’ *Astrophys. J.*, vol. 741, 2011. [Online]. Available: [arXiv:1104.1757](https://arxiv.org/abs/1104.1757).
- [50] A. D. Ludlow, R. E. A. S. Bose, W. A. H. L. Wang, S. C. J. F. Navarro and C. S. Frenk, ‘The mass–concentration–redshift relation of cold and warm dark matter haloes,’ *Mon. Not. Roy. Astron. Soc.*, vol. 460, pp. 1214–1232, 2 2016. [Online]. Available: [arXiv:1601.02624](https://arxiv.org/abs/1601.02624).
- [51] G. L. Bryan and M. L. Norman, ‘Statistical properties of x-ray clusters: Analytic and numerical comparisons,’ *Astrophys. J.*, vol. 495, 1998. DOI: <https://doi.org/10.48550/arXiv.astro-ph/9710107>. [Online]. Available: [arXiv:astro-ph/9710107](https://arxiv.org/abs/astro-ph/9710107).
- [52] W. Hu and A. V. Kravtsov, ‘Sample variance considerations for cluster surveys,’ *Astrophys. J.*, vol. 584, pp. 702–715, 2003. DOI: <https://doi.org/10.48550/arXiv.astro-ph/0203169>. [Online]. Available: [arXiv:astro-ph/0203169](https://arxiv.org/abs/astro-ph/0203169).

- [53] T. Ishiyama, S. P. Z. J. Makino, K. N. D. Groen *et al.*, ‘The cosmogrid simulation:statistical properties of small dark matter halos,’ *Astrophys. J.*, vol. 767, 2013. DOI: <https://doi.org/10.48550/arXiv.1101.2020>. [Online]. Available: [arXiv:1101.2020](https://arxiv.org/abs/1101.2020).
- [54] J. Penarrubia, M. G. W. A. J. Benson, A. M. G. Gilmore and L. Mayer, ‘The impact of dark matter cusps and cores on the satellite galaxy population around spiral galaxies,’ *Mon. Not. Roy. Astron. Soc.*, vol. 406, p. 1290, 2010. DOI: <https://doi.org/10.48550/arXiv.1002.3376>. [Online]. Available: [arXiv:1002.3376](https://arxiv.org/abs/1002.3376).
- [55] E. Hayashi, J. E. T. J. F. Navarro, J. Stadel and T. R. Quinn, ‘The structural evolution of substructure,’ *Astrophys. J.*, vol. 584, pp. 541–558, 2003. DOI: <https://doi.org/10.48550/arXiv.astro-ph/0203004>. [Online]. Available: [arXiv:astro-ph/0203004](https://arxiv.org/abs/astro-ph/0203004).
- [56] W. Springel, J. Vogelsberger Ludlow, F. Helmi Navarro and White, ‘The aquarius project: The subhalos of galactic halos,’ *Monthly Notices of the Royal Astronomical Society*, vol. 391, pp. 1685–1711, Dec. 2008. DOI: <https://doi.org/10.1111/j.1365-2966.2008.14066.x>. [Online]. Available: [arXiv:0809.0898](https://arxiv.org/abs/0809.0898).
- [57] A. G.-S. Shin’ichiro Ando, R. T. Nagisa Hiroshima Sebastian Hoof and M. G. Walker, ‘Structure formation models weaken limits on wimp dark matter from dwarf spheroidal galaxies,’ *Phys. Rev.*, vol. 102, 2020. [Online]. Available: [arXiv:2002.11956](https://arxiv.org/abs/2002.11956).
- [58] C. A. C. Ariane Dekker Shin’ichiro Ando and K. C. Ng, ‘Warm dark matter constraints using milky-way satellite observations and subhalo evolution modeling,’ 2021. [Online]. Available: [arXiv:2111.13137](https://arxiv.org/abs/2111.13137).
- [59] J. M. Gaskins, ‘A review of indirect searches for particle dark matter,’ *Contemp. Phys.*, vol. 57, 4 2016. [Online]. Available: [arXiv:1604.00014](https://arxiv.org/abs/1604.00014).
- [60] C. S. F. Jiaxin Han Shaun Cole and Y. Jing, ‘A unified model for the spatial and mass distribution of subhaloes,’ *Monthly Notices of the Royal Astronomical Society*, vol. 457, pp. 1208–1223, 2 Apr. 2016. DOI: <https://doi.org/10.1093/mnras/stv2900>. [Online]. Available: <https://academic.oup.com/mnras/article/457/2/1208/965286>.
- [61] M. Oguri and J. Lee, ‘A realistic model for spatial and mass distributions of dark halo substructures: An analytic approach,’ *Monthly Notices of the Royal Astronomical Society*, vol. 355, pp. 120–128, 1 Apr. 2004. DOI: <https://doi.org/10.1111/j.1365-2966.2004.08304.x>. [Online]. Available: [arXiv:astro-ph/0401628](https://arxiv.org/abs/astro-ph/0401628).
- [62] C. Barber, J. N. Else Starkenburg, A. McConnachie and A. Fattahi, ‘The orbital ellipticity of satellite galaxies and the mass of the milky way,’ *Monthly Notices of the Royal Astronomical Society*, vol. 437, pp. 959–967, 1 Jan. 2014. DOI: <https://doi.org/10.1093/mnras/stt1959>. [Online]. Available: [arXiv:1310.0466](https://arxiv.org/abs/1310.0466).
- [63] C. H. A. S. G. Robotham, ‘A short research note on calculating exact distribution functions and random sampling for the 3d nfw profile,’ *Monthly Notices of the Royal Astronomical Society*, vol. 437, pp. 959–967, 1 Jan. 2014. DOI: <https://doi.org/10.48550/arXiv.1805.09550>. [Online]. Available: [arXiv:1805.09550v2](https://arxiv.org/abs/1805.09550v2).